Lagrangian and Eulerian representations of fluid flow
Part 2: Advection of parcels and fields

James F. Price

Woods Hole Oceanographic Institution,
Woods Hole, Massachusetts, 02543
https://www2.whoi.edu/staff/jprice/ jprice@whoi.edu

January 4, 2024

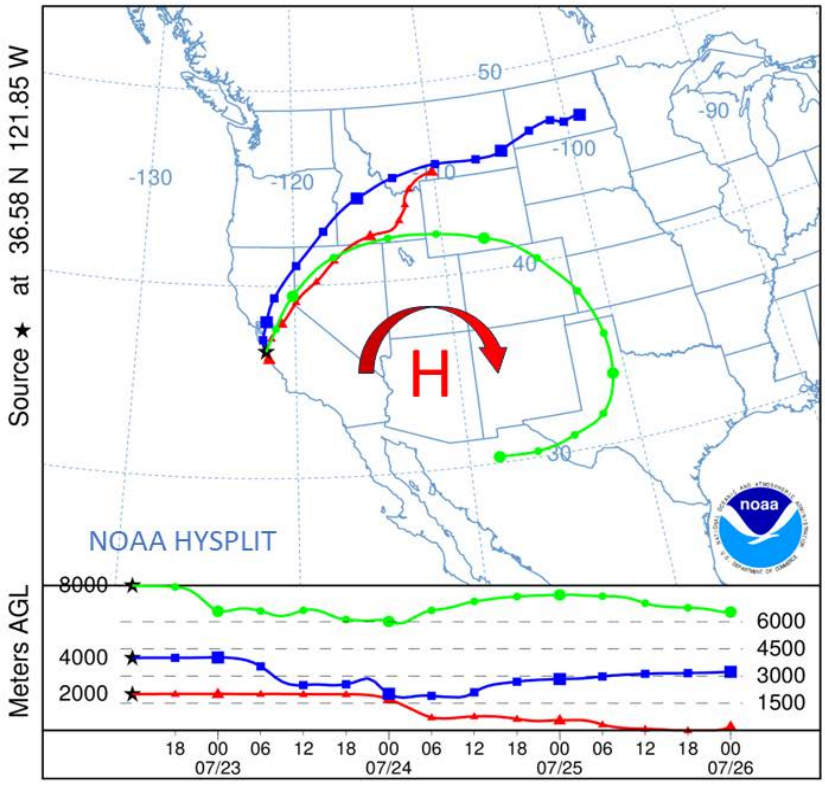

Figure 1: Tracer transport by fluid flow may be represented by parcel trajectories, the Lagrangian perspective of these simulated balloon trajectories, or by advection of tracer fields, the Eulerian perspective. The goal of this essay is to learn how Lagrangian and Eulerian methods and data may be used side-by-side. These trajectories were computed by the NOAA HYSPLIT system with essential wind data in the form of gridded (Eulerian) velocity fields computed by a weather forecast model. This kind of Eulerian to Lagrangian transformation is a central theme of this essay.

Abstract: This essay continues an introduction to Lagrangian and Eulerian methods of fluid mechanics. Part 1 argued that Lagrangian observations and conservation laws are the natural starting point for an analysis of fluid flows, though the resulting Lagrangian equations of motion are generally very difficult. The majority of theory is developed within Eulerian systems, and so this Part 2 flips the script: the starting point is presumed to be a known velocity field (Eulerian), and the theme is transformation to several kinds of Lagrangian diagnostic quantities, especially trajectories.

If what we know is a velocity field, then to know where a parcel is going, we have to know where it is. This amounts to inverting the fundamental principle of kinematics (FPK) of Part 1. Computation of a trajectory is an integration in time of the velocity at the moving position of the parcel. The fidelity of the trajectory will depend in a straightforward way upon the spatial resolution of the velocity field and upon the temporal resolution of the integration. There are a number of useful variants on the notion of a trajectory, including streaklines, which show the location of parcels that have a common source but different starting times, and backwards trajectories, that show where parcels present at a given position and time have come from. These are important tools for air quality forecasts, for example.

If the Eulerian velocity has been time-averaged or otherwise undersamples the velocity, then the FPK (or its inverse) does not apply, strictly. The difference between the time-averaged Lagrangian and Eulerian velocities may be attributed to Stokes drift, a material (Lagrangian) velocity that arises from correlation between parcel displacement and the spatial gradient of the Eulerian velocity. Stokes drift is especially important when this correlation is high, as it is in wind-driven gravity wave motion on the ocean surface. In that case the Stokes drift is downwind and surface intensified, and can be fairly large amplitude.

Advection represents the transport of fluid properties at a definite rate and direction, that of the fluid velocity. Some Eulerian numerical models treat advection as an adiabatic process that translates parcels along the characteristics defined by the velocity field. These so-called semi-Lagrangian methods often provide a significant improvement in efficiency or accuracy compared to strictly Eulerian methods that advect the tracer field.

Advection does more than simply transport fluid. A velocity field that is spatially-varying (the norm) may cause linear and shear deformation of a fluid parcel. Deformation may cause an initially compact patch of a tracer to be strained into long, thin filaments that have a greatly increased perimeter. A nonuniform velocity may also cause a fluid parcel to rotate. The rotation rate, called the vorticity, is analogous to angular momentum and follows a particularly useful conservation law. The Cauchy-Stokes decomposition theorem relates the eigenvectors of the velocity gradient tensor to these deformations and to the rotation rate.

Most real fluid flows are made up of a range of time and space scales, spanning anything from one to eight decades (tea cup to the atmosphere). Most all analyses begin with the definition of the scales that will be resolved, and so by exclusion define the smaller space and faster time scales that will be unresolved, but whose effects may be treated statistically or by a parameterization. In the case that the fast time scale motion is a random walk, a suitable (Eulerian) parameterization may be an effective diffusivity. Deformation by a resolved flow plus effective diffusivity can lead to significantly enhanced mixing of a tracer.

More on Fig. (1). The emphasis here is on methods, mainly, but these simulated balloon trajectories reveal some of the inner workings of an important weather phenomenon that you might have experienced — a heat dome. The balloons were launched from the coast of central California in July 2023, and their trajectory was forecast ahead for 3.5 days. They were ballasted for initial altitudes of 2000, 4000 and 8000 m above ground level (AGL, lower panel) and thereafter maintained constant pressure. The ground rose beneath the balloons as they drifted toward mid-continent. The balloon at the highest altitude (the blue line) made a sweeping, clockwise-turning trajectory consistent with the free, geostrophic wind around a large, slowly evolving high pressure system. By comparison, the lower-level balloon trajectories showed evidence of the frictional effects expected within the atmospheric boundary layer (the lowest several kilometers of the atmosphere) *viz.*, reduced speed compared to the geostrophic wind at altitude, and trajectories that turned toward lower pressure (to the left looking downwind). Other trajectories that were started on the periphery of the high pressure system did the same. This pattern implies a horizontally divergent wind within the boundary layer that is largely compensated by descending air at mid-levels. The descending air is warmed by adiabatic compression, resulting in dry, clear skies and consequent high solar insolation at ground level. The high pressure weather pattern may persist for days or even a few weeks, as it did on this occasion, leading to prolonged high surface temperature, drought, and wildfires. This heat dome phenomenon was widespread during summer, 2023.

These trajectories are thanks to NOAA HYSPLIT, https://www.ready.noaa.gov/HYSPLIT.php a comprehensive Lagrangian analysis system for the atmosphere that offers excellent tutorials for new users. For much more on HYSPLIT, see A. F. Stein, R. R. Draxler, G. D. Rolph, B. J. B. Stunder and M. D. Cohen (2015), NOAAs HYSPLIT Atmospheric Transport and Dispersion Modeling System. Bull. of the American Met. Soc., Volume 96, Issue 12, pp. 2059 - 2077, DOI: https://doi.org/10.1175/BAMS-D-14-00110.1

Contents

1 Eulerian solutions ⇒ Lagrangian diagnostics

This is the second of a two part introduction to Lagrangian and Eulerian representations of fluid flow. Part 1 emphasized the kinematics of fluid flow, and the application of the conservation laws of classical physics to modelling a fluid flow. The point of view taken in Part 1 is that the Lagrangian perspective is fundamental in two respects: what we mean by fluid flow is generally the motion of specific fluid volumes or parcels, and, the conservation laws apply to such specific fluid volumes. It seems like the Lagrangian perspective is off to a strong start. However, the equations of motion written in Lagrangian coordinates are quite difficult for most complex problems, and so the vast majority of theory and modelling is carried out within Eulerian systems that represent fluid properties as fields rather than material volumes. The weather forecast model that generated the wind field required to calculate the balloon trajectories of Fig. 1 is an example. All such models calculate their solutions for wind and other air properties on four dimensional fields (grids), three space dimensions and time. These models are thus fundamentally Eulerian, though many of them make good use of Lagrangian submodels at key junctures, especially when accounting for advection.

1.1 Goal and plan

The broad goal of this essay is an improved understanding of advection, i.e., the transport of parcels and fields by a fluid flow. 'Parcels and fields' implies Lagrangian and Eulerian representations, and this essay

considers both. The aim is to understand how these representations are related, and why and how we may transform data from one to the other.

Sec. 2 begins with the most important and widely used version of this transformation, calculation of Lagrangian trajectories from an Eulerian velocity field, as in Fig. (1). In principle this is straightforward; the Lagrangian velocity is evaluated using the fundamental principle of kinematics (the FPK of Part 1) in reverse, and integrated over time. There can be interesting complications when time-averaging occurs either by virtue of the observation method, or via the analysis. The FPK (or its inverse) applies to the instantaneous velocity, and may not apply when time averages enter. A new kind of velocity, sometimes called Stokes drift, arises when parcel displacement and the fluid velocity are correlated as in surface gravity waves.

Advection by a spatially-varying flow also deforms fluid volumes, which is considered in Sec. 3. The Cauchy-Stokes Decomposition Theorem provides a concise accounting of the rotation and deformation of fluid parcels in terms of the eigenvalues and eigenvectors of the velocity gradient tensor. The rotation rate is proportional to the curl of the velocity, the vorticity, which is an analog of angular momentum. Vorticity follows a somewhat simpler governing equation than does momentum, and can be a valuable diagnostic (Sec. 6).

Sec. 4 acknowledges that most real fluid flows are comprised of a wide range of time and space scales, some of which are resolved and treated explicitly, and some of which may be on such small scale (time or space) that they simply have to be treated in aggregate, that is, statistically. Reynolds averaging shows that one consequence of the small scale motion is likely to be a flux of tracer that may sometimes be modelled as a diffusion process. In most real flows, advection and diffusion act concurrently, and deformation by the resolved scale of motion will often cause tracers to be drawn into thin streaks that have much greater surface area than would occur absent the deformtion. This stirring process can accelerate the homogenization of a tracer.

Numerical models have considerable freedom to choose how specific terms and processes are evaluated, and an understanding of Lagrangian-Eulerian representations can be very helpful in understanding the design of efficient numerical methods, Sec. 5. Advection of tracer fields can be represented by a straightforward evaluation of the Eulerian advection terms, $\mathbf{V} \cdot \nabla(\text{tracer})$, or, it can be treated by following the predicted or hindcast motion of parcels that conserve their tracer values. This latter approach, often called semi-Lagrangian advection, can yield efficient and accurate numerical solutions of advection processes. Particle in Cell models are the semi-Eulerian complement; they follow particles for long times and so are Lagrangian, but evaluate pressure gradients or gravitational attraction by mapping particle masses to a grid.

Finally, Sec. 6 returns to the Lagrangian observations of Part 1 Fig. 1 for an analysis of the vorticity balance of the mesoscale motion (space scales $O(10^5)$ m). The vorticity is estimated from a velocity gradient tensor fitted to a cluster of floats that are followed for several months. The vorticity of the float cluster is observed to change in a way that is consistent with approximate conservation of the potential vorticty, the sum of planetary and relative vorticity divided by the water depth.

1.2 Acknowledgments

Financial support during preparation was provided by the Academic Programs Office of the Woods Hole Oceanographic Institution and by the U.S. Office of Naval Research. Administrative support was provided by the Department of Physical Oceanography, Woods Hole Oceanographic Institution.

This essay is dedicated to Prof. Tom Rossby, Graduate School of Oceanography, University of Rhode Island, whose generosity and enthusiasm for Lagrangian measurements of the ocean made a lasting impression.

2 Tracking parcels in a velocity field

2.1 Parcel trajectories

Let the position of a specific parcel be denoted by $\tilde{\mathbf{X}}(t)$, where the tilde denotes a Lagrangian variable as in Part 1. The trajectory of a parcel is the history of the integrated Lagrangian velocity,

$$\tilde{\mathbf{X}}(\mathbf{A},t) \;=\; \int_0^t \tilde{\mathbf{V}}(\mathbf{A},t) \;+\; \mathbf{A}, \tag{1}$$

where the parcel is identified by the initial position, $\mathbf{A}$. The presumption made here in Part 2 is that we know the Eulerian velocity field, $\mathbf{V}(\mathbf{X},t)$, which may be evaluated for the necessary Lagrangian velocity by reversing the fundamental principal of kinematics (FPK) of Part 1,

$$\boxed{\tilde{\mathbf{V}}(\mathbf{A},t) \;=\; \mathbf{V}(\mathbf{X}=\tilde{\mathbf{X}}(\mathbf{A},\,t),t)} \tag{2}$$

The entire content of this important equation rests on the presence (or not) of the tildes. A literal translation of (2) is that the Lagrangian velocity of a parcel that is at the position $\tilde{\mathbf{X}}(\mathbf{A},t)$ is the Eulerian velocity at that position $\mathbf{X} \;=\; \tilde{\mathbf{X}}(\mathbf{A},t)$. In words — to know where you are going, you have to know where you are (Fig. 2).[1]

Given (1) and (2), we have the prescription for a

parcel trajectory from Eulerian velocity: $$\boxed{\tilde{\mathbf{X}}(\mathbf{A},t) \;=\; \int_0^t \mathbf{V}(\mathbf{X}=\tilde{\mathbf{X}}(\mathbf{A},t),t) \;+\; \mathbf{A}} \tag{3}$$

[1]This and similar figures were made by the author using AI and DALL.E 2.

Figure 2: Have you ever had a day that left you wondering...

Swirling and chaotic,
Where will life carry me next?
Well, where am I now?

The trajectory equations (3) are typically implicit, in that the integrand will usually depend upon $\tilde{\mathbf{X}}$. If the x component of velocity u depends upon y or v, or if v depends upon x or u, then these are coupled equations that have to be solved simultaneously. In either case, the integration of (3) will generally have to be sought with numerical methods. The trajectory will certainly have to be solved numerically when $\mathbf{V}$ is the product of a numerical model and comes in the form of gridded, four-dimensional fields (x, y, z and t), as in Fig. (1). The procedure is straightforward in principle. Given a present position and time, find the present velocity by four-dimensional interpolation of the gridded Eulerian fields. Using this velocity, step the position forward in time. At the new position, again interpolate the Eulerian fields to obtain the new velocity, and step forward in time once more, repeating to the end. The accuracy and efficiency of the trajectory calculation will often be improved by employing somewhat sophisticated interpolation schemes, and by time-stepping with predictor-corrector or Runga-Kutta schemes.

Granted that most applications will require numerical methods, it is nevertheless useful to consider a very simple two-dimensional velocity field that will permit analytic solutions,

$$\mathbf{V}(x,y,t) \;=\; x\mathbf{e}_x \;+\; \frac{y}{1+2t}\mathbf{e}_y, \tag{4}$$

which is plotted for two times in Fig. 3. The component equations of a trajectory are then

$$\frac{d\tilde{x}}{dt} \;=\; \tilde{x}, \quad \text{and} \quad \frac{d\tilde{y}}{dt} \;=\; \frac{\tilde{y}}{1+2t}. \tag{5}$$

Since the tilde appears on all of the x and y, we can just as well drop them, with the understanding that x and y are the coordinates of a specific, moving parcel, and, the x and y on the right hand sides of (5) are the same thing as the x and y on the left hand sides. Suitable initial conditions are

$$x \;=\; a, \quad \text{and} \quad y \;=\; b \quad \text{at} \quad t \;=\; t_o.$$

Within each component equation the independent variables can be readily separated,

$$\frac{dx}{x} \;=\; dt \quad \text{and} \quad \frac{dy}{y} \;=\; \frac{dt}{(1+2t)},$$

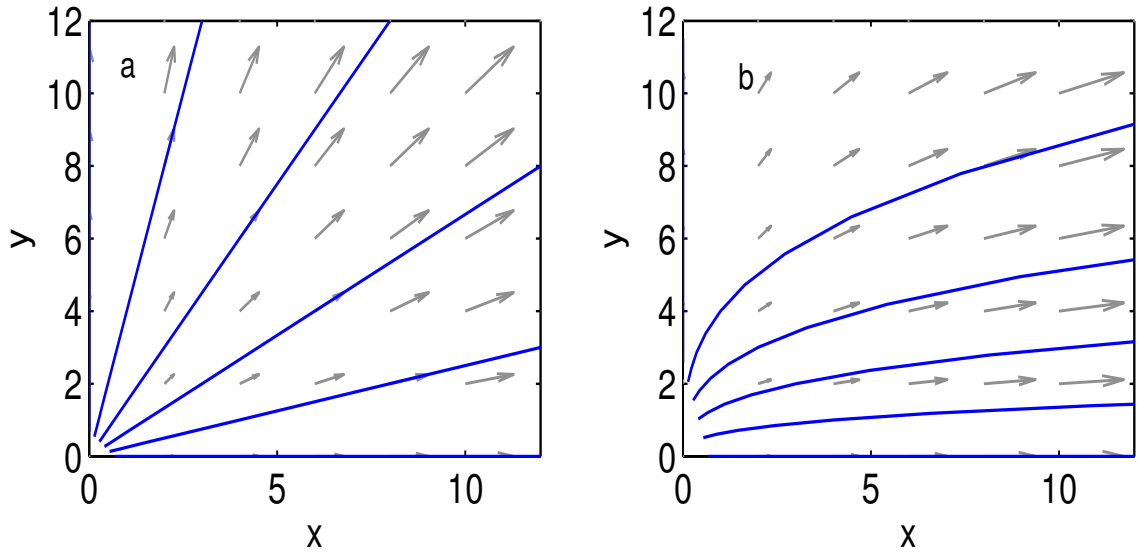

Figure 3: **(left)** Velocity field and streamlines (the family of blue, solid lines) for Eq. (5) at $t = 0$, and at $t = 1$ **(right)**. The velocity at a given point turns clockwise with time as the y-component of the velocity decreases with time.

and then integrated over the limits a to x, b to y, and t_o to t to yield the trajectory components,

$$x(a,t_o,t) \;=\; a\; exp(t-t_o) \qquad \text{and} \qquad y(b,t_o,t) \;=\; b\frac{(1+2t)^{1/2}}{(1+2t_o)^{1/2}}. \tag{6}$$

The y-component was seen also in Part 1, but here the initial time has been retained for use below.

Trajectories starting from a few different a and b are in Fig. 4. The Eulerian velocity is everywhere upward and to the right, and so it is no surprise that the trajectories do about the same thing, Fig. 3. The trajectories bend downward in time, consistent with the temporally-decreasing y-component of the velocity field. In a later section 2.5 we will see a case where the Eulerian and the Lagrangian mean flows are qualitatively different, and the trajectories could not have been anticipated in advance of an integration.

2.2 Backward trajectories

Trajectories are forward in time in that they show where a parcel released at a given point and time will be found at some later time due to transport by the velocity field. However, if we know the history of the velocity field, then this parcel tracking can be reversed to determine where a parcel observed at a given time and place came from. Let t_o be the present time, t_b be the time going backward, then $t' = t_o - t_b$ is the time in the past, and the origin of the parcel may be evaluated from

$$\tilde{\mathbf{x}}(t') \;=\; -\int_0^{t'} \mathbf{V}\left(\tilde{\mathbf{x}}(t'),t'\right) dt', \tag{7}$$

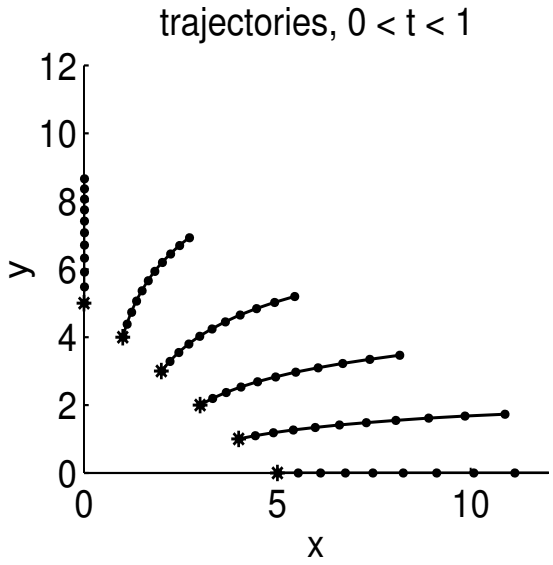

Figure 4: Trajectories of six parcels that were released into the flow given by Eq. (5). The sources are shown by asterisks. They were released at the same time, $t_o = 0$, and tracked until $t = 1$. Dots along the trajectories are at time intervals of 0.1. In this very simple flow, the trajectories are as you would expect from the Eulerian velocity field seen above. That will not always be the case with flows that have more complex time and space dependence.

and similarly for the $\tilde{y}$-component. This kind of backward trajectory calculation is the backbone of air quality studies that seek to determine the source of pollutants observed at a given site.[2]

The essential idea of a backward trajectory is that a given parcel position can be associated with a unique position at any previous time. This is plausible for advection by a resolved velocity field, but not when diffusion is also present. Diffusion effectively spreads the future position of a parcel over a domain that grows as the square root of time. Indeed, the notion of a discrete, trackable parcel and diffusion are somewhat incompatible, and better to think instead of the tracer value. In the presence of diffusion, the tracer value at a given time and place will depend upon some average of the tracer field over a domain that size of which increases with the elapsed time.

2.3 Streaklines are a snapshot of parcels having a common origin

Another useful characterization of the history of parcel positions is called a streakline, which shows the positions, at a fixed time, of all of the parcels which at some earlier time passed through a given point. A natural example of this is the plume of smoke coming from a point source located at $\mathbf{x}_p$ and recorded, say by a photograph taken at a time, t_p. The information needed to construct a streakline is contained within the trajectory, Eq. (6). To construct a streakline, release parcels one after the other from a fixed source. The first parcel is released at time $t_0 = 0$, and let the trajectory run until $t = t_p$, and then take a

[2]Examples are at https://www.arl.noaa.gov/hysplit/ and a very thorough tutorial on methods used to estimate backward trajectories from meteorolgical data is online at https://www.ready.noaa.gov/documents/Tutorial/html/index.html See also https://diginole.lib.fsu.edu/islandora/object/fsu:389481/datastream/PDF/view

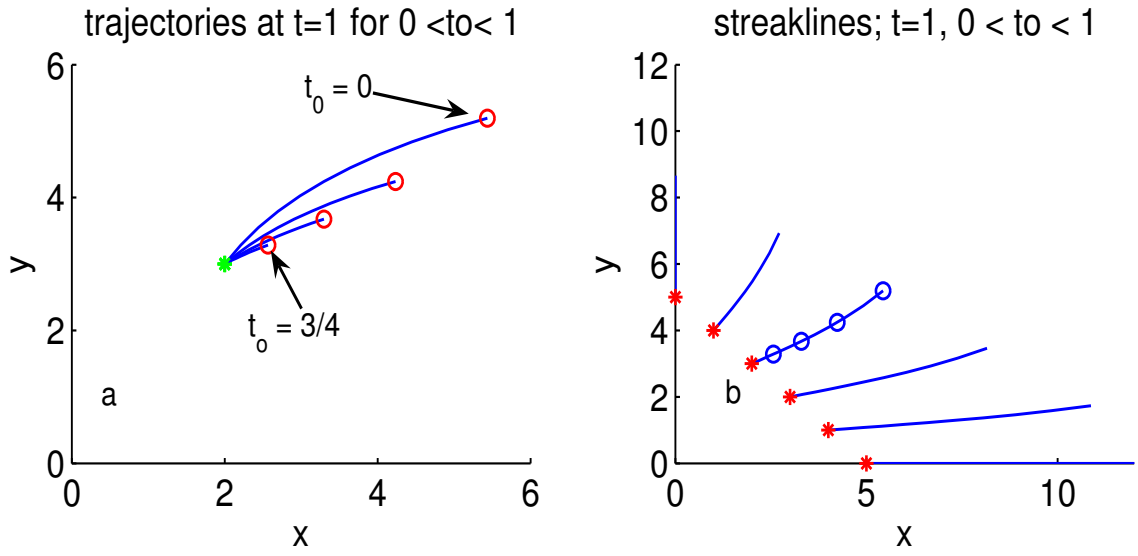

Figure 5: **(left)** Trajectories of five parcels that were released from a common source, (x,y) = (2,3), and tracked until $t = 1$. The parcels were released at different initial times, $t_0 = 0,\ 1/4,\ 2/4,\ 3/4$, and 1. The latter trajectory has zero length. The end points of the trajectories are the open circles, the locus of which forms a streakline. **(right)** Streaklines from several different sources. These streaklines start at $t_0 = 0$ and the 'photograph' was taken at $t_p = 1$. Notice that these streaklines end at the endpoint of the trajectories of Fig. 4 (they have that one point in common) but that streaklines generally have a different shape (different curvature) from the trajectories made over the same time range. In this figure and in previous ones (Fig. 2b) the two quantities being compared are only slightly different, and you might well wonder if, for example, streaklines are some kind of approximation to trajectories. The answer is no, in general, they are qualitatively different things.

photograph. The only data retained from this trajectory is the position at time $t = t_p$, i.e., record $\mathbf{x}(t_p, \mathbf{x}_p, t_0 = 0)$. A second parcel is released a little later, say at $t_0 = \frac{1}{4}$, and again let the trajectory run until $t = t_p$, keeping only the last position, $\mathbf{x}(t_p, \mathbf{x}_p, t_0 = \frac{1}{4})$. A third parcel is released at $t_0 = \frac{2}{4}$, and so on. It appears, then, that a recipe for making a streakline from a trajectory is to treat the initial time, t_0, as a variable, while holding t constant at t_p, and also the initial position at $\mathbf{x} = \mathbf{x_p}$. Several streaklines are in Fig. 5. Notice that in this time-dependent flow, trajectories and streaklines are not parallel.

2.4 Streamlines are parallel to an instantaneous flow field

Still another and widely useful method for depicting a velocity field is to draw the streamlines, a family of lines that are everywhere parallel to the velocity. Time is fixed, say at $t = t_f$, and thus streamlines portray the direction field of a velocity field, with no reference to parcels or trajectories or time-dependence of any sort. There is more than one way to construct a set of streamlines, but a method that lends itself to generalization is to solve for the parametric representation of a curve, $\mathbf{x}(s)$ that is everywhere parallel to the velocity;

$$\boxed{\frac{d\mathbf{x}}{ds} = \mathbf{v}(t_f, x, y)} \tag{8}$$

or in components;

$$\frac{dx}{ds} = u(t_f,x,y); \quad \frac{dy}{ds} = v(t_f,x,y). \tag{9}$$

A suitable initial condition is $x(s_0) = x_0$, etc. Notice that s is here a dummy variable; any other symbol could be used, but s is conventional.[3] $\mathbf{x}$ is the position of a point on a line, where just above $\mathbf{x}$ meant the position of a parcel. This reuse of symbols is risky practice, but it is also almost unavoidable. Given the velocity components Eq. (5), these equations are also readily integrated to yield a family of streamlines:

$$x = x_0\, exp(s-s_0); \quad y = y_0\, exp\left(\frac{s-s_0}{1+2t_f}\right), \tag{10}$$

and recall that t_f is the fixed time chosen to draw the streamlines. The integration constants may be chosen so that a given streamline will pass through an arbitrary position. There is no rule for choosing these positions; in Fig. 3 there were five positions chosen arbitrarily, and then s was varied over sufficient range to sweep through the domain. Other streamlines could be added if needed to help fill out the picture. No particular value is attached to a given streamline. The streamline's sophisticated cousin, the streamfunction, has isolines that are also parallel to velocity, and which are assigned values that are directly related to the speed of the flow and the distance between streamlines.

2.5 Tracking parcels around a steady vortex given limited Eulerian data

The previous sections developed the formal methods needed to transform Eulerian velocity (Lagrangian) trajectories and other variables that help depict properties of a fluid flow. An understanding of the formal steps is important, of course, but the ease with which those transformations were made resulted from the assumption of a very simple closed solution for the Eulerian velocity — not something you are likely to encounter outside of a homework problem. In practice, partial and incomplete information is the norm, and so this section will consider an approximate analysis method based upon an expansion of the velocity field in Taylor series. This yields results that are interesting and important of themselves, especially the notion of Stokes drift that will come up in Sec. 2.6.

The power and the limitations of the Taylor series method can be appreciated by analysis of parcel motion in a steady, irrotational vortex in R^2. The radial and azimuthal velocity components of such a vortex are

$$\mathbf{V} = \begin{pmatrix} u_r \\ u_\theta \end{pmatrix} = \begin{pmatrix} 0 \\ \frac{C}{2\pi r} \end{pmatrix} \tag{11}$$

where r is the distance from the vortex center. The $1/r$ dependence of the azimuthal speed is the distinguishing feature of an irrotational vortex. C is a constant, termed the circulation,

$$C = \oint \mathbf{V}\cdot d\mathbf{s},$$

[3]The notion of a parameterized curve is central to the method of characteristics discussed in Part 1, Sec. 4. The parameter s could be regarded as time, with care not to confuse this use of time with the time-dependence of the velocity field (which is suppressed while drawing a map of streamlines). This helps make clear that streamlines are parallel to parcel trajectories in steady flows, and, are also the characteristics of the advection equation.

where $d\mathbf{s}$ is the vector line segment along a path that encloses the vortex center and that is traversed in an anti-clockwise direction. C measures the vortex strength, and without loss of generality we can set $C = -2\pi$ to define a vortex that rotates clockwise, Fig. (6). Parcel trajectories in this steady vortex will be circular, and a parcel will make a complete orbit in a time $T = (2\pi r)^2/C$. The Cartesian velocity components of the vortex are

$$\begin{pmatrix} u \\ v \end{pmatrix} = \frac{C}{2\pi r}\begin{pmatrix} \sin\theta \\ \cos\theta \end{pmatrix} \tag{12}$$

where $r = (x^2 + y^2)^{1/2}$ and the angle $\theta = \text{atan}(y/x)$ is measured counter-clockwise from the x-axis.

An irrotational vortex is an idealization of the vortex flow produced by the convergent flow into a drain or the starting vortex left behind an accelerating airfoil. These vortices have several interesting properties that will be considered in later sections (including why they are said to be irrotational). For now, (12) makes a convenient flow into which floats and current meters may be inserted in order to investigate kinematics.

2.5.1 The zeroth-order approximation, or PVD

For the sake of this development, imagine that the only thing known about this vortex is the velocity observed at one fixed site, say $(x,\ y) = (0,\ 1)$. The velocity observed at this fixed site, $\mathbf{V}_0 = \mathbf{V}(x,\ y)$ is, of course, an Eulerian velocity, and is a steady, uni-directional flow having Cartesian components $(U_0,\ V_0) = -(C/2\pi r,\ 0) = (1,\ 0)$. What, if anything, can be inferred about parcel trajectories from this very limited data?

If no other information was available, then out of desperation one might estimate a pseudo-trajectory, called a progressive vector diagram, or PVD, by integrating this Eulerian velocity in time as if it were the Lagrangian velocity of a moving parcel,

$$\delta\mathbf{x}_0 = \int \mathbf{V}(x_o, t)\, dt = \begin{pmatrix} U_0\, t \\ 0 \end{pmatrix}. \tag{13}$$

It is essential to understand that (13) is wrong, formally, as it completely misses the distinction between Lagrangian and Eulerian velocity (you would never do that, would you?).

It is fruitful to think of the PVD estimate as a zeroth-order approximation of a true trajectory. The PVD in this case indicates a linear, pseudo-trajectory, consistent with the velocity observed at the fixed site, Fig. (6), dotted line. A PVD is a useful way to visualize a current meter record or a wind record insofar as it gives a direct measure of how much fluid has gone past an observation site. Is there any flow condition under which a PVD could be interpreted as if it were a true, parcel trajectory? Yes, a PVD would represent a true trajectory if the Eulerian velocity field was spatially uniform. Observations made at any position would then be equal to observations made anywhere else, including at the moving position of a parcel. A spatially uniform flow is a degenerate case of little practical interest, but this helps to show that the issue is the spatial variation of the flow.

From the example of a steady vortex flow of Fig. (6), it would appear that the PVD is a reasonable estimate provided that the inferred displacement is considerbly less than the horizontal scale, L, over

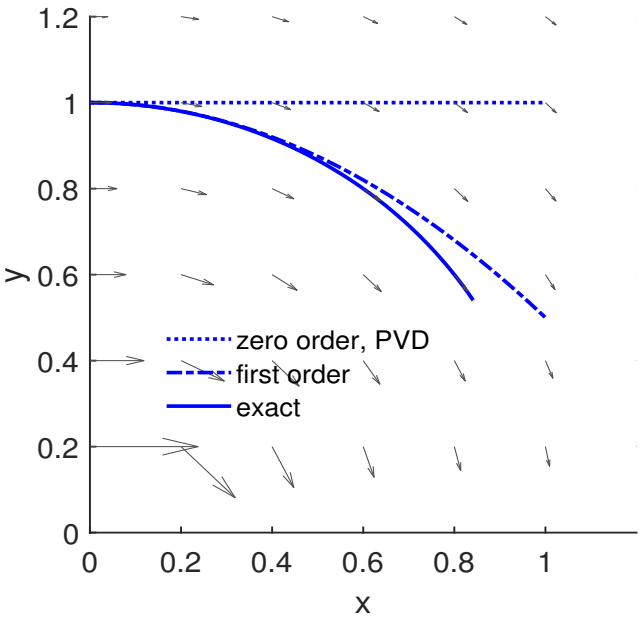

Figure 6: Parcel tracking around an irrotational vortex. A parcel was launched at $(x,y) = (0,1)$ and tracked up to $\delta t = 1$. The exact trajectory (solid line) is easily computed in cylindrical coordinates. The zeroth order approximation, or PVD, in which the Eulerian velocity measured at the fixed observation site (where $U_\theta = 1$) has been integrated as if it were the Lagrangian velocity, is the dotted line and has a net displacement $\delta x_o = 1$. The PVD starts off well enough, but begins to diverge noticably from the exact trajectory after the displacement exceeds about 0.1. The first order trajectory (dash dot line) accounts approximately for the spatial variation of the velocity and is somewhat better than the PVD, but it too becomes rather inaccurate as the displacement becomes comparable to the length scale of the flow, L, in this case the distance to the vortex center, $L = 1$.

which the flow changes significantly. This condition could be written

$$\delta x_0 \approx U\, t_a << L,$$

with U the speed and t_a the advection time, or

$$\frac{t_a\, U}{L} << 1.$$

An advection time that satisfies this condition will be called the short time advection approximation, since time (rather that U or L) is likely to be the independent variable. By inspection, the horizontal scale of this vortex flow is estimated to be the radial distance to the vortex center, $L = 1$ at the site chosen, and $U = 1$, as well. Hence the PVD pseudo-trajectory makes a reasonable estimate of the actual trajectory for times $t_a \leq 0.1$, which is 1/10 of the elapsed time shown in the trajectories of Fig. (6). In problem 4) below, the error of the PVD (defined as distance to the trajectory) will be estimated as $\delta t^2/2$ and so $\delta t \leq 0.1$ should be acceptable for many purposes.

2.5.2 The first order approximation

Evidently we can not get far from the starting point knowing only the velocity at that one point, so let's give ourselves another piece of information, the velocity gradients, but only at the starting point. With

this new piece of data we can take some account of the spatial variation of the velocity. The plan is to represent the velocity field in the vicinity of the stating point by expanding in a Taylor series, here for each component separately,

$$\begin{aligned} u(x,y) &= u_0 + \frac{\partial u}{\partial x}\delta x + \frac{\partial u}{\partial y}\delta y + HOT, \\ v(x,y) &= v_0 + \frac{\partial v}{\partial x}\delta x + \frac{\partial v}{\partial y}\delta y + HOT, \end{aligned} \tag{14}$$

where (u_0, v_0) is the velocity observed at the starting point, the partial derivatives are evaluated at the same point, and HOT is the sum of all the higher order terms that are proportional to $\delta x^2, \delta x^3$, etc. In effect, this presumes knowing not only the velocity but also the (spatial) partial derivatives of velocity, though at one position only. It is convenient to use a vector and tensor notation to write equations like these in a form

$$\mathbf{V}(x,y) = \mathbf{V}_0 + \mathbb{G}\cdot\delta\mathbf{x} + HOT, \tag{15}$$

where $\mathbb{G}$ is the velocity gradient tensor encountered in Sec. 3, Part 1, and repeated here for the two-dimensional case at hand,

$$\mathbb{G} = \begin{pmatrix} \dfrac{\partial u}{\partial x} & \dfrac{\partial u}{\partial y} \\ \\ \dfrac{\partial v}{\partial x} & \dfrac{\partial v}{\partial y} \end{pmatrix}$$

$\mathbb{G}$ is a device to streamline notation; when we (matrix) multiply $\mathbb{G}$ into a displacement vector (written as a column vector), the result is the velocity difference that corresponds to that displacement vector.[4] It is easy to see that if the displacement vector was doubled or halved, then the result would be twice or half the velocity difference. Thus, multiplication by a velocity gradient tensor serves to make a linear transformation on a displacement vector. In general, the result will be a velocity difference vector having a different direction from that of the displacement vector, and of course it has a different amplitude and different physical dimensions as well. The velocity gradient tensor evaluated at the observation site

[4] **G** is a Cartesian tensor for which the multiplication rules are the same as that of matrices. This raises the question — is there a difference between a matrix and a tensor? A matrix is more general in that the elements can be pretty much anything. A matrix is usually an array of numbers that have a relationship to some other matrix (or vector) so that the rules of matrix multiplication, addition, etc., yield the desired form. There are no restrictions on what the matrix elements represent: there could be elements representing temperature and savings account balance in the same matrix. There is no implied rule that specifies how the matrix elements should change if the scale or system of units should change, say Farenheit to Centigrade and dollars to euros. On the other hand, a tensor is intended to represent a physical quantity having a geometric significance and thus a magnitude and a direction. The elements of a velocity gradient tensor have a crucially important dependence upon a coordinate system. For example, if rectangular coordinate axes are rotated 45 degrees clockwise, then the elements of the velocity gradient tensor must rotate 45 degrees anti-clockwise so that the velocity shear, which has a physical meaning, is invariant to the arbitrary orientation of the coordinate system. The elements of a velocity gradient tensor are thus said to be contravariant with respect to the unit vectors of the coordinate system. No such transformation rule is implied for the elements of a matrix.

$(x_s,\, y_s) = (1,\, 0)$ has a simple form

$$\mathbb{G} \;=\; \frac{C}{2\pi}\begin{pmatrix} 0 & 1 \\ 1 & 0 \end{pmatrix} \;=\; \begin{pmatrix} 0 & -1 \\ -1 & 0 \end{pmatrix},$$

where recall we have taken $C = -2\pi$.

The PVD approximation amounts to an integration of the first term only of the Taylor series, while ignoring the spatial variation of the velocity altogther. Since this approximation omits all terms that are first and higher power in the displacement, the PVD is termed the zeroth order, pseudo-trajectory. The first order trajectory, i.e., the first correction to the trajectory, can then be computed by dropping the HOT from Eq. (15), and approximating

$$\delta\mathbf{x}_0 \;=\; \int \mathbf{V}_0\, dt$$

and integrating in time,

$$\delta\mathbf{x}_1 \;=\; \delta\mathbf{x}_0 \;+\; \mathbb{G}\cdot\mathbf{V}_0 t^2/2. \tag{16}$$

This gives a considerable improvement upon the zeroth-order PVD (Fig. 6), the dot-dash line. If our interest was limited to short times only, then this might make a useful approximate solution for a trajectory. However, after sufficient time has passed and the displacement becomes comparable to the length scale of the flow, the radius of the vortex, then this first order pseudo-trajectory also accumulates a noticeable error. Adding an evaluation of the next term of the HOT would delay the failure, in general, but in any steady vortex flow the displacement will eventually carry a parcel a long distances from its origin. One way to describe this shortcoming is that approximation methods built around a Taylor series expansion are not uniformly valid in time when applied to a steady vortex flow.

2.6 Tracking parcels in water waves

The notion of such a pseudo-trajectory may be applied fruitfully to a wavelike motion in which the parcel displacements during a wave passage are small compared to the wavelength. Consider a surface gravity (water) wave having a surface displacement

$$\eta(x,t) \;=\; a\cos(kx-\omega t), \tag{17}$$

where a is the amplitude of the surface displacement, $k = 2\pi/\lambda$ is the wavenumber given the wavelength λ and ω is the wave angular frequency (it is assumed that ω and $k > 0$). The argument of the trigonometric function shows that this surface displacement moves rightward as a progressive wave having a phase speed $c = \omega/k$. The two-dimensional and time-dependent velocity field associated with this wave

$$\mathbf{V}(x,z,t) \;=\; Ue^{kz}\begin{pmatrix} \cos(kx-\omega t) \\ \sin(kx-\omega t) \end{pmatrix}, \tag{18}$$

where z is the depth, positive upwards from the surface. The amplitude or speed at the surface is $U = a\omega$ and decays with depth on an e-folding scale $1/k$. This exponential decay with depth is appropriate for a wave whose wavelength is less than the water depth, a so-called deep water wave. If the wavelength is

much greater than the water depth, in which case a shallow water wave, the x component of the velocity is approximately independent of depth and the z component is linear with depth and vanishes at the (flat) bottom.[5]

2.6.1 The zeroth order approximation, closed loops

The (Eulerian) velocity observed at a fixed point is a rotary current, often called the wave's orbital velocity, of amplitude $a\omega e^{kz}$ that turns clockwise with time at the angular frequency ω (assuming that x increases to the right). Given the known velocity the PVD-like parcel displacements are estimated by integrating $\mathbf{V}(x,z,t)$ with respect to time while holding x and z constant,

$$\delta\mathbf{x}_0 \;=\; ae^{kz}\begin{pmatrix} -\sin(kx-\omega t) \\ \cos(kx-\omega t) \end{pmatrix}. \tag{19}$$

The PVD indicates that parcels move in a closed rotary motion with each wave passage and that the net motion is zero, consistent with the wave-average of the Eulerian velocity.

The analysis of motion around a vortex suggests that this PVD for a gravity wave would probably give a fairly accurate prediction for the actual parcel displacements provided that the parcel displacements were much, much less than the scale over which the wave orbital velocity varies. In this case the scale is k^{-1} in either direction, so that this condition is equivalent to requiring that the wave steepness, $ak = 2\pi a/\lambda$ must be much less than 1. This is also the condition under which the linear solution gives an accurate waveform of the surface displacement, a pure sinusoid, which we have assumed with Eq. (17).

2.6.2 The first order approximation, Lagrange = Euler + Stokes

However, it is dubious that this zeroth order approximation of the trajectories can tell us anything reliable about the actual trajectories, and so let's proceed to calculate the first order velocity via Eq. (15). The velocity gradient tensor for this wave is just

$$\mathbb{G} \;=\; a\omega k e^{kz}\begin{pmatrix} -\sin(kx-\omega t) & \cos(kx-\omega t) \\ \cos(kx-\omega t) & \sin(kx-\omega t) \end{pmatrix}$$

[5] An excellent introduction to surface gravity waves is 'Water Wave Mechanics for Engineers and Scientists', by R. G. Dean and R. A. Dalrymple, World Scientific Pub. Co., 1991. For Stokes drift in particular see also Longuet-Higgins, M. S., 1969. 'On the transport of mass by time-varying ocean currents'. *Deep-Sea Res.*, **16**, 431-447 and Longuet-Higgins, M. S., 1986. 'Eulerian and Lagrangian aspects of surface waves', *J. Fluid Mech.*, **173**, 683-707.

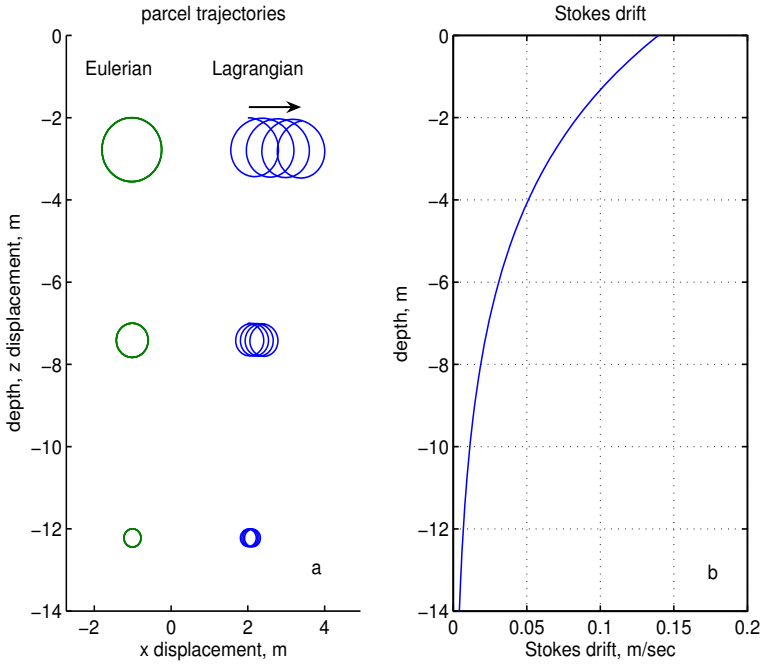

Figure 7: **(left)** Parcel trajectories underneath a deep-water, surface gravity wave that is presumed to be propagating from left to right. The amplitude of the surface displacement was taken to be $a = 1$ m and the wavelength $\lambda = 50$ m. The Eulerian trajectories (or PVDs) are closed circular orbits around which the parcels move clockwise. The Lagrangian trajectories were computed by integrating numerically for four periods (= 22.6 sec) and are open loops indicating there is a net drift of fluid parcels from left to right (shown as an arrow). **(right)** Stokes drift for this wave computed from Eq. (20). An animation of a gravity wave and parcel trajectories is linked in the next figure.

and matrix-multiplying into the zeroth order displacement given by Eq. (19) gives the first order velocity (insofar as the HOT have been dropped),

$$\begin{aligned} \mathbf{V}_1(z) &= a^2\omega k e^{2kz}\begin{pmatrix} \sin^2(kx-\omega t)+\cos^2(kx-\omega t) \\ 0 \end{pmatrix} \\ &= Uake^{2kz}\begin{pmatrix} 1 \\ 0 \end{pmatrix}, \end{aligned} \tag{20}$$

where recall $U = a\omega$ is the amplitude of the orbital velocity at the surface. The coefficient $Uak = a^2k^2c$ is the wave steepness squared times the phase speed. This velocity is independent of time and x, and so the first order displacement is easily computed,

$$\delta\mathbf{x}_1(z) = \mathbf{V}_1(z)t, \tag{21}$$

where there is no particular initial position. Notice that this formula relates the displacement of a parcel to a depth, i.e., a field coordinate, so that it gives a field representation of a Lagrangian property.

Quite unlike the PVD, Eq. (21) indicates that fluid parcels have a substantial net motion in the

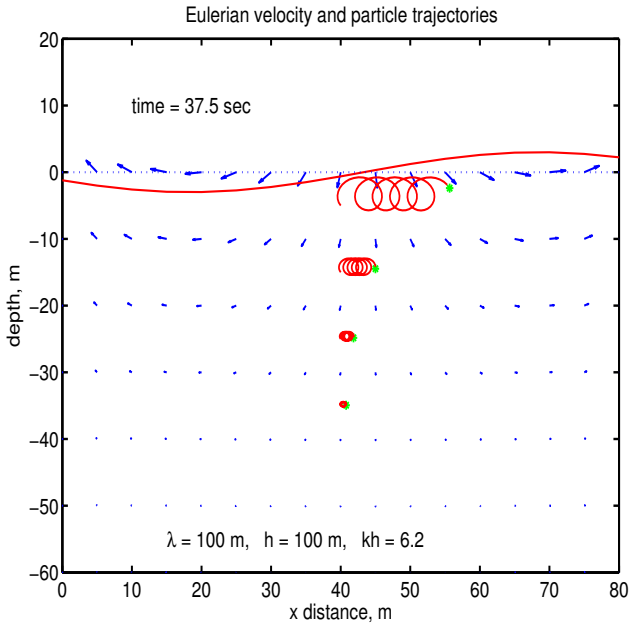

Figure 8: A surface gravity wave propagating from left to right as computed on linear theory. The wave orbital velocity is the array of vectors and the sinusoidal red line is the free surface. This is a rather steep wave: the wave angular frequency ≈ 1 s^{-1}, the surface displacement is 3 m, the wavelength is 100 m in a water depth of 100 m. The spiralling red lines are the trajectories of parcels computed numerically. Notice that parcels have a mean motion to the right, in the direction of the wave propagation, Stokes drift. An animation is available at https://www2.whoi.edu/staff/jprice/wp-content/uploads/sites/199/2022/06/gwavemovie.mp4

direction of the wave propagation, often called Stokes drift or mass transport velocity, that is a fraction $2\pi\frac{a}{\lambda}e^{kz}$ of the orbital motion amplitude. For example, for a wave having an amplitude of $a = 1$ m and wavelength of $\lambda = 50$ m, the orbital motion at the surface is about 1.11 m s^{-1} where the Stokes drift is about 0.14 m s^{-1}. The Stokes drift decreases rapidly with depth, about twice as fast as does the wave orbital velocity.

The vertically integrated Stokes drift is the mass transport per unit length,

$$M = \rho \int_{-\infty}^{0} \mathbf{V}_1(z)dz = \begin{pmatrix} \rho U a/2 \\ 0 \end{pmatrix},$$

and also the momentum per unit area associated with the wave. The kinetic energy per unit area of the wave motion is

$$K = \rho \int_{-\infty}^{0} \mathbf{V}(z)^2 dz = \rho U c a/4.$$

Thus the momentum in the direction of gravity wave propagation and the kinetic energy of gravity waves are related by the particle-like relation

$$M = \frac{2K}{c},$$

which holds for other kinds of waves, e.g., electromagnetic waves, that have genuine momentum.[6] Thus, the Stokes drift turns out to be much more than a residual effect of switching from an Eulerian to a Lagrangian coordinate system and indeed it is one of the most important means by which surface gravity waves interact with other scales of motion.[7] It is notable that all of the information needed to calculate the Stokes drift was present in the Eulerian velocity field, Eq. (18). However, to reveal this important phenomenon required an analysis that was explicitly Lagrangian, i.e., that tracked parcels over a significant duration.

Two comments regarding the Stokes drift. First, it has been estimated as the product of two terms that are derived from a linear solution, the velocity gradient tensor and the PVD displacement, and is thus 'bilinear'. The amplitude of the Stokes drift is proportional to the wave amplitude squared. This seems to imply that the Stokes drift estimated from a nonlinear wave might be rather different from that calculated here. We don't intend to carry this calculation any further, but will simply note that this is not the case, assuming only that the nonlinear wave is not grossly distorted from the linear solution. A nonlinear correction to the linear solution gives only a nonlinear correction squared (and probably very small) to the Stokes drift. Second, the Stokes drift can be envisaged as the difference between the time-integral of the Eulerian and Lagrangian velocities in the sense that, averaged over a wave, the various fluid velocities can be imagined related by Euler + Stokes = Lagrange (see Longuet-Higgins of footnote 5, and in the surface wave case, Euler = 0). This stands in marked contrast to the FPK which, recall, applies to the *instantaneous* velocity. Thus Stokes drift arises from time-averaging or integrating, which most observation techniques necessarily do, of course, if only to yield data sets of a manageable size. In other cases, averaging may arise as an inevitable byproduct of the sampling procedure. In either event, the formal FPK may not apply.

2.7 Key ideas

1) Most models in fluid mechanics are Eulerian, and their solutions are defined on a finite grid of spatial coordinates (numerical models) or a continuous field (analytic models). Given complete Eulerian data of this kind it is more or less routine to compute the trajectories of fluid parcels.

2) Calculation of a trajectory from Eulerian data will almost always involve solving an implicit equation or integral: To know where you are going, you have to know where you are.

[6] Waves that exist on a physical medium need *not* have a genuine momentum of this sort, though they will have a momentum flux, see M. E. McIntyre, 'On the wave momentum myth', *J. Fluid Mech.*, **106**, 331-347, 1981. An excellent recent reference on the topic of wave momentum is by D. Rowland, 'Comments on "What happens to energy and momentum when two oppositely-moving wave pulses overlap?"', *Am. J. Phys.*, **72**(11), 1425-1429, 2004. Surface gravity waves have momentum by virtue of the displaced free surface. Here's a small problem for you: show that the Eulerian mean momentum over the water column is equal to the mass transport associated with Stokes drift by making the same kind of (bilinear) approximation for transport that we made for Stokes drift, i.e., assume that the wave velocity $\mathbf{V}$ under the displaced surface is given by Eq. (26) evaluated at $z = 0$, and compute the wave mean of $\eta\mathbf{V}$.

[7] Stokes drift will transport fluid properties as well as any material, e.g., plankton, that are suspended in the fluid. The role of Stokes drift in ocean circulation and ocean ecology is an active topic in ocean science, see McWilliams, J.C. and J.M Restrepo, 'The wave-driven ocean circulation.' *J. Phys. Oceanogr.* **29**, 2523-2540, 1999.

3) Advection alone (without diffusion) is reversible in time. Given the history of the Eulerian velocity, it is possible to compute backwards trajectories that show where fluid came from.

4) Streaklines are the locus of the trajectories that started at a given point but at different times (as in a smoke plume from a fixed, ongoing source).

5) If only limited information is available to define a velocity field, then the estimation of a trajectory will be compromised to some degree. The most extreme example, known as a progressive vector diagram, integrates the velocity observed at a fixed site to compute a pseudo-trajectory, or PVD. A PVD may be a useful approximation to the true Lagrangian trajectory originating from a given point, for short times, $t_a U/L << 1$.

6) The next approximation, utilizing the partial derivatives of velocity, does somewhat better than a PVD, but also fails once the integration time yields a displacement that is comparable to the dominant spatial scale of the velocity field.

7) There is no general relation between the pseudo-trajectories noted above and genuine Lagrangian trajectories observed for long times/large displacements. This is a corollary of 2) above: To know where you will be in the medium- or long-term future, you will have to know where you are at each step of the journey.

8) Parcel trajectories in the presence of wave motion may show a significant mean flow that results from a correlation of parcel displacement and the wave propagation. In the case of surface water waves, there can be a significant Lagrangian mean flow in the direction of the wave propagation, Stokes drift.

2.8 Problems

1) There is an important family anniversary event coming up, and your big idea is a balloon flight for the entire family. You had better get this right. Start with a visit to the HYSPLIT web site, https://www.ready.noaa.gov/HYSPLIT.php and under the READY menu banner select Balloon flight forecasting tools. As you will soon discover, HYSPLIT is not a homework toy model, but rather a comprehensive and sophisticated forecasting tool that will require a little effort on your part. You will be queried for the parameters of a simulated balloon flight that can be forecast ahead for a few days. Define the launch site to be your present position, and choose a height 2000 meters above the ground. Compute the forecast for a flight of, say 48 hours. Did the balloon carry you some place you might want to go? If not, try varying the altitude of the balloon, and the launch time/date, and see if you can come closer to a desirable or at least a safe, dry termination. How sensitive is the trajectory to the launch position?

2) Given the irrotational vortex flow of Sec. 2.5.1, show that the PVD approximation has an error (defined as the distance to the corresponding point on the actual trajectory) that is due almost entirely to the y component of the displacement. Show too that for short integration times, the error increases as δt^2, and hence that $t_a U/L << 1$ makes a plausible bound on the acceptable error of a PVD. Suppose that the launch site for the PVD is taken to be $(x,\ y) = (0,\ 0.2)$, which is much closer the vortex center than the site chosen in Sec. 2.5.1. How does the time t_a change in that case?

3) Stokes drift is a very robust phenomenon that can be produced and observed with quite modest means: fill a flat container with water to a depth of about 2-4 cm. A bath tub works well, but even a large cake pan will suffice. To make gravity waves use a cylinder having a diameter of roughly the water depth and a length that is about half the width of the tank. Oscillate the wave maker up and down with a frequency that makes gravity waves and observe the motion of more or less neutrally buoyant particles; some that float and others that sink to the bottom. You can easily vary three things, the amplitude of the waves, the depth of the water, and the width of the wave maker. Are the waves in your tank shallow water or deep water waves? Describe the mean flow (if any) set up by the oscillating wave maker, and how or whether it varies with the configuration of the tank and wave maker.

4) Suppose that the one-dimensional velocity in a progressive wave is given as $Ucos(kx-\omega t)$. Calculate the Stokes drift approximation of the mean parcel motion in this wave, and compare the result to the numerical integration of the full trajectory equation, i.e., $dx/dt = Ucos(kx(t)-\omega t)$. This requires a small program or script and can be accomplished with a rather crude numerical method. For what range of wave steepness does the Stokes drift estimate give an accurate estimate of the mean flow? Why do parcels have a Stokes drift in this wave?, i.e., explain why parcels in this wave velocity field have a net motion. What happens at large steepness? How does this compare with your observations from the bath tub? How does this compare with the Stokes drift of a deep water gravity wave?

5) Suppose that you can make perfect Lagrangian measurements at arbitrarily fine temporal resolution. How would you use these data to construct the corresponding Eulerian velocity field? Now suppose, more realistically, that your Lagrangian measurements are averages over some finite time interval, say many wave periods in a case where surface gravity waves are present. How would you (or could you) construct the corresponding Eulerian velocity field from those data?

3 Rotation and deformation of fluid parcels

You have likely noticed that advection by a real fluid flow does much more than simply translate parcels from place to place; the swirling flow in a teacup will cause a tracer patch (a macroscale parcel) to rotate, and will draw out a tracer patch into a long, thin streak. This rotation, and the change in shape, called a deformation, can have significant consequences.

To pose a definite problem, consider the motion of a tracer patch that is released into a steady, clockwise rotating, vortical flow; first a solid body rotation, in which the azimuthal speed increases with radius as r

$$\textbf{solid body vortex}, \quad \mathbf{V} = (u_r, \ u_\theta) = (0, \ \Omega_o \, r), \tag{22}$$

where Ω_o is the rotation rate, and then an

$$\textbf{irrotational vortex}, \quad \mathbf{V} = (u_r, \ u_\theta) = (0, \ \frac{\Omega_o \, r_o^2}{r}), \tag{23}$$

in which the azimuthal velocity decreases with r as is $1/r$. There is no radial velocity in either vortex. The rotation rate at $r = 1$ was taken to be $\Omega_o = -1$, which is clockwise, and $r_o = 1$.

These vortex flows are idealizations, and yet with a little effort (imagination?) something akin to both kinds of vortices can be observed in the flow in a teacup: more or less irrotational vortices are

observed to spill off the edges of a spoon that is pushed through the fluid, and at longer times the azimuthal motion that fills the teacup may approximate a solid body rotation (except near the edges).[8]

The first task is advect the tracer with these velocity fields. Given the azimuthal symmetry of these vortex flows, it is desirable to calculate the tracer advection in polar coordinates $(r,\ \theta)$. The polar coordinates of the points $(x_b,\ y_b)$ that define the boundary of the tracer patch were computed from the usual,

$$r_b \ = \ \sqrt{(x_b^2 + y_b^2)} \ \text{ and } \ \theta_b \ = \ \text{atan}(y_b, x_b).$$

The radius is unchanged by the purely azimuthal vortex flows, while the angle θ changes at the rate $\Omega(r)$ appropriate to the r and vortex model,

$$r_b^{i+1} \ = \ r_b^i \quad \text{and} \quad \theta_{\rm b}^{\rm i+1} \ = \ \theta_{\rm b}^{\rm i} \ + \ \delta {\rm t}\, \Omega({\rm r}), \tag{24}$$

with $(\ \ )^i$ the i-th time, and δt is a small time step. The solution for $r(t)_b$ and $\theta(t)_b$ is, in effect, a characteristic for the parcel b, and can be computed as far out in time as needed. Since there is no diffusion or source (the flow is adiabatic), the tracer is constant in time along the charateristics (Sec. 4, Part 1).

The tracer is transported clockwise in both vortices (Fig. 9) as expected from the sign of Ω; there is nothing quite as surprising as Stokes drift (Sec. 2.5) that can make the Lagrangian mean flow (the long term displacement of a parcel) qualitatively different from the Eulerian mean flow (what you would guess given the velocity field). Aside from that, the effects of advection are remarkably different. The solid body rotation (Fig. 9, left) leaves the shape of the tracer patch unchanged, while the orientation changes at the rate $-\Omega$ that characterizes the rotation rate of the entire vortex. The irrotational vortex (Fig. 9, right) produces a strong deformation of the tracer patch, but leaves the average orientation of the tracer patch unchanged (hard to see this given the large deformation) The area of the tracer patch is unchanged in either case.

These changes in the orientation and shape of the tracer patch are due solely to advection by the velocity *field*, Eqs. (22) and (23). The goal of this section is to find out what specific properties of a velocity field are relevant. Here again we are asking for an explanation of Lagrangian properties — the size, rotation rate and shape of a fluid material volume — in terms of the Eulerian velocity field, $\mathbf{V}(x,y)$.

[8]These vortex models are very useful, despite that they each have unphysical properties in the limit of small or large r. The irrotational vortex has a singularity in u_θ at $r = 0$, while the u_θ of a solid body rotation grows linearly and without bound with r. A hybrid made from these two idealizations — solid body rotation near the center of a vortex, Eq. (22), matched to an irrotational profile $u_\theta(r)$ from Eq. (23) at some larger r — avoids both problems. This is called a Rankine vortex, and can make a convenient, first approximation to some real vortices, e.g., a hurricane. A time-dependent, viscous model of an irrotational, point vortex, called the Lamb-Oseen vortex, shows the evolution into a Rankine vortex, Sec. (4.5).

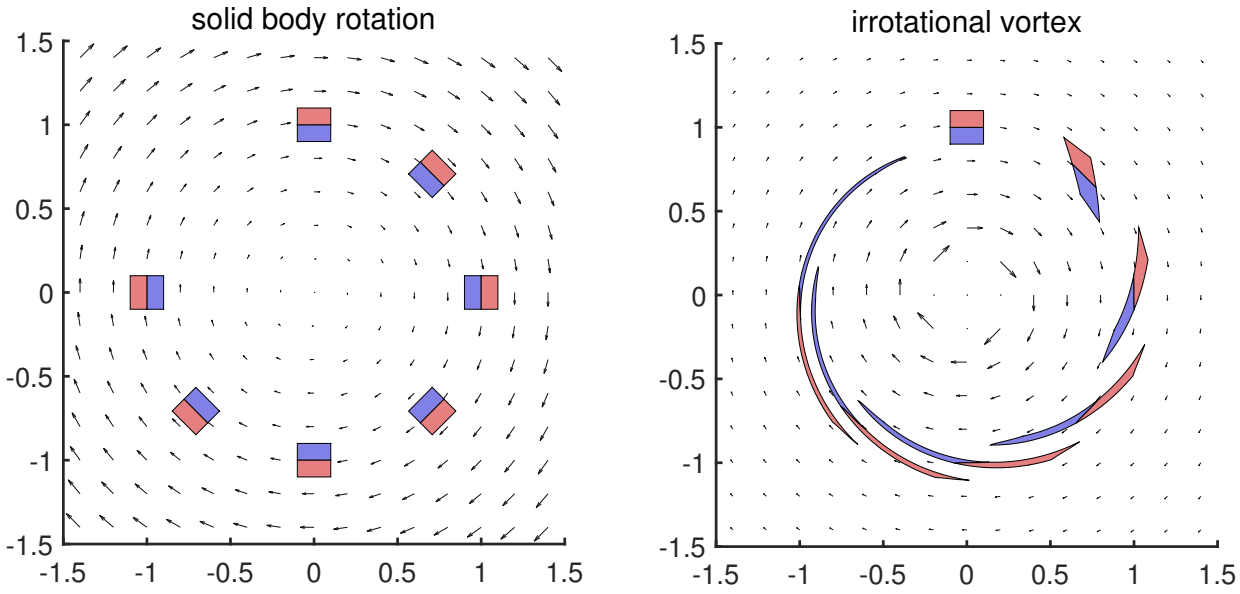

Figure 9: A small, square patch of a bi-colored, passive tracer (length 0.2 on each side) was released into a steady, clockwise rotating vortex and advected through 3/4 of a full revolution. The tracer patch is plotted at sucessive time intervals $\pi/4$. **(left)** This vortex is a solid body rotation. The patch rotated, but the area and shape were unchanged. **(right)** In this experiment, the vortex was irrotational. Advection carried the tracer patch clockwise around the vortex center just as before, and it also deformed the tracer patch into a long, thin filament. Nevertheless, this tracer patch did not rotate. Area was conserved as before.

3.1 The simplest shear flow

The specific goal of this section is to understand the tracer evolution seen in Fig. (9). To develop the tools needed for this, it will be helpful to start with the simplest possible shear flow,

$$\mathbf{V}(x,y) = \begin{pmatrix} u \\ v \end{pmatrix} = \begin{pmatrix} V_0 + \beta y \\ 0 \end{pmatrix} \tag{25}$$

This flow is homogeneous in that the shear is $\partial u/\partial y = \beta = 0.7$ and constant in time and space (the units of shear are time^{-1}, which may be left unspecified for the present). The mean velocity, $V_0 = 0.5$. An initially square tracer patch embedded in this flow evolves as shown in Fig. (10); the tracer patch is translated to the right, rotated clockwise, and deformed into a parallelogram. The translation is, of course, due to V_0, and the rotation and deformation are evidently related to the velocity shear.

For short times (small displacements) the Eulerian velocity field around a given point, $(x_0,\ y_0)$ may be approximated by the first terms of a Taylor expansion (as in Sec. 2.5 and repeated here),

$$\mathbf{V}(x,y) = \mathbf{V}_0(x_0,y_0) \ + \ \mathbb{G}\cdot\delta\mathbf{x} \ + \ HOT, \tag{26}$$

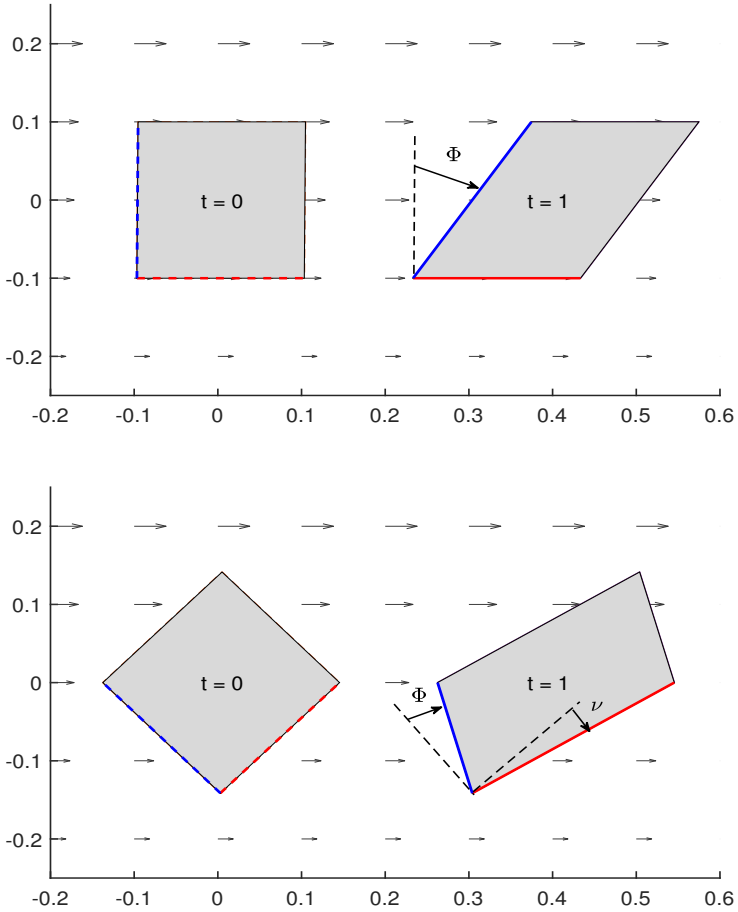

Figure 10: **(upper)** A square patch of a passive tracer was released into a homogeneous shear flow, Eq. (25), and advected for an elapsed time = 1. Advection caused this tracer patch to be translated to the right, rotated clockwise through about 20 deg, and deformed. **(lower)** The same velocity field, but here the initial tracer patch was rotated 45 deg. The rigthward translation and the rotation (suitably defined) apear to be the same as before, but the deformation was quite different.

where $\delta\mathbf{x}$ is a small displacement away from (x_0, y_0) and

$$\mathbb{G} = \begin{pmatrix} \dfrac{\partial u}{\partial x} & \dfrac{\partial u}{\partial y} \\ \\ \dfrac{\partial v}{\partial x} & \dfrac{\partial v}{\partial y} \end{pmatrix}$$

is the velocity gradient tensor (Sec. 2.5.2) evaluated at (x_0, y_0). The velocity gradient tensor evaluated at any point in the homegeneous shear flow (25) is just

$$\mathbb{G} = \begin{pmatrix} 0 & \beta \\ 0 & 0 \end{pmatrix} = \begin{pmatrix} 0 & 0.7 \\ 0 & 0 \end{pmatrix}. \tag{27}$$

There is no simple, single figure that suffices to illustrate even a 2x2 tensor, but it is possible to show what a tensor *does* when it multiplies a vector. A general account is that tensor multiplication on a vector makes a linear transformation of the vector. And thus, multiplication of a velocity gradient tensor on to a displacement vector yields a velocity (difference) vector that will in general have a magnitude, physical

dimensions and direction that are all different than that of the displacement vector. To see this, multiply $\mathbb{G}$ onto a set of unit (displacement) vectors, **e**, that span 360 deg, and plot the resulting velocity difference, $\delta\mathbf{V} = \mathbb{G}\mathbf{e}$, at the end of each unit vector, Fig. (11), upper left. For example, $\mathbb{G}$ times a unit displacement to the 'north' (positive y) produces a velocity difference to the 'east', $\mathbb{G}$ times a unit vector to the 'east' gives zero. The velocity differences plotted in this way happen to look a lot like the velocity field itself, since the shear is spatially uniform (homogeneous). However, this diagram applies at the specific point (x_o, y_o) where $\mathbb{G}$ has been evaluated, and are not a map of the velocity field *per se*.

For short times, this velocity field advects the tracer patch as if it was the Lagrangian velocity, cf. the first approximation of a trajectory computed in Fig. (6). Ths shears of the velocity field thus have important consequences for the displacement, rotation and deformation of a tracer patch. [9]

3.2 Physical rotation rate and vorticity

This shear flow changes the orientation of the tracer patch. Consider the case of a tracer patch that is initially aligned with the coordinate axes, Fig. (10, upper, and denote the angle of the blue axis with respect to the vertical (dashed line) by ϕ. By simple geometry (developed in Problem 1) below),

$$\frac{d\phi}{dt} = -\frac{\partial u}{\partial y}$$

for short times. Similarly, denote the angle between the red axis (orthogonal to the blue axis and thus initially horizontal) and the horizontal by υ, and a short calculation shows that

$$\frac{d\upsilon}{dt} = \frac{\partial v}{\partial x}.$$

In this specific example, the angle $\upsilon = 0$ initially, and stays that way since $\partial v/\partial x = 0$. The same sort of analysis can be done with a different set axes rotated at $\pi/4$ (Fig. 10, lower). It is evident that ϕ and ν change in the same sense (rotated clockwise) and in this specific case these angles change at about the same rate, which is about half (by inspection) of the previous $d\phi/dt$ computed on the blue axis in the case above. Clearly, the rate of change of the orientation (direction) of the sides of the tracer patch depends upon their orientation.

A plausible measure of the rotation rate of the patch as a whole is the average of the angular rates computed on orthogonal axes,

$$\omega = \frac{1}{2}(\frac{d\upsilon}{dt} + \frac{d\phi}{dt}) = \frac{1}{2}(\frac{\partial v}{\partial x} - \frac{\partial u}{\partial y}). \tag{28}$$

For this specific shear flow, $\omega = \partial u/\partial y = \alpha = -0.7$. This ω is called the physical rotation rate in the

[9] As you look at Fig. (11) and consider that it derived from the very simple shear flow of Eq. (25), you are probably wondering how this could possibly be progress — something very simple has been turned into a small blizzard of velocity diagrams that, you are cautioned, really aren't velocity maps at all. True enough, but hang on a little longer; once you have become familiar with these tensors and the Cauchy-Stokes Theorem, you will have the means to calculate useful, intelligible results for any velocity field.

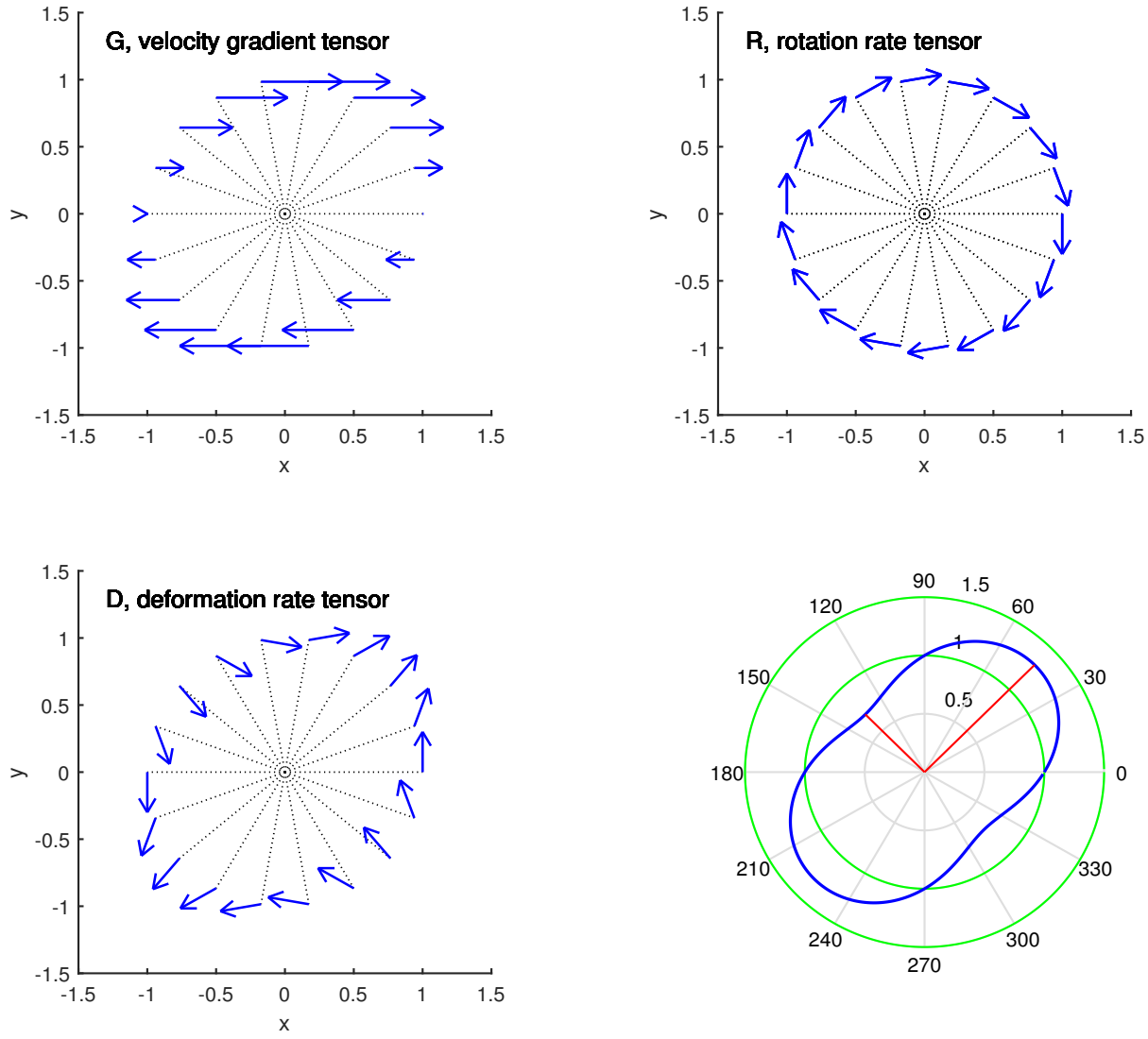

Figure 11: **(upper left)** The velocity gradient tensor $\mathbb{G}$ of the homogeneous shear flow, Eq. (27), has been multiplied into a sequence of unit vectors with varying directions (the dotted lines) and the resulting velocity plotted at the end of the unit vectors. This gives the impression of a map, but all of this should be envisioned to hold at a single point. **(upper right)** The rotation rate tensor $\mathbb{R}$ has been multiplied into a sequence of unit vectors. **(lower left)** The deformation rate tensor $\mathbb{D}$ multiplied into the unit vectors. Note that $\mathbb{G} = \mathbb{R} + \mathbb{D}$. **(lower right)** The blue, peanut-shaped ellipse is the linear deformation rate plus 1. The eigenvectors of the deformation rate tensor $\mathbb{E}$ are the red lines. Notice that the maximum and minimum values of the linear deformation rate are aligned with the eigenvectors.

sense that a neutrally buoyant paddle wheel embedded in this flow should rotate at this rate.[10] By inspection this appears to be a good estimate also for the case where the initial tracer patch was rotated, but a more convincing demonstration of the general applicability of (28) will come from the rotation tensor defined just below.

Despite that ω is the rotation rate of a physical object, ω is very seldom used in the practical analyses of fluid motion (solid mechanics is different in this regard). It is generally more useful to characterize the rotation of a fluid by a closely related measure called vorticity, χ, and which is $\chi = 2\omega$,

$$\text{vorticity in } \mathrm{R}^2\text{:} \qquad \boxed{\chi = \frac{\partial v}{\partial x} - \frac{\partial u}{\partial y} = \nabla \times \mathbf{V}} \tag{29}$$

The vorticity and the vorticity balance equation, which is the curl of the momentum balance, are ubiquitous. For that reason it makes sense to leave the factor 2 with ω rather than χ. The factor 2 will not come up again until Sec. 6, when the vorticity of wind or ocean currents is added to 2 times the physical rotation rate of the Earth to form the absolute vorticity observed from an inertial reference frame.

In two-dimensions, the vorticity is effectively a scalar, i.e, a single number. In R^3 the vorticity $\nabla \times \mathbf{V}$ is a vector with three components. Vorticity is invariant to the orientation of the tracer patch with respect to the coordinate system. The vorticity of a fluid is analogous in many respects to the angular momentum of a rotating solid. It differs in being defined point-wise, and has no moment arm or center. The appeal and utility of vorticity comes from its somewhat simpler conservation law compared with that of momentum (Sec. 3.4, Part 1), and partly for that reason the vorticity balance can often be used to real advantage in the diagnosis (and prediction) of fluid flows (an example is in Sec. 6).

3.3 Deformation rate

In the common case that the angles ϕ and ν change at different rates, then the tracer patch will necessarily change shape or deform. One possible measure of the shape of a parcel is the interior angle between, say the upper and right limbs of the orthogonal axes, Γ, and evidently $\Gamma = \pi/2 + \phi - \upsilon$, Fig. (10). If it happens that ϕ and υ change by the same amount, then Γ =constant, and the parcel will simply rotate without deforming, i.e., a solid body rotation. But if the angles change at a different rate, as they do in Fig. (10), upper, then the shape of the parcel will necessarily change, and

$$\frac{d\Gamma}{dt} = \frac{d\upsilon}{dt} - \frac{d\phi}{dt} = \frac{\partial v}{\partial x} + \frac{\partial u}{\partial y}. \tag{30}$$

If the angle ϕ changes while the lengths of the parcel sides remain constant, then this kind of time-varying deformation is called a *shear* deformation or strain rate. This is the case in Fig. (10), upper, when the angle ϕ is small. This particular shear deformation rate is in the plane parallel to the x-axis.

But suppose that the same square tracer patch is rotated by 45 degrees before being released into the

[10] An especially good illustration of this is found in the Shapiro fluid mechanics video 'Vorticity', https://video.odl.mit.edu/videos/2e75fb6283de4b54a09ee0da1c8e78e9/

flow. The effect of advection then appears to be quite different (Fig. 10, lower); the sides of the parcel remain (almost) orthogonal, but now the lengths of the sides are compressed or stretched (lower right side. A deformation rate that causes a change in the length of a material line is termed a *linear* deformation rate.

Unlike the vorticity, the deformation rate can not be written as a vector operator on the velocity, and from Fig.(10) it seems that when the deformation rate that is diagnosed with a given orthogonal axes pair (the sides of the parcel), the result is entirely dependent upon the orientation of these axes with respect to the flow. This is a hint that there is more to say about the deformation rate than the special case Eq. (30) can inform.

3.4 Rotation rate and deformation rate tensors

The deformation rate may change the shape and the size (area) of a parcel, while rotation alone can not. This suggests that it may be useful to separate the rotational part of the velocity gradient tensor from all the rest. This is straightforward because the rotation is associated with the anti-symmetric part of the velocity gradient tensor, and any (N x N) tensor can be factored into symmetric and anti-symmetric component tensors in the following steps. Let $\mathbb{G}'$ be the transpose of $\mathbb{G}$,

$$\mathbb{G}' = \begin{pmatrix} \frac{\partial u}{\partial x} & \frac{\partial v}{\partial x} \\ \\ \frac{\partial u}{\partial y} & \frac{\partial v}{\partial y} \end{pmatrix}$$

and now subtract and add $\mathbb{G}'$ to $\mathbb{G}$ as

$$\begin{aligned} \mathbb{G} &= \frac{1}{2}(\mathbb{G}-\mathbb{G}') + \frac{1}{2}(\mathbb{G}+\mathbb{G}') \\ &= \mathbb{R} + \mathbb{D}. \end{aligned} \tag{31}$$

The effect is to decompose $\mathbb{G}$ into two new tensors

$$\mathbb{R} = \frac{1}{2}\begin{pmatrix} 0 & -(\frac{\partial v}{\partial x}-\frac{\partial u}{\partial y}) \\ \\ \frac{\partial v}{\partial x}-\frac{\partial u}{\partial y} & 0 \end{pmatrix} \tag{32}$$

and

$$\mathbb{D} = \begin{pmatrix} \frac{\partial u}{\partial x} & \frac{1}{2}(\frac{\partial u}{\partial y}+\frac{\partial v}{\partial x}) \\ \\ \frac{1}{2}(\frac{\partial u}{\partial y}+\frac{\partial v}{\partial x}) & \frac{\partial v}{\partial y} \end{pmatrix} \tag{33}$$

$\mathbb{R}$ is the **rotation rate tensor** and by its construction is anti-symmetric, $R_{12} = -R_{21}$, and $R_{11} = R_{22} = 0$. In R^2, $\mathbb{R}$ has only one unique component that is equal to the physical rotation rate, in this case ω, Eq. (28). When $\mathbb{R}$ is multiplied onto a set of unit vectors the result is a velocity difference $\delta\mathbf{V} = \mathbb{R}\mathbf{e}$ that is normal to the unit vector and has the same amplitude (same speed) for all directions of the unit vector. The rotation associated with $\mathbb{R}\,\mathbf{e}$ is readily apparent, Fig. (11, upper right) and Fig. (10), upper row, and for the simple shear flow of Eq. (27), the physical rotation rate is just $\omega = -\frac{1}{2}\partial u/\partial y = -0.35$, and thus 0.35 radians $\approx$ 20 degrees over a time interval = 1 (Fig. 10, upper row). The vorticity of this shear flow is then 2ω = -0.7. The vorticity is a physical property of the flow, and hence its value should be (and is) independent of the arbitrary choice of a coordinate system, whether cartesion and rotated (Fig. 10 upper row, left and right) or cylindrical, or any other.

$\mathbb{D}$ is the **deformation rate tensor,** and is symmetric, $D_{12} = D_{21}$. In general, the diagonal elements are non-zero and are not equal. Thus the deformation rate tensor $\mathbb{D}$ in R^2 has three independent components (in general). The resulting velocity difference, $\delta\mathbf{V} = \mathbb{D}\ \mathbf{e}$, where $\mathbf{e}$ is the unit vector, varies in direction and amplitude depending upon the direction of $\mathbf{e}$ the (in the specific case shown in Fig. (11d) the amplitude happens to be constant). The linear deformation rate in a given direction is given by the component of $\delta\mathbf{V}$ that is parallel (or anti-parallel) to the unit vector in that specific direction. There are two special directions in which the linear deformation rate is either a minimum or a maximum. Given the specific $\mathbb{G}$ of Eq. (27), the minimum linear deformation rate is -0.35 and is found when the unit vector makes an angle of 135 (or 315) degrees with respect to the x axis (Fig. 11b); the maximum linear deformation rate is 0.35 and is at 45 (or 225) degrees. Thus a parcel will be compressed along a line that is oriented 135 (or 315) degrees (with respect to the x axis) and will be stretched along a line normal to this, 45 (or 225) degrees. Notice too that when the unit vector is pointing in these special directions, the velocity difference and the unit vector are either anti-parallel or parallel, and the relationship among $\mathbb{D}, \mathbf{e}$, and $\delta\mathbf{V}$ may then be written

$$\mathbb{D}\,\mathbf{e} = \delta\mathbf{V} = \lambda\,\mathbf{e},$$

where λ is a real number. These special directions are thus the directions of the *eigenvectors* of the symmetric tensor $\mathbb{D}$, and the amplitude of the linear deformation rate in those directions is given by the corresponding *eigenvalues*, λ = -0.35 and +0.35 for this particular $\mathbb{D}$.[11]

The deformation rate is proportional to the rate at which adjacent fluid parcels slide past one another, which, in the presence of viscosity, leads to a viscous stress. Since the solid body-rotational part of the velocity gradient tensor does not contribute to linear or shear deformation, it may as well be subtracted from the velocity gradient tensor before computing the viscous stress (Sec. 3, Part 1). Thus the viscous stress tensor is often written $\mathbb{T} = \nu\mathbb{D}$, which insures that the stress tensor will be symmetric.

Divergence. Another important quantity that was encountered in Part 1, Sec. 3.5, is the divergence, the sum of the linear deformation rates measured in any two orthogonal directions. Let L_x be an

[11] Eigenvectors and eigenvalues are a central theme of linear algebra and will not be reviewed here. Excellent references are by J. Pettofrezzo *Matrices and Transformations* (Dover Pub., New York, 1966) and for undergraduate-level applied mathematics generally, M. L. Boas, *Mathematical Methods in the Physical Sciences, 2nd edition* (John Wiley and Sons, 1983). If you have access to Matlab, https://www.mathworks.com/academia/courseware/matrix-methods.html is a very useful tutorial, including eigenvectors and values.

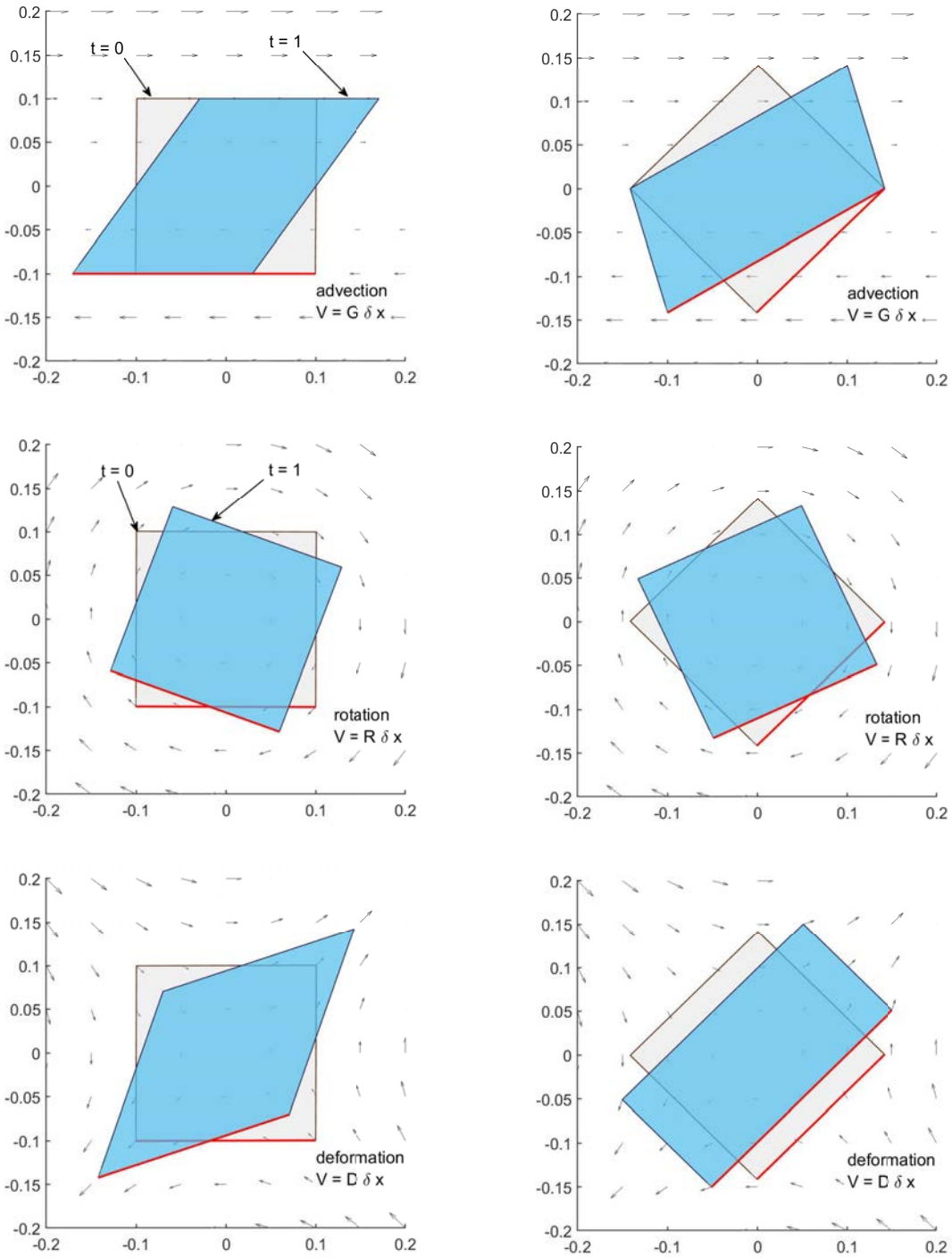

Figure 12: A square patch of passive tracer was released into a prescribed velocity field and advected for an elapsed time = 1. The initial patch is light gray; after advection the patch is blue. The tracer patch in the right column was first rotated 45 deg. **(upper row)** The velocity was computed from the velocity gradient tensor, $\mathbf{V} = \mathbb{G}\boldsymbol{\delta}\mathbf{x}$, Eq. (25), with no mean flow. This is otherwise a repeat of Fig. (10). **(middle row)** This velocity was computed from the rotation tensor, $\mathbf{V} = \mathbb{R}\boldsymbol{\delta}\mathbf{x}$, with no mean flow and no deformation. These tracer patches both rotate clockwise without deformation. The amount of rotation is independent of the orientation of the patch. **(lower row)** This velocity field was $\mathbf{V} = \mathbb{D}\boldsymbol{\delta}\mathbf{x}$. The tracer patch at left illustrates shear deformation, while the tracer patch at right was elongated and compressed in orthogonal directions, illustrating linear deformation. The effect of a deformation velocity field depends upon the orientation of the tracer patch with respect to the eigenvectors of the deformation tensor. In all six cases the area of the patch was conserved, indicating zero divergence.

(infinitesimal) line segment parallel to the x-direction, then

$$\frac{dL_x}{dt} = L_x \frac{\partial u}{\partial x}, \tag{34}$$

and similarly for L_y. Thus if a tracer patch has an area $A = L_x L_y$, then the normalized rate of change of the area is just

$$\text{divergence in 2-d:} \quad \boxed{\frac{1}{A}\frac{d}{dt}A = \frac{\partial u}{\partial x} + \frac{\partial v}{\partial y} = \nabla \cdot V}$$

The divergence is the sum of the eigenvalues of the deformation tensor, and also the trace of $\mathbb{D}$, $\mathbb{D}_{11} + \mathbb{D}_{22}$. In the specific case of the shear flow Eq.(25), the divergence happens to be zero, though the linear deformation rate in most directions is not zero. The divergence is a scalar, and is the same for any orientation of the parcel or of the coordinate axes. Thus, like the 2-d vorticity, the divergence is invariant to coordinate rotation.

3.5 The Cauchy-Stokes Decomposition Theorem brings this all together

The discussion above is summarized by the Cauchy-Stokes Theorem — the fluid motion at a given place and time may be resolved into three components:

Translation — advection by the spatial mean velocity $\mathbf{V}_o$.

Rotation — induced by advection in a sheared velocity field. The physical rotation rate is 1/2 $\nabla \times \mathbf{V}$ and is the off- diagonal elements of the rotation rate tensor, $\mathbb{R}$. The rotation rate is invariant to coordinate rotation.

Deformation — a change in shape and area (in 2-d) of a material volume caused by advection in a sheared velocity. The maximum and minimum linear deformation rate are given by the eigenvectors and eigenvalues of the deformation rate tensor, $\mathbb{D}$. The sum of the eigenvalues is the divergence, $\nabla \cdot \mathbf{V}$, which gives the rate of change of area. Divergence is an invariant to coordinate rotation.

3.6 Application to the vortex flows

Solid body rotation. Let's now try this formalism on the vortex flows of Fig. (9). A good case could be made for doing these calculations in polar coordinates, but for now the more familiar rectangular coordinate representation of the solid body rotation is

$$u = \Omega\, y, \quad \text{and} \quad v = -\Omega\, x,$$

where the rotation rate Ω is a constant. The appropriate tensors are

$$\mathbb{G} = \begin{pmatrix} 0 & \Omega \\ -\Omega & 0 \end{pmatrix} \qquad \mathbb{R} = \begin{pmatrix} 0 & \Omega \\ -\Omega & 0 \end{pmatrix} \qquad \mathbb{E} = \begin{pmatrix} 0 & 0 \\ 0 & 0 \end{pmatrix}$$

Note that these $\mathbb{G}$, $\mathbb{R}$, $\mathbb{E}$ happen to hold throughout the vortex, which is unusual. Given all of the zeros, this case looks to be somewhat degenerate, however, the formalism works as intended; $\mathbb{R}$ indicates (physical) rotation at the rate Ω everywhere in the vortex, and $\mathbb{D}$ indicates zero deformation, and of course zero divergence throughout the vortex. Thus, advection by a solid body rotation does not change the area or the shape of a tracer patch in any way (which we knew already from Fig. 9), though it does cause a rotation.

Irrotational vortex. Now consider an irrotational vortex, which makes better use of this formalism. In cartesian coordinates,

$$u = \Omega\, r_o^2\, \frac{y}{r^2} \quad \text{and} \quad v = -\Omega\, r_o^2\, \frac{x}{r^2},$$

where $r^2 = x^2 + y^2$, r_o is a constant, and Ω is as before. The difference between this vortex and the solid body rotation is the $1/r^2$ dependence of the azimuthal speed. By choosing $r_o = 1$, and the Ω used above, the azimuthal speed, $u_\theta = \Omega r$, is equal to that of the solid body rotation at $r = 1$, but not otherwise. The velocity gradient tensor of this flow is

$$\mathbb{G} = \frac{\Omega r_o^2}{r^4} \begin{pmatrix} -2xy & x^2 - y^2 \\ x^2 - y^2 & 2xy \end{pmatrix}$$

The rotation rate tensor vanishes throughout,

$$\mathbb{R} = \frac{\Omega r_o^2}{r^4} \begin{pmatrix} 0 & 0 \\ 0 & 0 \end{pmatrix}$$

and so the deformation rate tensor is just

$$\mathbb{E} = \mathbb{G}.$$

The two eigenvectors of this tensor are

$$\frac{\Omega r_o^2}{r^4} \begin{pmatrix} f(x,y) \\ 1 \end{pmatrix} \quad \text{and} \quad \frac{\Omega r_o^2}{r^4} \begin{pmatrix} -f(x,y) \\ 1 \end{pmatrix}$$

where

$$f(x,y) = \frac{\sqrt{4x^2y^2 + (x^2 - y^2)^2}}{x^2 - y^2} - \frac{2xy}{x^2 - y^2}$$

and the two corresponding eigenvalues are

$$\sqrt{4x^2y^2 + (x^2 - y^2)^2} \quad \text{and} \quad -\sqrt{4x^2y^2 + (x^2 - y^2)^2}.$$

At the initial position of the tracer patch, $(x,y) = (0,1)$,

$$\mathbb{E} = \frac{\Omega r_o^2}{r^4}\begin{pmatrix} 0 & -1 \\ -1 & 0 \end{pmatrix} \qquad \mathbb{D}_{vector} = \frac{1}{\sqrt{2}}\begin{pmatrix} -1 & -1 \\ -1 & 1 \end{pmatrix} \qquad \mathbb{D}_{value} = \frac{\Omega r_o^2}{r^4}\begin{pmatrix} -1 & 1 \end{pmatrix}$$

where the eigenvectors are the column vectors of $\mathbb{D}_{vector}$ and the eigenvalues are the first and second elements of $\mathbb{D}_{value}$. The first eigenvalue is negative, and hence the tracer patch will be compressed in the direction of the first eigenvector, 225 and 45 degrees anticlockwise from positive x. The second eigenvalue is positive, and hence the tracer patch will be stretched along the directio of the second eigenvector, 135 and 315 degrees. The eigenvectors and values will vary in space; after the tracer patch had been advected clockwise, and centered on $(x,y) = (1,0)$, the values at that site are

$$\mathbb{E} = \frac{\Omega r_o^2}{r^4}\begin{pmatrix} 0 & 1 \\ 1 & 0 \end{pmatrix} \qquad \mathbb{D}_{vector} = \frac{1}{\sqrt{2}}\begin{pmatrix} -1 & 1 \\ 1 & 1 \end{pmatrix} \qquad \mathbb{D}_{value} = \frac{\Omega r_o^2}{r^4}\begin{pmatrix} -1 & 1 \end{pmatrix}$$

The eigenvalues are unchanged, but the eigenvectors are rotated clockwise through 90 degrees, and hence the deformation relative to the tracer patch continued. The normalized rate of stretching is

$$\frac{1}{L}\frac{dL}{dt} = \frac{\Omega r_o^2}{r^4} = 1,$$

and persists as the tracer patch is advected clockwise by the vortical flow. By the time $t = \frac{3}{2}\pi$, the patch had been stretched by a factor $\frac{3}{2}\pi$, and compressed by the reciprocal. The initially square tracer patch was thus drawn into a long, thin filament, all the while conserving its area and thus the net content of the tracer. This kind of filamentation process is a common property of most real flows, and is often called 'stirring', especially when it is generated deliberately to enhance mixing (more on this in the next section).

3.7 Key ideas

1) A fluid flow having some spatial variability (which is to say all real flows) may cause a tracer patch to rotate, change shape (deform) and possibly change volume. Along with the transport, these are often crucial effects of advection.

2) The instantaneous rotation and deformation of a tracer patch (Lagrangian properties) may be related to the velocity gradient tensor defined on the Eulerian velocity field via the Cauchy-Stokes Theorem.

3) Physical rotation rate is the average at which orthogonal axes rotate. Vorticity is defined to be twice the physical rotation rate and has properties analogous to angular momentum, though defined point-wise in a fluid.

4) Deformation rate may be characterizd as the strectching (or compression) of fluid lines along orthogonal directions. The eigenvectors of the deformation tensor indicate the directions in which the linear deformation is the maximum and minimum. The values are gien by the eigenvalues.

5) The trace of the deformation tensor is an invariant called the divergence, which is the rate of change of the normalized area (in R^2).

6) The estimation of finite amplitude rotation or deformation requires an integration in time of the advection equation, that, in effect, continually updates the rotation and deformation tensors.

3.8 Problems

1) Go back and take another look at the (stirred) fluid flow in a teacup. Do you see evidence of divergence, rotation or deformation?

2) Refer to Fig. (10), upper. Let the initial vertical side of the tracer patch be h, and let the relative displacement of the upper left corner be d. Show that the included angle ϕ changes with time as $d\phi/dt = (1/h)\partial d/\partial t = \partial u/\partial y$ provided that ϕ is small, in effect, at short times. How does this estimate at long times? In a similar vein, what is the short and long time dependence of the hypotenuse, $\sqrt{h^2+d^2}$?

3) It was noted that the average rotation rate of a tracer patch defined by Eqs. (28) or (29) is independent of the orientation of the axes with respect to the tracer patch. Can you verify this by inspection of Fig. (10), or by Fig. (12), middle?

4) Refer to Fig. (12), lower right. Compare (quantitatively) the linear deformation rate in the directions 45 degrees and 135 degrees with the observed change of the tracer patch length and width in Fig. (12), lower right. Compare also with the distance between opposite vertices of the square (and then parallelogram) of Fig. (12), lower left.

5) The decomposition of the velocity gradient tensor as $\mathbb{G} = \mathbb{R} + \mathbb{D}$ is linear, as is the operation of tensor multiplication. Can you verify from Fig. (12) (by inspection at several points) that that the sum of the rotation velocity field and the deformation velocity field (middle and lower rows) does indeed add up to the 'advection' velocity of the upper row? Specifcally, what happens to the y-component fo the velocity?

6) A good example of a simple flow in which to examine stirring and mixing is a confluent flow, $u(x,y) = b*x$ and $v(x,y) = -b*y$. What are the rotation and deformation tensors for this flow? Suppose the start is a square tracer patch offset from the $x-$axis. What is the long-time tracer distribution? An animation of this case (including some random particle motion that is discussed in Sec. 4) is available from https://www2.whoi.edu/staff/jprice/wp-content/uploads/sites/199/2022/08/confluence.mp4

4 Advection by resolved and unresolved motions

Every real fluid flow will be made up of motions that have a more or less extensive range of time and space scales. In the case of flow in a tea cup, the largest scale of motion will usually be a vortex that will fill the entire domain and then slowly decay (tens of seconds) due to viscous drag with the bottom and sides of the cup. Small scale motions, including irrotational vortices generated by the initial stirring, will be present at the beginning of an experiment, and viscous boundary layers a few millimeters thick will show the direct effect of boundary friction. The range of spatial scales in a teacup is quite limited, only about one order of magnitude, because viscosity sets the lower bound to be not much less than the domain size. The scales of motion of the atmosphere span at least eight orders of magnitude, from thousands of kilometers in the westerly wind belts, down to centimeters in viscous boundary layers that are in contact with a smooth surface and the equivalent of viscous boundary layers in the tea cup. It is quite possible to model explicitly (numerically) the entire range of motion in a tea cup,[12] but it is certainly not possible to do so for the atmosphere.

The first step in every practical analysis will be to decide what range of the scales of motion will be resolved, either by observations or modelled explicitly, and an acknowledgment of the scales that will have to be left unresolved, whether for practical or conceptual reasons. If the spatial or temporal scales of the unresolved motions are larger than the scales of interest, then the issue may be as simple as observing or defining the average velocity, the $\mathbf{V_o}$ of the Cauchy Stokes Theorem. But very often the unresolved scales will include smaller space scales and faster time scales. In that case the scale separation is often written as

$$\mathbf{v} \;=\; \mathbf{V} \;+\; \mathbf{v}', \tag{35}$$

where $\mathbf{v}$ is the total, or actual velocity, and $\mathbf{V}$ is the resolved velocity estimated by a linear averaging applied to $\mathbf{v}$ over some suitable space or time scale, say a time T,

$$\mathbf{V}(\mathbf{x},\mathbf{t}) \;=\; \overline{\mathbf{v}} \;=\; \frac{1}{T}\int_t^{t+T} \mathbf{v}(\mathbf{x},\mathbf{t})dt. \tag{36}$$

The unresolved velocity, $\mathbf{v}' = \mathbf{v} - \mathbf{V}$, is often termed the 'eddy' velocity, though without implying a closed circulation. The average of the eddy velocity

$$\overline{\mathbf{v}'} \;=\; \frac{1}{T}\int_t^{t+T} \mathbf{v}'dt \;=\; 0.$$

The significance of (35) lies in the kind and the extent of the averaging that is applied to the total velocity to define the resolved velocity. Temporal averaging is most common (36), but spatial averaging and ensemble averaging are possible and quite useful as well.[13] There is no inconsistency in allowing that the resolved velocity $\mathbf{V}$ can be varying in time. But, for this averaging to be most useful, there should

[12] Ok, but why would you? See Luo G, Hou TY. 2014, Potentially singular solutions of the 3D axisymmetric Euler equations. Proc. Natl Acad. Sci. USA 111, 12 96812 973. (doi:10.1073/pnas.1405238111), and https://www.bbc.com/news/av/uk-england-london-54195597

[13] For more on Reynolds averaging, see https://www2.whoi.edu/staff/jprice/wp-content/uploads/sites/199/2023/11/Randall-RA.pdf

be a time scale T over which $\mathbf{V}$ varies only a little, and yet is long enough that averages of the eddy velocity and its moments (example below) will be reasonably well-converged to meaningful averages. For this to hold rigorously, there will have to be a separation of time scales between the resolved and the eddy velocities, sometimes referred to as a spectral gap, though in practice there is likely to be a continuum of time (or space) scales.

4.1 Reynolds averaging of advection terms leads to eddy fluxes

Having defined the resolved velocity, the issue then turns to accounting for the effects of the smaller/faster scale eddy motions, even though not observing or modelling the eddy motion in detail. This problem — accounting for the effects of unresolved motions — is a significant part of the research effort in fluid dynamics; Reynolds averaging gives us a place to start.

Presume an advection/diffusion equation for a scalar variable, c, having no special properties, i.e., a passive tracer,

$$\frac{\partial c}{\partial t} \;=\; -\nabla\cdot(\mathbf{v}c) + K_c\nabla^2 c, \tag{37}$$

with K_c the molecular diffusivity of c. As noted above, it is almost always necessary to distinguish resolved from unresolved motions as in (36), and the same holds for tracer distribution, and so let

$$c \;=\; C \;+\; c'.$$

Substitute these into the advection equation (37) and average again to find the governing equation for the resolved tracer field, C,

$$\frac{\partial C}{\partial t} \;=\; -\nabla\cdot(\mathbf{V}C) \;-\; \nabla\cdot\overline{(\mathbf{v}'c')} \;+\; K_c\nabla^2 C. \tag{38}$$

Rather than the four advection terms that might have been expected, there are only two advection terms since the cross-products of resolved and unresolved variables vanish under the presumed linear averaging operation, e.g.,

$$\overline{\nabla\cdot(\mathbf{V}c')} \;=\; \nabla\cdot\overline{\mathbf{V}c'} \;=\; \nabla\cdot\mathbf{V}\,\overline{c'} \;=0.$$

The key finding from this Reynolds averaging procedure is that the net effect of the eddy motion acting upon the resolved-scale tracer distribution is the cross-correlation, $\overline{\mathbf{v}'c'}$, that appears in (38). This term is variously called an eddy flux or an eddy-covariance. Reynolds averaging alone doesn't tell us anything regards the physical process that makes up the eddy flux.

As an example of an eddy flux, consider the vertical flux of water vapor (evapotranspiration), F $[mass\ length^{-2}\ time^{-1}]$, at a height of a few tens of meters in the atmospheric boundary layer above a horizontally homogeneous, open field. The total vertical flux will be, in general,

$$F \;=\; \rho_{air}(WQ \;+\; \overline{w'q'} \;-\; K_q\frac{\partial q}{\partial z}). \tag{39}$$

The species being transported is q, the water vapor mixing ratio (closely proportional to humidity). The first term on the right is transport by the mean vertical velocity, W, which may be assumed negligible if

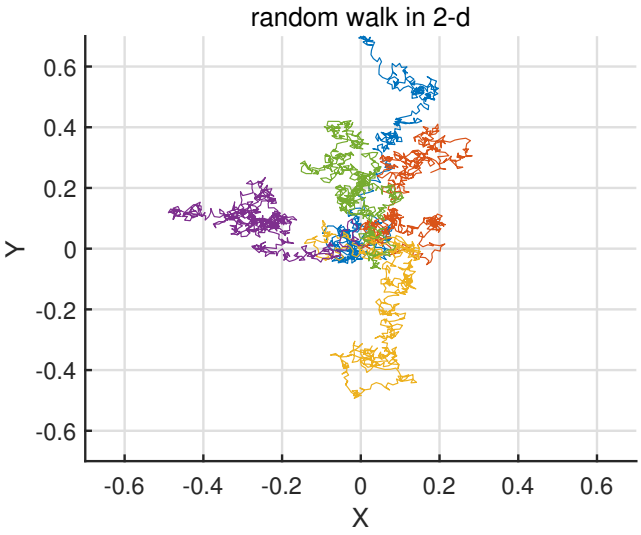

Figure 13: Five particle trajectories from the random walk, Eq. (40), up to time $t = 2\pi$. In each trajectory there are 628 steps of distance $s = 0.01$, which give an appearance much like Brownian motion. The next five trajectories will have similar overall amplitude, but likely to be completely different in detail.

there are no significant horizontal variations of topography. The third term represents the flux of water vapor due to molecular diffusion, and is completely negligible if the boundary layer is well-mixed and turbulent, which is nearly always the case. The second term on right is the vertical eddy flux, with w' the vertical component of the eddy (wind) velocity, and q' the comparable eddy component of the water vapor mixing ratio. From observations we know that this eddy flux is almost always the dominant process of water vapor vertical transport within the atmospheric boundary layer. To estimate an observed eddy flux requires rather precise measurements of w and q, since q' is typically O(10^{-2}) Q, and at a temporal resolution of O(0.1 sec). A stable average of this eddy flux requires about ten minutes of high frequency sampling.[14]

4.2 A random walk as a first model of unresolved advection

The discussion above is fairly abstract, and so it will be helpful to consider a concrete example in which the resolved velocity is a vortex of the kind considered in Sec. 3, and eddy velocity will be associated with a random walk of discrete particles. The statistics of the random walk are presumed to be known, but not its detailed motion. In the upcoming Sec. 4.4 these two 'flows' will be added together to make a flow with two distinct scales, and thus advection by resolved and unresolved motions at once. But for now, consider just the eddy velocity $\mathbf{v}'$ and the resulting eddy flux.

In place of the continuous, passive tracer c noted above, the flow will be observed by computing the trajectories of discrete, freely drifting material particles executing a random walk. The calculation is as follows: particles were launched at $t = 0$ at the origin, $(x, y) = (0, 0)$. At each time, $t_i = i\delta t$, the position of the jth particle was advanced through a small, random vector displacement

$$ {}^{j}\mathbf{x}'_{i+1} \;=\; {}^{j}\mathbf{x}'_{i} \;+\; {}^{j}\delta\mathbf{x}_{i}, $$

[14] Measuring and interpreting eddy fluxes is an object in meteorology and many other fields. An excellent primer on the topic of eddy flux measurement in the atmosphere's land boundry layer is by https://www.licor.com/env/support/Eddy-Covariance/videos/ec-method-02.html

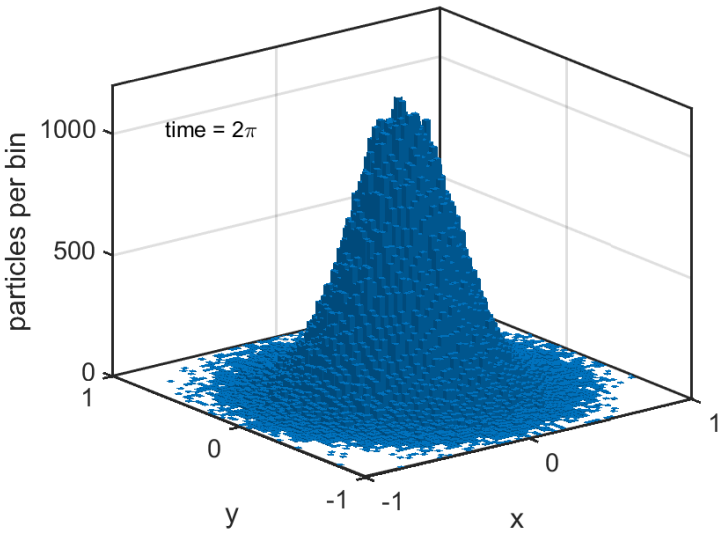

Figure 14: A histogram of the particle count per (arbitrary) bin width, from an ensemble of 500,000 random walk trajectories like those of Fig. (25). This data is from time $t = 2\pi$. At later times, the distribution spreads laterally as $\sqrt{t}$ and the peak amplitude decreases as $1/t$.

where

$$ {}^{j}\delta\mathbf{x}_i \;=\; \begin{pmatrix} {}^{j}\delta x_i \\ {}^{j}\delta y_i \end{pmatrix} \;=\; \frac{s}{\sqrt{2}} \begin{pmatrix} \cos({}^{j}\mu_i) \\ \sin({}^{j}\mu_i) \end{pmatrix}, \tag{40} $$

and s is a small, fixed step size that we are free to choose, $s = 0.01$. There is no need to assign units at this point, but the dimensions will be kept consistent and noted on occasion. Random comes from the angle μ, which is uniformly distributed on the interval $0 \le \mu < 2\pi$. Each realization of δx is unique; there is no memory from one step to the next, and so there is zero lagged correlation in time for a given particle. There is zero cross-correlation between any two particles on ensemble average. The time step is taken to be $\delta t = 0.01$ and hence the speed of the random walk is $|\mathbf{w}| = s/\delta t = 1.0$. The experiments were run for a duration, T, up to 10π and thus there will be $n = T/\delta t = 3141$ steps in each trajectory during a full experiment. Five typical trajectories are shown in Fig. (25). The number of particles in the ensemble, N, is almost unconstrained by the minimal computational demand of the random walk calculation. N may be chosen to give either legible graphics when every particle is shown, N = 10,000, or much larger, up to 500,000, to give well-converged ensemble averages denoted by angle brackets,

$$ < \tilde{y} > \;=\; \frac{1}{N} \sum_{j=1}^{N} {}^{j}\tilde{y}. $$

Such a large N is excessive for many purposes. Notice that the ensemble averaging is over discrete, not continuous variables. The identity of each particle is retained throughout an experiment, characteristic of Lagrangian method. Whether such a random walk is a faithful model of a turbulent flux of the sort referenced in Eq. (39) is a (very) good question that will be visited in Sec. 4.4.

The eddy motion prescribed via Eq. (40) is a classical random walk in two dimensions, and has well-known statistical properties.[15] First, while any one particle might end up anywhere within a radius

[15] A random walk is interesting and important in its own right as it can make a useful model of the stochastic processes that arise in a very wide range of contexts, from economics to astrophysics. The basics of random walk are described well in

wT of its launch position, the ensemble average of x' and y' will vanish for all times, e.g.,

$$< x'_n > \;=\; < \sum_{i=1}^{n} {}^j\delta x_i > \;=\; n\, s < \cos({}^j\mu_i) > \;=\; 0,$$

which is consistent with the intent that this is the eddy component of particle displacement. However, the ensemble average of the *squared* displacement in x or y, e.g.,

$$< x'^2_n > \;=\; < \sum_{k=1}^{n} {}^j\delta x_k \times \sum_{l=1}^{n} {}^j\delta x_l \; > \tag{41}$$

does not vanish, in general. The product of sums on the right may be written

$$< \sum_{k=1}^{n} {}^j\delta x_k \times \sum_{l=1}^{n} {}^j\delta x_l > \;=\; < \sum_{i=1}^{n} {}^j\delta x_i^2 > \;+\; < 2 \sum_{k>l}^{n} \sum_{l=1}^{n} {}^j\delta x_k \, {}^j\delta x_l > . \tag{42}$$

The second term at right is the product of the δxs at different times, $k > l$. This vanishes on ensemble average, since the angle μ at each step is independent of the μ at the previous (or any other) time step. Thus the ensemble average of the mean square of x' increases with the elapsed time, t, as

$$< x'^2_n > \;=\; < \sum_{i=1}^{n} {}^j\delta x_i^2 > \;=\; n\, s^2 < \cos\left({}^j\mu_i\right)^2 > \;=\; \frac{1}{2} n\, s^2 \;=\; \frac{1}{2} s\, |\mathbf{w}|\, t. \tag{43}$$

It is often preferable to consider the root mean square of x' or r', and these grow as the square root of the elapsed time, Fig. (15), left,

$$\boxed{\sqrt{< x'^2_n >} \;\propto\; \sqrt{n} \;\propto\; \sqrt{t}}$$

This square root time dependence of the rms displacement is perhaps the most characteristic and important property of a random walk.

4.3 An Eulerian description of dispersion by a random walk; effective diffusivity

The particle trajectories discussed above are Lagrangian, in that they record the motion of (simulated) material particles. This seems natural for the definition of a random walk and the description of an evolving tracer patch or particle cloud. However, to make contact with most theory and modelling, this Lagrangian description is best translated into its Eulerian equivalent.

When particle trajectories are available in large numbers, as they are here, the particle concentration (particles per unit area) is analogous to the continuous passive tracer, c. The two-dimensional, Reynolds averaged advection equation for this tracer is just, repeating (38),

$$\frac{\partial C}{\partial t} \;=\; -\,\mathbf{V}\cdot\nabla C - \nabla\cdot\overline{\mathbf{v}'c'} \;+\; K_c \nabla^2 C.$$

https://mathworld.wolfram.com/RandomWalk2-Dimensional.html

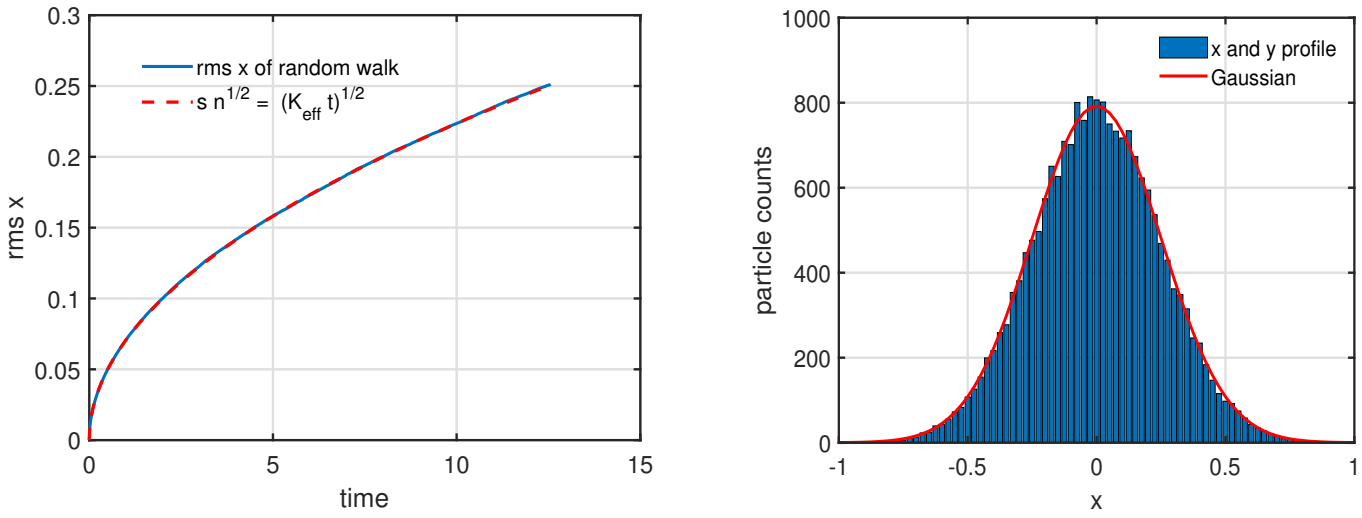

Figure 15: Statistical properties of the random walk, Eq. (40). **(left)** Root mean square x displacement as a function of time from an experiment that tracked a very large number of particles (blue line). The expected rms for this process is $\sigma = s\sqrt{n/2}$, where s is the step size and n the number of steps up to the time = $n\delta t$ (red dashed line, which is directly on top of the blue line). **(right)** Particle concentration at the time $t = 2\pi$ as a function of x or y made by cutting across the distribution of Fig. (26) along $y = 0$ and $x = 0$ and averaged (blue bars). The red line is the concentration from the solution (46) of the classical diffusion equation which uses the known σ of the random walk at left. This favorable comparison supports the use of classical diffusion concepts, e.g., effective diffusivity, to describe the dispersion of particles by a random walk.

To solve this for C requires knowing the resolved velocity, $\mathbf{V}$, here taken to be a prescribed vortex flow of the kind seen in Sec. 3, and the eddy flux, $\overline{\mathbf{v}'c'}$. Evaluating this latter term will require several assumptions, some bordering on guesses, that can be checked against known the random walk. The path taken here is to apply the classical mixing length theory to estimate an effective diffusivity, K_{eff}, of the random walk. The speed of the eddy velocity $\mathbf{v}'$ is estimated to be the speed of the random walk, w, which is homogeneous, isotropic and known,

$$|\mathbf{v}'| \approx w = \frac{s}{\delta t}.$$

The eddy anomaly of the tracer concentration, c', is less obvious, but as a guess, try

$$c' = s\,|\nabla C|,$$

which presumes that the step size, s, of the random walk is a mixing length acting on the resolved tracer field. There is no direction associated with the random walk step, and so this too is a relation for magnitude only. To here this gives

$$|\overline{\mathbf{v}'c'}| \approx w\,s|\nabla C|.$$

The right hand side has the form of a Fickian diffusion, $-K\,\nabla C$, provided that $K_{eff} \approx w\,s$ is an effective

diffusivity associated with the random walk. Eq. (43) indicates a factor 1/2 coming from the ensemble averaging of the random direction, μ, and so, provisionally,

$$K_{eff} \approx \frac{1}{2} s\, w. \tag{44}$$

This K_{eff} is a constant (homogeneous and steady) that may be taken outside of the gradient operator, and the eddy flux term may be estimated as

$$\overline{\mathbf{v}' c'} = -K_{eff}\, \nabla C.$$

The direction of the eddy flux comes from the assumption that it will be anti-parallel to the gradient of C, i.e., the usual sense of a heat flux from hot to cold. The Reynolds-averaged advection equation (38) can then be written as an advection/diffusion balance for the resolved tracer C,

$$\frac{\partial C}{\partial t} = -\mathbf{V} \cdot \nabla C + K_{eff} \nabla^2 C + K_c\, \nabla^2 C. \tag{45}$$

The process of the eddy flux — a fast time and short space scale random advection — has thus been parameterized as an effective diffusivity, $K_{eff} = \frac{1}{2} sw$, acting upon the resolved tracer field.[16]

To check that this parameterization of eddy flux is indeed appropriate for this case, the statistics of the random walk may be compared with the solution for suitably calibrated two-dimensional, Fickian (classical) diffusion,

$$\frac{\partial C}{\partial t} = K_c\, \frac{1}{r}\, \frac{\partial}{\partial r} \left(\frac{r\, \partial C}{\partial r} \right)$$

Assume an initial condition that corresponds to the experiment of Fig. (14), a radially symmetric and highly localized delta function of tracer C centered over the origin, and a boundary condition that tracer concentration vanishes at infinity,

$$C(r,\, t=0) \propto \Delta(r), \quad \text{and} \quad C(r,\, t) \to 0 \ \text{ as } \ r \to \infty.$$

The solution for C is then a Gaussian

$$C(r,t) = \frac{1}{2\pi\, \sigma^2} \exp\left(\frac{-r^2}{2\sigma^2} \right), \tag{46}$$

with a time-dependent standard deviation σ,

$$\sigma(t) = \sqrt{2\, K_c\, t}.$$

[16] A parameterization provides an estimate of something that would otherwise remain unknown, in this case an eddy flux, in terms of something that is known at least in principle, here the statistics of a random walk and the gradient of the resolved tracer field. It is important to keep in mind that a parameterization is not an identity, and will not be valid universally. Rather, parameterizations are likely to be more or less *ad hoc* and useful over a limited range, which may be very difficult to define fully and precisely. Most parameterizations should be treated with some skepticism, and subjected to testing whenever possible. This is especially important when the parameterization exerts a significant influence upon the end result of a model or an analysis, as it does here.

This is often said to be the 'fundamental solution' for 2-d diffusion. To compare this solution with the random walk, choose $K_c = K_{eff} = w\,s/2 = 0.01$ (dimensional units of K are $[length^2\ time^{-1}]$). The solution (46) and the particle count histogram shown in Fig. (15), right, have been normalized to give a net particle count of $N = 500,000$, consistent with the random walk ensemble.

The time-dependent standard deviation and the instantaneous distribution particle density of the random walk are, superficially, indistinguishable from this solution for Fickian (classical) diffusion (46), Fig. (15). This is a well known result, and yet it is still a little bit surprising, considering that advection and diffusion are quite different processes.[17] A conclusion drawn from this comparison is that the familiar usage 'diffusion' and the parameterized advection/diffusion equation (45) are useful terms and concpets in an Eulerian theory that seeks to describe the dispersal of particles that occurs in a (Lagrangian) random walk.[18]

Figure 16: Stirring and mixing:

Spinning, shearing flows
wrapping tracer filaments
that embrace and merge.

4.4 Stirring and mixing: when advection and diffusion act at once, Peclet number

The random walk and the vortex flows of Sec. 3 have been combined on the assumption that the two flows are independent. As we will see, their joint effect may not be a linear addition, however.

The initial condition for these experiments had the particles (N = 10,000) uniformly distributed over a circular area of radius 0.1 and centered on $(x,\ y) = (0,\ 1)$. The perimeter of this circle was advected by

[17] There are limits in which random walk and diffusion do indeed give quite different results. Consider that classical diffusion follows a parabolic partial differential equation that requires all boundary data at all times up to the present. Even the most distant boundary will thus have an some effect, even if infinitesimal, on every point in the domain of a classical diffusion problem. By contrast, the maximum speed at which a random walk can propagate a signal is just $|w|$, which is finite, as it should be, physically. In that regard, a random walk would appears to be a more plausible representation of a physical process than is classical diffusion. For more on this see Keller, J., 2004, Diffusion at finite speed and random walks, Proc Natl Acad Sci U S A. 101(5): 11201122. Published online 2004 Jan 20. doi: 10.1073/pnas.0307052101

[18] The success of the mixing length parameterization in this case is so compelling that you might be led to expect similar success in other cases, and in other problems. Probably not! More likely is that the eddy velocity will be inhomogeneous, anisotropic and dependent upon the resolved velocity shear, among others. In that event, a constant and isotropic effective diffusivity will not obtain the way it did in this especially simple case of a random walk that was independent of the resolved flow. A good strategy might be to regard the mixing length hypothesis as a null model, and then see if you can devise a better model by taking account of the specific eddy process(es) in your problem.

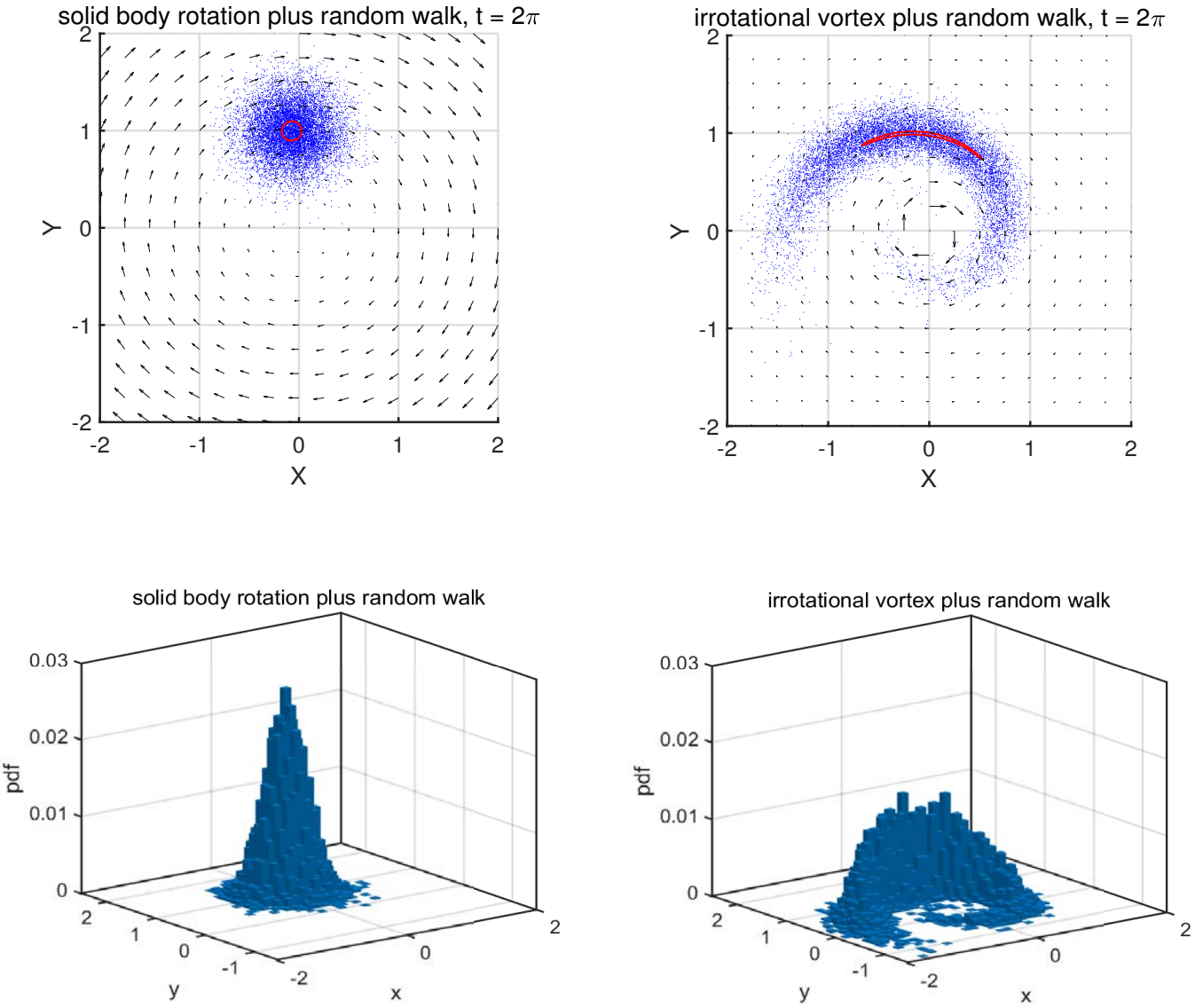

Figure 17: Advection plus random walk of freely drifting particles placed into a solid body rotation **(left)** and into an irrotational vortex **(right)**. The initial perimeter of the particle cloud is in red outline at upper left, and was advected by the vortex flow, but not subject to the random walk. This is intended to show deformation, which occurs in the irrotational vortex at right, but not in the solid body rotation at left. The upper panels are snapshots at $t = 2\pi$ and one complete revolution, and the lower panels are the corresponding probability density distributions (10,000 particles and 900 bins). The solid body rotation leaves the cluster perimeter unchanged, while the random walk diffused particles into the surrounding fluid. The irrotational vortex caused the cloud to be deformed into a thin filament which consequently had a significantly increased perimeter. As a result, there was enhanced diffusion of the particles out of the initial cloud, as evidenced by the much reduced peak in the histogram. Animations of these experiments are available at https://www2.whoi.edu/staff/jprice/wp-content/uploads/sites/199/2022/07/sm-solid.mp4 and https://www2.whoi.edu/staff/jprice/wp-content/uploads/sites/199/2022/07/sm-irrot.mp4

the prescribed vortex flow (solid body or irrotational), but not diffused, and shown by the red outline (Fig. 17) to give an indication of deformation. The distribution of particles after a time $t = 2\pi$ and one full revolution of either vortex at $r = 1$ is in Fig. (17). The solid body rotation and irrotational vortices gave remarkably different particle distributions.

How to describe and interpret what we see here? If our interest is what happens within the fluid itself, then a description that follows the particle cloud is appropriate and is discussed in the next section. If the goal is to describe the particle density at a fixed location, then diagnosing the particle budget over a control volume is appropriate, Sec. 4.4.2.

4.4.1 Following the particle cloud, the Lagrangian view

One straightforward and useful diagnostic is the area of the cloud. This may be estimated from a histogram of particle positions (Fig. 14) by summing the area of the bins that have at least one particle. This gives an upper bound on the cloud size. These statistics have been estimated over four experiments. The first two of these serve mainly to calibrate our view of diffusion and advection taken separately, and then the third and fourth experiments reveal the phenomenon of interest, stirring and mixing.

No diffusion. First, consider that there is no diffusion, and that advection is by the solid body rotation (the red line, no random walk, of Fig. 18, left). In that case the cloud size remains constant at the initial value, $\pi r_0^2 = 0.03$. The same holds for advection by the irrotational vortex.

No advection. Second, consider that there is a random walk, but with no advection (the magenta line of Fig. 18), left. The particle cloud expands, isotropically, as in Figs. (14) and (15), and the area grows linearly in time as $\text{area} \propto \sigma(t)^2 = K_{eff}\, t$. To make an equality of this relation requires a factor of about 9 multiplying the right side to account for the difference between the standard deviation of the particle distribution σ, and the leading edge of the particle cloud, which is about a factor of 3 greater.

Solid body rotation plus diffusion. Third, suppose that there is diffusion as well as advection by a solid body rotation, the solution of Fig. (17), upper left. The area of the expanding cloud in this experiment (the blue line of Fig. 18, left) is virtually identical to that found with diffusion alone. The clear conclusion from this is that advection (absent deformation) and rotation, as occurs in a solid body rotation, have no effect on the diffusive growth of the particle cloud.

Irrotational vortex plus diffusion. Fourth, and most interesting, is the case of diffusion plus advection by the irrotational vortex (Fig. 17, upper right). The irrotational vortex causes a strong deformation of the particle cloud as seen before, which does not by itself change the area of the particle cloud. But, when deformation is combined with diffusion, the result can be a fairly dramatic increase of cloud size, here about a factor 3 (cf. the blue and green lines of Fig. 18, left). The large increase in cloud area follows from the deformation of the cloud into a long filament, which would be very thin absent diffusion. The initial particle cluster was a circular area having radius $r_o = 0.1$ and an initial circumference of $0.2\pi \approx 0.63$. The deformation of the irrotational vortex extended (stretched) the sides of the initial cluster at a rate $2r_o\Omega$, which caused the circumference to grew almost linearly with time, from 0.6 to about $0.4\Omega T \approx 13$ by the end of the experiment, five revolutions, $t/2\pi = 5$. Diffusion acting across the greatly increased perimeter of the particle cloud was much more effective at mixing particles into the

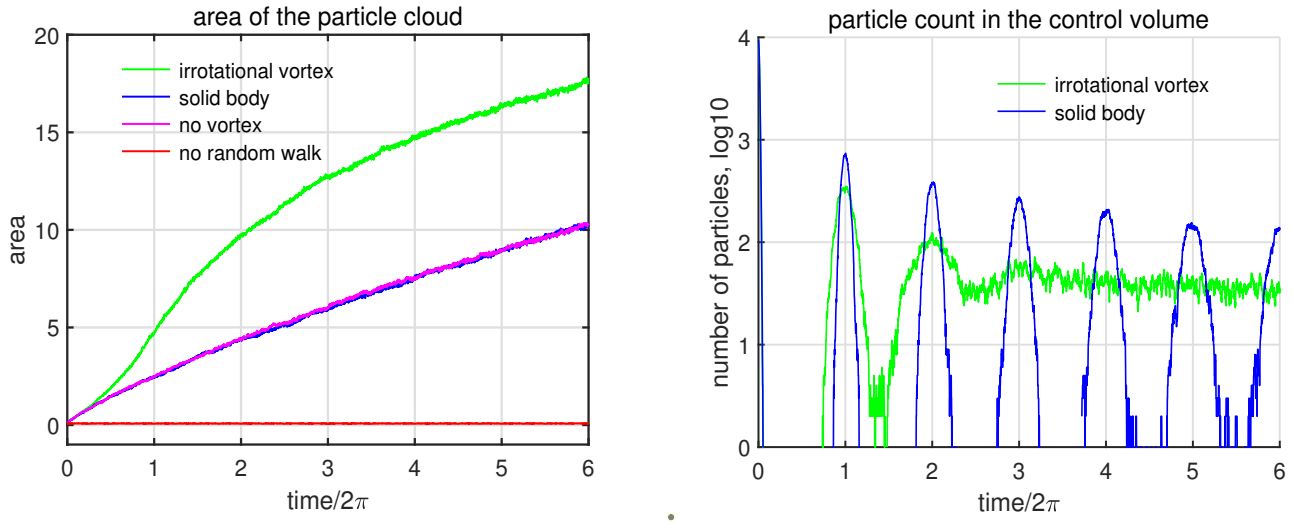

Figure 18: Lagrangian and Eulerian views of the evolving particle distribution. **(left)** The area of the cloud estimated as the sum of the area of every histogram bin (Fig. 17, lower) having at least one particle. Other possible measures of the area, e.g., the e-folding width squared, will give smaller estimates of the area, but similar time-dependence and comparison of one case to another. There are four experiments shown here. The red line is for a case having no random walk, and advection by either kind of vortex; area is conserved. The magenta line has the random walk with no vortex flow. The blue line is random walk plus a solid body rotation, and is indistinguishable from the random walk only case. Lastly, the green line is the random walk plus advection by an irrotational vortex. **(right)** The particle count in a control volume that at $t = 0$ coincided with the initial particle positions (the red circle at 12 o'clock in Fig. 17, upper left). The vortex flows were either an irrotational vortex (green line) or the solid body rotation (blue line). There was a large pulse of particle count at time intervals of 2π as the particle cloud was carried into and then out of the CV by the vortex flow. This advection signal was much more persistent in the solid body vortex case than in the irrotational vortex case. In the latter case, the particle concentration was nearly isotropic after about three revolutions, and so the signal of azimuthal advection was nearly extinguished thereafter.

surrounding fluid than was diffusion acting on a symmetric particle cloud, cf. the green and blue lines of Fig. (18), left.

A closer look at this last solution shows that the rate of increase of the area had three fairly well-defined stages. For very short times, $t/2\pi \leq 0.2$, the increase in area was the same for the solid body rotation case and the irrotational vortex case. Deformation was not significant for very short times while the particle cloud was still fairly compact and isotropic (round). During an intermediate time, $0.5 < t/2\pi < 4$, deformation caused a significant increase in the growth rate as described above. At still longer times, $t/1\pi > 5$, the particle cloud had been wrapped completely around the vortex center, and the particle distribution was almost isotropic thereafter. Further deformation was of little or no consequence. The area of the cloud continued to grow slowly as particles were diffused outward to larger radius.

4.4.2 Watching a control volume, the Eulerian view

If the need was to characterize the particle density field, that is, particle density at fixed points in space, then a different approach is required. One way is to take the particle count within a control volume (CV) (in this 2-d domain, actually a control area) that can be any size and shape. Here the CV was taken to be coincident with the initial particle launch region, a circular area with radius 0.1 centered on $(x,y) = (1,0)$ and fixed in space.

Solid body rotation. The solution for the case of solid body rotation plus diffusion is in Fig. (18), right, the blue line. This is very different from the prvious (Lagrangian) characteriztion of cloud size. The particle count shows a very pronounced, periodic pulse at time intervals of 2π as the particle cloud is advected into and then out of the CV (this is fairly obvious, but is easier to see in the animation linked in the caption of Fig. 17). Advection by the resolved vortex velocity thus has a dominant effect on the particle count in a fixed CV.

The full advection/diffusion equation, Eq. (45) is relevant to the particle field in this Eulerian frame. Advection and diffusion are distinct processes, and the Peclet number,

$$Pe \propto \frac{\text{advection tendency}}{\text{diffusion tendency}} \propto \frac{|\mathbf{V}\cdot\nabla C|}{|K_{eff}\nabla^2 C|} \propto \frac{UC/L}{K_{eff}C/L^2} \propto \frac{UL}{K_{eff}},$$

provides a framework that will help us think in quantitative ways about their comparative magnitude. U is the scale of the resolved vortex velocity that does the advection; $U = U_\theta = 1$ at $r = 1$ is appropriate. $K_{eff} = 0.01$ is the effective diffusivity in these experiments. In this problem (and often) the interesting thing turns out to be the length scale, L, that characterizes the tracer distribution in the sense that $\partial C/\partial x$ is O(C/L) and $\partial^2 C/\partial x^2$ is O(C/L^2). C is the spatially-varying part of the C field, which divides out of this Pe. The L is taken to be the initial radius of the particle cloud and so $L = 0.1$. Given these parameters, $Pe = 10$, and the inference is that the evolution of the particle density at a fixed site will be due mainly to advection. In the case of the solid body rotation and the fixed CV (Fig. 18, right, blue line), it clearly is, at least during the first few revolutions of the vortex flow.

The effect of diffusion by the random walk was to broaden the particle cloud over time, resulting in a reduced peak amplitude of the particle count on each successive pass through the CV. Nevertheless, the local rate of change of C (or particle number) within the fixed CV was still due mainly to advection, since larger L (even though caused by diffusion) favors advection compared with diffusion. If U is made smaller or K_{eff} is made larger, then the expected qualitative changes implied by a smaller Pe are realized, i.e., a greater effect of diffusion than in the nominal case. However, for $Pe > 1$, advection dominates the instantaneous balance at intermediate and long times unless the relationship of $\mathbf{V}$ and ∇C changes significantly, which it may (discussed further below).

Another form of Peclet number, a displacement Peclet number, illustrates explicit dependence upon elapsed time,

$$Pe_d = \frac{\text{advection distance}}{\text{diffusion distance}} = \frac{U\,t}{\sqrt{K\,t}} = \frac{Un}{w\sqrt{n}},$$

the ratio of advection distance to the diffusion distance at time, t (and note that n is a pure number with no physical dimension). At very short times, say one step of the random walk, $n = 1$, and given that $U = w$, the motion of a single particle is due equally to the resolved flow and the eddy velocity. At long

times, after many random steps, the displacement of a particle will be due mainly to the advection distance, which grows as $t \propto n$, vs. the diffusion distance which grows as $\sqrt{t} \propto \sqrt{n}$.

Irrotational vortex During the first several revolutions, time$/2\pi < 2$, the azimuthal advection was much as it was in the previous experiment, but after about $t/(2\pi) > 3$, the signal of advection was nearly extinguished.

What happened to *Pe*? The Peclet number makes use of one length scale to characterize the first and second derivatives of the tracer field (the particle cloud) that are relevant to advection and diffusion. The dependence upon one length scale is plausible at the start of an experiments when the particle cloud was isotropic. However, this may fail dramatically when the particle cloud has evolved far from the initial condition, in this case into a long and very thin filament. The appropriate length scale for the advection term should represent the component of the gradient that is parallel (or anti-parallel) to the advecting velocity. After about three revolutions of the irrotational vortex, the particles were smeared out over a cloud that was nearly azimuthally symmetric, and hence the advection effect due to the azimuthal velocity was greatly diminished compared with the advection of the initial condition. The appropriate length scale for diffusion is the smaller of the width and the length of the particle cloud, which can be very different when deformation stretches the particle cloud into a thin filament, as it has here. Thus the Pe estimate made from the length scale $L = r_o$ appropriate to the initial condition was not relevant once the particle cloud had evolved far away from the isotropic initial condition. Indeed at long times, further evolution of the particle cloud was due mainly to diffusion, just as it is in the Lagrangian description of the previous subsection.

The important result of this last calculation is that the combined effect of deformation and diffusion produced a near-homogeneous equilibrium much more rapidly than would occur in the absence of deformation, i.e., by diffusion acting alone. At this level of detail, there is a significant difference between diffusion by a small scale random walk (or molecular diffusion) which acts to reduce tracer gradients by mixing, and a deformation rate by the resolved flow, often called 'stirring' when it is quasi-random, which acts to increase mean square gradients.[19]

Reversible stirring. The deformation caused by the irrotational vortex after one revolution may be undone by simply reversing the direction of the vortex (Fig. 31) while omitting the random walk. After another 2π elapsed time, the initial particle cloud (the red outline) returned to its starting position; the resolved scale deformation, even though quite large, is reversible. The dispersal of particles by the random walk does not reverse, however, unless we were to store each step for each particle, about 6,000,000 in total, and played that tape backwards.[20]

[19] An excellent introduction to stirring and mixing is by Thiffeault, J-L., 2010, Lecture 1: Stirring and mixing. Notes by S. Pegler and A. O'Rourke. https://www2.whoi.edu/staff/jprice/wp-content/uploads/sites/199/2023/11/Thiffeault-SM.pdf. A very interesting discussion of the Peclet number as a measure of deterministic vs. random process is by Gommes, C., and J. Tharakan, 2020, The Peclet number of a casino: Diffusion and convection in a gambling context. A. J. Phys., 88(6), 439-447. https://ui.adsabs.harvard.edu/abs/2020AmJPh..88..439G/abstract A simple Matlab script you can use to integrate this case and the other vortex flows discussed in Sec. 5.4 is https://www2.whoi.edu/staff/jprice/wp-content/uploads/sites/199/2023/12/stirandmix.txt

[20] An animation of this case is https://www2.whoi.edu/staff/jprice/wp-content/uploads/sites/199/2022/08/sm-unwind.mp4

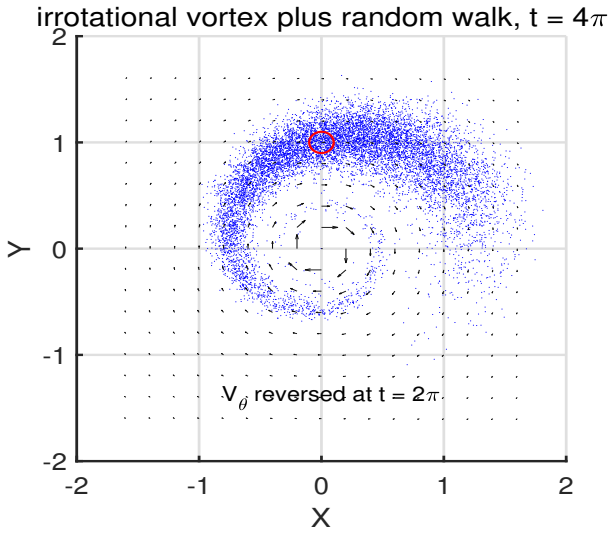

Figure 19: Can the stirring and mixing be reversed? The end state of the irrotational vortex/random walk experiment, Fig. (17), lower left, was used as the initial state of a follow-on experiment in which the direction of rotation was reversed and the integration continued until $t = 4\pi$. The perimeter of the initial particle cluster (red circle) was restored exactly, but the diffusion of particles was not.

4.5 Appendix: The Lamb-Oseen vortex

We now have most of the pieces in place to understand a phenomenon called the Lamb-Oseen (LO) vortex. This has only a tangential connection with the Lagrangian-Eulerian theme of this essay and so is included as an appendix. The LO vortex is nonetheless interesting in that it bridges the apparently huge divide between an irrotational vortex and solid body rotation. The solution of the LO vortex is also one of the few simple, time-dependent solutions of the Navier-Stokes equations.

4.5.1 How to make a starting vortex

The LO vortex can be thought of as an idealization of the starting vortex that forms behind an airplane wing, or, a teaspoon pushed through a tea cup. High pressure (relative high free surface height) builds up in front of the accelerated spoon and low pressure occurs behind. A starting vortex forms as fluid flows around the edge of the spoon from higher to lower pressure. Since the fluid that makes up most of the vortex is driven mainly by this pressure gradient, most of the fluid within the vortex is free of vorticity. A comparatively small volume of fluid makes contact with the spoon through a thin viscous boundary layer that imparts vorticity having a sense that is consistent with the swirling motion of the larger vortex (negative if clockwise). Most of this vorticity is concentrated in a compact, central core. The core is surrounded by fluid that is in vortical motion, but is nevertheless vorticity-free.[21]

The strength of the vortex may be measured by the circulation, C,

$$C = \oint \mathbf{V}\cdot\mathbf{ds} = \iint (\nabla\times\mathbf{V})\cdot\mathbf{n}\, da = \iint \chi\, da, \tag{47}$$

[21] An isolated vortex having one sign of vorticity is oftentimes referred to as a monopole and described as if two-dimensional, as here. In practice, the vortex formed by a spoon pushed through a tea cup will be three-dimensional, with a continuation along the bottom edge and connecting to a mirror image vortex on the opposite side (e.g., Fig. 2, Part 1). That there is a vortex pair, rather than an isolated monopole, is of considerable importance in the evolution of the flow.

the line integral of velocity around a closed loop. By Stokes' Theorem,[22] this line integral is equal to the total flux of vorticity, $\nabla \times \mathbf{V} \cdot \mathbf{n}$ through any surface that is bounded by the loop. In the two-dimensional case of interest here, C is also equal to the areal integral of the (scalar) vorticity, χ, over the surface that is bound by the loop. If the loop does not surround the vortex core, then $\chi = 0$ everywhere over the surface, and so $C = 0$. If the loop does enclose the vortex core, then $C = \tilde{z}$, which can be termed the vortex strength.

4.5.2 Diffusion of vorticity

If the vorticity is highly localized, then the initial distribution $\chi_o(r)$ may be idealized as a delta function of r,

$$\chi_o \;=\; \tilde{z}\,\delta(r)\;. \tag{48}$$

Assuming an integration path that is a circle of radius r centered on this core, then Stokes' Theorem shows that

$$V_\theta(r) \;=\; \frac{\tilde{z}}{2\pi r}, \tag{49}$$

the velocity profile that we have been calling an irrotational vortex. This V_θ has a singularity at the origin which is unphysical; vorticity may be highly localized, but in a real fluid it can not be a literal delta function on account of viscosity, if nothing else. To allow that the initial vortex core will have a finite width, σ_o, the delta function of Eq. (48) may be represented by a normalized Gaussian,

$$\tilde{z}\,\delta(r) \;\approx\; \frac{\tilde{z}}{2\pi\sigma_o^2}\,\exp\left(\frac{-r^2}{2\sigma_o^2}\right), \tag{50}$$

that may be made arbitrarily narrow, $\sigma_o \to 0$, to give a strongly peaked distribution having the integral properties of a delta function. In the example below of an LO vortex in water, $\sigma_o \;\approx\; 0.1$ cm (by inspection).

We have seen that an irrotational vortex will have significant deformation near the core that will enhance the mixing of particles and presumably vorticity into the outlying fluid. On the reasonable assumptions that the vortex is azimuthally symmetric and that the radial velocity is negligible, then the vorticity of the vortex will evolve according to the linear diffusion equation,

$$\frac{\partial \chi}{\partial t} \;=\; \nu\nabla^2\chi \;=\; \nu\,\frac{1}{r}\,\frac{\partial}{\partial r}\left(r\,\frac{\partial \chi}{\partial r}\right), \tag{51}$$

where ν is the kinematic viscosity of the fluid. If water at room temperature, $\nu \approx 0.01$ cm^2 sec^{-1} (note the CGS units). The initial condition is Eq. (48) plus (50) and the boundary condition is $\chi \to 0$ as $r \to \infty$. The solution for the vorticity distribution is then the fundamental solution of the two-dimensional heat equation, Eq. (46) and (Fig. 20, upper),

$$\chi(r,t) \;=\; \frac{\tilde{z}}{4\pi\nu(t+t_o)}\,\exp\left(\frac{-r^2}{4\nu(t+\pi t_o)}\right) \tag{52}$$

[22] https://www.byjus.com/maths/stokes-theorem

modified with a time offset $t_o = \sigma_o^2/(2\pi\nu) \approx 0.15$ sec to allow for a finite core of radius σ_o and the χ_o of Eq. (48). As time runs, vorticity diffuses into the surrounding fluid, and the associated azimuthal velocity is (Fig. 20, center),

$$V_\theta(r\,t) \;=\; \frac{1}{r}\int_0^r r\,\chi\;dr \;=\; \frac{\tilde{z}}{2\pi r}(1 \;-\; \exp(\frac{-r^2}{4\nu(t+\pi t_o)})). \tag{53}$$

4.5.3 The inner core, solid body rotation

This solution has two familiar limits. In the inner core of the vortex, $r << \sqrt{4\nu t}$ (small r or large t), the vorticity is quasi-uniform with r and decaying in time. The velocity of the inner core increases linearly with r and decreases in time,

$$V_\theta \;\approx\; \frac{\tilde{z}r}{8\pi\nu t}, \quad \text{a decaying, solid body rotation.}$$

At large radius or small time, $r >> \sqrt{4\nu t}$, the vorticity is very small and steady, and the azimuthal velocity decreases as $1/r$,

$$V_\theta \;\approx\; \frac{\tilde{z}}{2\pi r}, \;\text{the initial, irrotational vortex, not yet affected appreciably by viscosity.}$$

This solution for a time-dependent diffusive vortex, known as a Lamb-Oseen vortex, shows how an irrotational vortex, which has significant deformation and viscous stress, will evolve in time into a solid body rotation which has vorticity but no deformation or viscous stress. A solid body rotation could thus be steady, except that the velocity profile $V_\theta \propto r$ insures that a solid body will sooner or later interact with surrounding fluid or boundary.

The pressure anomaly associated with the displaced free surface, $P = \rho g z$, has no dynamical role in the vorticity balance (51). However, a pressure anomaly has an essential role in the momentum balance, insofar as it provides the radially-inward, centripetal force required to provide a quasi-static balance to the centrifugal force of the azimuthal velocity. The free surface displacement may be computed from a steady, radial force balance

$$\frac{V_\theta^2}{r} \;=\; g\frac{\partial z}{\partial r}$$

integrated from the far field inwards (Fig. 20, lower),

$$z(r) \;=\; -\int_\infty^r \frac{V_\theta^2}{gr}\,dr \;+\; z(\infty).$$

Notice that the free surface in the vortex center is a relative low, regardless of the sense of the azimuthal flow. This is not the case for much larger, geophysical vortices that are significantly influenced by the Coriolis force (next Sec. 7). The free surface displacement is especially easy to observe and so is a useful diagnostic (for more on the free surface see Problem 4 below).

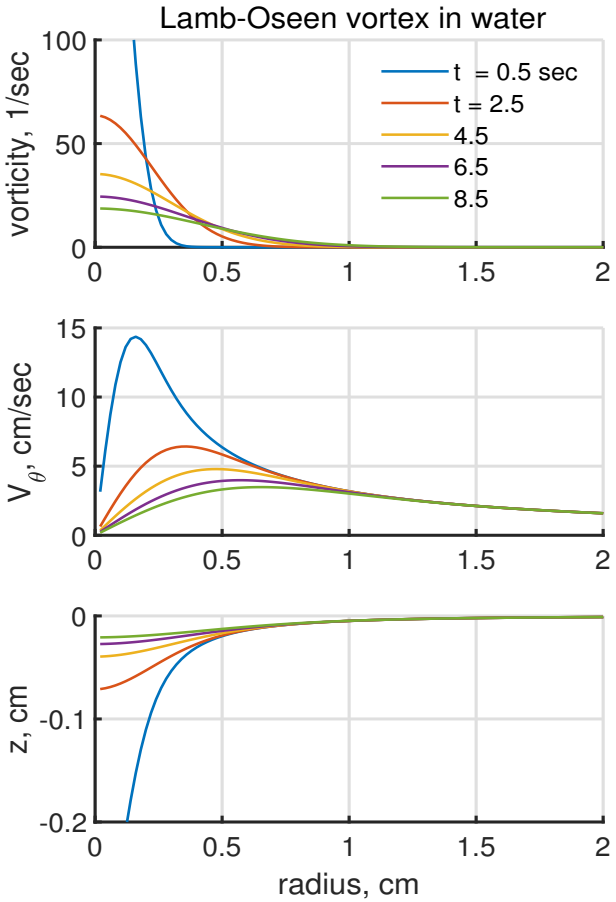

Figure 20: Some properties of a Lamb-Oseen vortex in water having $\tilde{z} = 20$ cm^2 sec^{-1} and $\nu = 0.01$ cm^2 sec^{-1}. The vorticity **(upper)** was initially concentrated very near the origin, and then diffused outward with time. The azimuthal velocity **(middle)** and the free surface displacement **(lower)**. The dimensional scales are those of a small irrotational vortex in water. Profiles are shown at 2 sec intervals, beginning at $t = 0.5$ sec. Even at very short times, 0.5 sec, there was a discernible core of the vortex that was in solid body rotation. Outlying regions, $r > 1$ cm, were irrotational (velocity decreasing as $1/r$) for the duration shown here.

4.6 Key ideas

1 The basis for some improved algorithms for estimating advection is the notion that parcel trajectories are the characteristics of an advection equation.

2 All real fluid flows have a more or less wide range of time and space scales: for a tea cup, about one order of magnitude; for the atmosphere, about ten orders of magnitude. The first step of an analysis will be the definition of the scale(s) that will be resolved, and those that will have to be left unresolved, frequently smaller time and space scales.

3 Linear (Reynolds) averaging may be used to define the resolved scale, and implicitly the unresolved or eddy scales. The net effect of the eddy motion on the resolved scale may often be accounted as an eddy flux, the cross-correlation of the eddy velocity and an intensive fluid property.

4 The classical mixing length theory yields a parameterization of the eddy flux as an effective diffusivity, K, acting on the resolved tracer field. This may work well when the eddy velocity is a random walk, isotropic, homogeneous and independent of the larger scale. It should not be taken as a general solution/parameterization of eddy fluxes.

5 The Peclet number UL/K can make a useful estimate of the magnitude of advection by the resolved scale compared with diffusion $\propto K$ provided that a single length scale L is appropriate for both the gradient and the Laplacian operators. This is likely to be violated as the tracer field evolves with time.

6 A very important consequence of advection is that it may (usually will) be accompanied by deformation that changes the shape of fluid parcels. If sustained, deformation will tend to produce long and thin streaks of tracer that have a greatly increased perimeter and thus much more readily diffused into the surrounding fluid compared with tracer in a zero deformation flow. Random deformation is often described as stirring, and the combined effect of stirring and mixing (diffusion) leads to comparatively rapid homogenization.

4.7 Problems

1) Given that the actual velocity **v** is nondivergent, apply a Reynolds averaging procedure to show that the resolved velocity and the eddy velocity are also nondivergent.

2) Arguably the most important characteristic of a random walk is that the long term, ensemble mean displacement measured by the root mean square of x, y or r grows as the square root of time. Can you explain how this comes about in a few sentences? Can you use the formalism of Eqs. (41) and (42) to describe the growth of correlated motion, i.e., a mean flow (as opposed to a random walk)?

3) A good example of a resolved flow in which to examine stirring and mixing is a confluent flow, $u(x,y) = b\,x$ and $v(x,y) = -b\,y$ (Problem 6 of the previous section). Consider a random walk in this flow. At long times, the tracer will be confined to an increasingly narrow filament that is parallel to the $x-$axis. At some long time, the dispersion of particles away from the ever-lengthening and thinning filament will be balanced by the ongoing linear deformation, a compression, yielding an equilibrated filament width, albeit with ever-diminishing particle concentration. Can you test that the balanced width of this filament is closely proportional to the Batchelor scale, $L_B = \sqrt{K/b}$? What causes the particle concentration to decrease? An animation of this case is available from
https://www2.whoi.edu/staff/jprice/wp-content/uploads/sites/199/2022/08/confluence.mp4

4) Given the solution of a Lamb-Oseen vortex, Eq. (53), show that the free surface in the core of the initial vortex is $z \propto 1/r^2$, while the core is in irrotational motion (only a very short time, tenths of seconds). The free surface at the center of the vortex then appears to have a noticeable dimple. But after viscosity has diffused vorticity away from the center, and an appreciable central region is in solid body rotation, show that the free surface is then $z \propto r^2$and the free surface at the center of the vortex appears to be flat. Look for this rapid (less than a second) transition in the shape of the free surface in the vortices you can make by pushing a paddle (or any flat object) through still water. (Were you surprised by how viscous water appears to be in this context? I was.)

5 Models that combine Lagrangian and Eulerian concepts

A wide variety of numerical models have developed around the idea of combining the most advantageous aspects of Lagrangian and Eulerian methods and concepts. Hybrid models are feasible because numerical models have the option to treat the different terms and processes of an equation of motion or tracer balance by wholly different methods. Thus, advection may be treated by a Lagrangian (parcel-tracking) method, Sec. 5.1, while the pressure field might be better evaluted by mapping fluid properties (e.g., mass density) on to a fixed, Eulerian grid, Sec. 5.3.

5.1 Numerical treatments of advection

This subsection 5.1 will consider finite difference methods for solving a one-dimensional tracer advection problem, first by a purely Lagrangian method, then a purely Eulerian method, and then finally by a hybrid method called semi-Lagrangian. This latter method is called semi-Lagrangian because parcel identity is retained only for short times. Such semi-Lagrangian treatments of advection are very widely used, and are a significant motivation for understanding both Lagrangian and Eulerian systems.

The test problem will be the one-dimensional, time-dependent balance of a passive tracer, $c(x,\ t)$,

$$\frac{D\ c(x,t)}{D\ t}\ =\ Q(x,t). \tag{54}$$

The initial tracer distribution is a two-level, top-hat pulse of half width 1,

$$c(x,t=0)\ =\ c_o(x),$$

which has sharp edges (Fig. 21, left, the blue line). The boundary condition is that tracer goes to zero at very large $\pm x$. A current is specified as

$$u(t) = U_0\ sin(10\pi\ t/t_M), \tag{55}$$

where t_M is the duration of the experiment, 10,000, and t/t_M is the normalized time. The current amplitude $U_0 = 0.01$ is sufficient to carry (advect) the tracer pulse back and forth across the model domain ten times, and with a displacement that is several times the initial pulse width. The external source Q is also presumed to be a known function of time,

$$Q\ =\ Q_o sin(J\pi\ t/t_M),$$

with J the number of half-cycles, and could be, e.g., heating by solar insolation. There is no diffusion and so this is otherwise an ideal fluid. The one-dimensional geometry assumed here minimizes algebra and eases the presentation, but it is not general: important complications can arise in two or three space dimensions that will be noted toward the end of Sec. 5.1.

This problem has an exact solution that may be found by the method of characteristics (see Problem 2) at the end of this section). In the exact solution, and assuming $Q = 0$, the tracer profile will overlay the

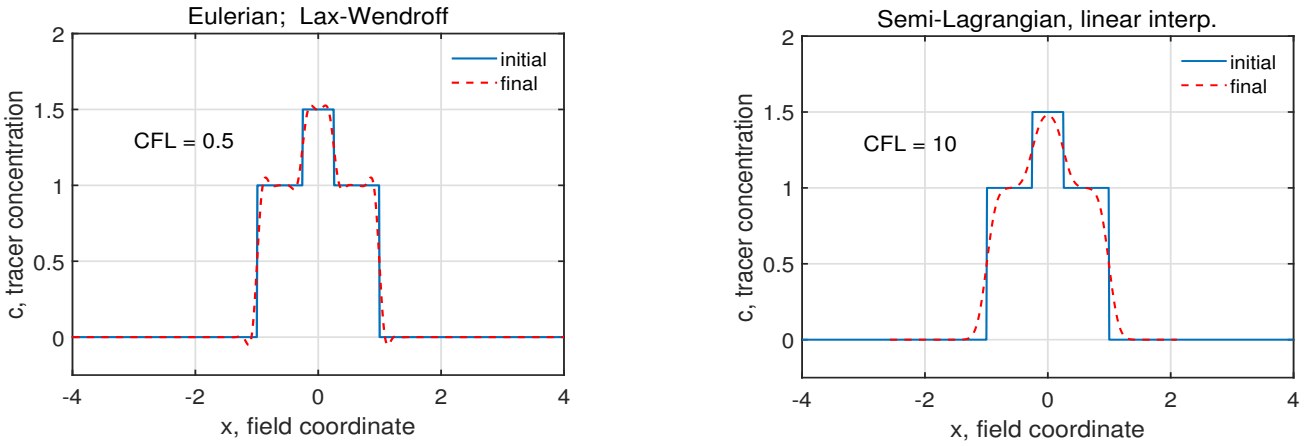

Figure 21: Tracer advection experiments solved by numerical methods on a one-dimensional domain. The initial tracer distribution was a two-level top-hat (solid blue line) that was advected back and forth across the center of the domain through ten complete cycles. An exact solution will have the end time solution (red dashed line) overlay the initial distribution. The left panel is the solution computed with an Eulerian second order Lax-Wendroff scheme with a time step $\delta t = 0.5$, and CFL = 0.5. The right panel shows the solution computed with a semi-Lagrangian scheme (Sec. 5.1.3) using a linear interpolation to evaluate the tracer at the estimated parcel departure positions. This solution was computed with a considerably larger time step, $\delta t = 10$ and so CFL = 10. These solutions display roughly comparable though quite different errors: high frequency noise in the Lax-Wendroff solution, and diffusive-like broadening of the pulse in the semi-Lagrangian solution. A significant practical difference is that the semi-Lagrangian solution required far fewer steps.

initial profile at every half cycle of the current, Fig. (21).

5.1.1 Discretized data and numerical solution

One-dimensional models and exact solutions are *not* the usual fare of fluid mechanics. Rather, most real problems and certainly most research problems require solution by numerical methods that can treat multi-dimensional and nonlinear systems. (Of course, exact solutions to highly simplified problems can be essential as a means to check and to interpret numerical solutions.)

To represent a tracer distribution within a one-dimensional numerical calculation requires at least two discrete arrays, one that represent the tracer,

$$c = [c_1 \;\; c_2 \;\; \ldots \, c_N],$$

with N the number of elements, or nodes, and a second array that represents space,

$$x = [x_1 \;\; x_2 \;\; \ldots \;\; x_N],$$

and that is in a one-to-one correspondence with c. We could also include an array of times, but this is peripheral to the main point. The same comment applies to the source term, Q, and to the current, u.

The space coordinates could be interpreted in one of two ways depending upon whether the calculation will take a Lagrangian or an Eulerian prespective. The x_n could be regarded as the time-dependent $\tilde{x}$-coordinates of moving parcels; the $\tilde{x}_n$ is then the position of the $n-$th parcel having tracer c_n. A superscript time index on $\tilde{x}$ is essential, i.e., $\tilde{x}_n^i$, while the corresponding $\tilde{c}_n$ are constant, and so do not require a superscript to denote the time. There is generally no need to keep all of the time levels, $t = [t_1 \ t_2 \ \ldots \ t_M]$, but notice that $t^i = i\,\delta t$ with δt the time step. If we let $(\ )^i$ be the present time level, then $(\ )^{i+1}$ is the next time level. This is, of course, Lagrangian view of (54), and the tilde is our notational convention that distinguishes Lagrangian from Eulerian variables when they are being considered side-by-side as here.

Alternatively, the x_n could be field coordinates, i.e., the fixed positions in space where we seek the solution for the time-dependent tracer. In that case the x nodes could be spaced equally at grid interval δx and so $x_n = n\delta x$ and $L = N\,\delta x$ is the width of the domain. The tracer is then time dependent, and so requires a time superscript, c_n^i is the i-th time (the present time) value of c at the n-th node.

To summarize, a discretized view of the tracer balance (54) can be either

Lagrangian: the time-varying position of parcels, $\tilde{x}_n^i$, each of which have a fixed tracer, $\tilde{c}_n$, or,

Eulerian: a time-varying tracer, c_n^i, defined on fixed field coordinates, x_n.

In several key respects the discussion that follows is in parallel with the method of characteristics (Part 1, Sec. 4). And specifically, the source term may often be dealt with separately from the advection term. If, the source term is external, e.g., solar insolation, then the only restriction on the time step is that it must be small enough to resolve the temporal variation of the source. If solar insolation, tens of minutes or hourly will probably suffice. Solving for the advection process is more challenging.

5.1.2 Lagrangian advection of parcels

This problem is very simple when viewed from a Lagrangian perspective. The adiabatic tracer balance is just

$$\frac{D\,\tilde{c}_n}{Dt} = \frac{\partial \tilde{c}_n}{\partial t} = 0, \tag{56}$$

or in other words,

$$\tilde{c}_n = c_{on},$$

and the tracer value on each moving parcel is fixed in time at the initial value. The entire phenomenon is contained in the motion of the parcels given by the trajectory equation,

$$\frac{\partial\,\tilde{x}_n}{\partial\,t} = \tilde{u}. \tag{57}$$

In the problem defined here, the velocity is a known function of time only, and so a sufficient, if elementary, finite difference form of the trajectory equation is just

$$\tilde{x}_n^{i+1} = \tilde{x}_n^i + \delta t\, u^i. \tag{58}$$

Notice that (58) is first order, and forward in time, and there are no space derivatives required. This is trivial to integrate in the present test problem, the only constraint on the time step is that it should be small enough to resolve the time dependence of the current. With that satisfied, the solution is almost exact (as in the method of characteristics) and so there is no reason to show it here. You can see this solution in the script noted in footnote 24 below, and experiment with different time steps.

In two or three dimensions there can be a significant practical shortcoming inherent to a purely Lagrangian model that does not arise in this one-dimensional test problem. Namely, the parcel trajectories are likely to become entangled, and the parcels distributed very unevenly across the model domain.[23] If the model required solving for the velocity and thus the pressure gradient and the laplacian needed for momentum diffusion, then this uneven and uncontrolled distribution of parcel positions (which are the positions where we know the solution) could become a significant issue. This is akin to the problem of evaluating a pressure gradient in the three-dimensional Lagrangian equations noted in Sec. 2.5 of Part 1. A viable solution is to map the Lagrangian data onto a grid, and then evaluate the pressure or gravitational mass attraction at the position of the parcels; this is the hybrid, Particle in Cell approach that will be discussed in Sec. 5.3.

5.1.3 Eulerian advection of a tracer field

Now consider the purely Eulerian version of (54) in which c is a function of the field coordinates x and time, t,

$$\frac{D\,c(x,t)}{Dt} \;=\; \frac{\partial c(x,t)}{\partial t} \;+\; u(x,t)\frac{\partial c}{\partial x} \;=\; 0. \tag{59}$$

In the Eulerian frame, the task is to calculate how the advection of the tracer field $c(x,t)$ changes c at the discrete, fixed grid point(s), x_n, of an Eulerian model grid. To evaluate the advection term requires the velocity, u, that is either specified or may be presumed known by the same method used to solve for the tracer.

A plausible, simple finite difference estimate of the gradient of c at x_n is the centered, first difference around x_n,

$$\frac{\partial c}{\partial x} \;\approx\; \frac{c_{n+1} \;-\; c_{n-1}}{x_{n+1} \;-\; x_{n-1}} \;=\; \frac{c_{n+1} \;-\; c_{n-1}}{2\delta x}, \tag{60}$$

and as a first guess for the time derivative,

$$\frac{\partial c}{\partial t} \;\approx\; \frac{c^{i+1} - c^{i}}{t^{i+1} \;-\; t^{i}} \;=\; \frac{(c^{i+1} - c^{i})}{\delta t}.$$

Forward in time, centered in space: Putting these two finite difference estimates together with (59) gives a very concise prescription, or 'scheme', for stepping the tracer ahead in time,

$$c_n^{i+1} \;=\; c_n^i \;-\; \delta t\; u_n^i\; \frac{(c_{n+1}^i - c_{n-1}^i)}{2\delta x}. \tag{61}$$

[23] See Welander, P., 1955, Studies on the General Development of Motion in a Two-Dimensional, Ideal Fluid, Tellus, May, 1955, 141-156. Online at https://onlinelibrary.wiley.com/doi/abs/10.1111/j.2153-3490.1955.tb01147.x

Thus, given c^i and the current, u^i_n, (61) provides an explicit estimate of the next time level, c^{i+1}. This is an explicit estimate in that the right hand side involves previous time levels only. An implicit estimate would include c^{i+1} on the right hand side. This scheme is called 'forward in time, centered in space', or FTCS.

The Eulerian numerical solutions to follow have been evaluated with a grid interval $\delta x = 0.01$, and with a nominal time step $\delta t = 1.0$, but varied from case-to-case. The end time is $t_M = 10000$ and hence there are $M = 10000$ time steps for the nominal δt.

The simple and intuitive FTCS integration scheme (61) seems hopeful, but it turns out to be wildly unstable; the tracer values quickly diverge and the calculation blows up, figuratively.[24] How and why the FTCS method is unstable can be anticipated from a von Neuman stability analysis, which is outside the present scope.[25] the finte difference advection terms tends to generate spurious high frequency (space scale $2\delta x$) variability, that can quickly swamp the physical process of advection that was intended by (59). In some cases these numerical errors can be minimized by choosing using a sufficiently small time step, δt. A very important parameter that characterizes the size of the time step is the nondimensional CFL number

$$CFL = \frac{U\ \delta t}{\delta x},$$

where U is the maximum amplitude of the advecting flow. For most explicit finite difference schemes, stability requires that the time step gives a CFL number less than 1, otherwise a time step will amount to an extrapolation that will be unstable. Accuracy may require that the CFL be considerably less than 1.

Second-order, Lax-Wendroff: Much better results come from the widely used Lax-Wendroff method, which is a second order, explicit scheme,

$$c^{i+1}_n = c^i_n - \delta t\ u^i\ \frac{c^i_{n+1} - c^i_{n-1}}{2\ \delta x} + \delta t^2\ u^{i2}\ \frac{c^i_{n+1} + c^i_{n-1} - 2c^i_n}{2\ \delta x^2}. \tag{62}$$

Compared with the unfortunate FTCS, there is a new term on the right hand side that can be interpreted as a diffusion process — a finite difference second space derivative multiplied by a coefficient that looks like an effective diffusivity, $\propto\ \delta t\ u^2$. Though not intentionally built into this scheme, this term acts to damp the growth of high frequency spatial variability coming from the first order advection term. The solution for tracer distribution computed via the Lax-Wendroff method with $\delta t = 0.5$ and CFL = 0.5 (Fig. 21, left, the red dashed line) shows some high spatial frequency noise on the edges of the tracer pulse, but otherwise looks good (but what can be considered good or bad will depend very much upon intended use of the solution). [26]

[24] The time-dependent solution for this and other schemes is displayed by the Matlab script LandEadvection.m available at https://www2.whoi.edu/staff/jprice/wp-content/uploads/sites/199/2023/04/LandEadvection.txt This script was written to be readily modified to your own experiments.

[25] A concise article on stability generally is https://www.flow3d.com/resources/cfd-101/numerical-issues/computational-stability/

[26] There is no denying that a comparison of numerical solutions as in Fig. (21) is deadly-dull. Considerbly better is to see how these and other solutions develop in time.[24] Some solutions start off with high frequency noise that slowly dissipates (or not, FTCS), and others show a secular trend in the peak amplitude, e.g., a persistent decay of the pulse amplitude that may mimic diffusion. This is very pronounced with a scheme called upwind differencing (shown in the script noted above, but not here) that seems well-conceived in as much as it recognizes that advection has an inherent direction, from upwind to downwind.

5.1.4 Semi-Lagrangian advection

There are hybrid numerical schemes that adhere to the spirit of (56) while keeping an Eulerian core and avoiding the problems associated with entangled trajectories. The solution is sought on a fixed spatial grid, while tracking parcels for only short times that do not generate complex, entangled trajectories. There are several plausible ways to do this in detail, but the central idea is that advection alone should be adiabatic.

Suppose that the model equations have been stepped forward to yield the tracer at a grid point x_n at a time t^i. From the Lagrangian perspective, and considering only advection, then the tracer at that grid point should be the tracer of the parcel that departed an upstream position at the previous time t^{i-1}, and then arrived at the grid node x_n at time t^i. (This is assuming that the present parcel position has a one-to-one mapping with previous times, and that there is no diffusion.) Given the known velocity field and its short-term history, the upstream departure point for this x_n, say x_{n-dp} may be calculated by a backwards-in-time integration of the trajectory equations,

$$x^i_{n-dp} \; = \; x^i_n \; - \; \delta t \; u^i$$

(57). It is very likely that the estimated departure point, x_{n-dp}, will not coincide with a node of the Eulerian grid, and so an estimate of the tracer value at the departure point will require an interpolation of the tracer field at the departure time. For example, suppose x_{n-dp} falls between the grid nodes x_m and x_{m+1}, and that the distance (no sign) to $x_m$is a. A linear interpolation to find the tracer at the departure point would then be

$$c^{i-1}_{n-dp} \; = \; c^{i-1}_m \; + \; \frac{a}{\delta x}(c^{i-1}_m \; - \; c^{i-1}_{m+1}),$$

and so

$$c^i_n \; = \; c^{i-1}_{n-dp}.$$

Most importantly, no CFL-like criteria arises here, and the time step need only resolve the time-dependence of the advecting current. Since the parcel identity is retained during only a single time step, a method of this kind is often referred to as semi-Lagrangian.

In the semi-Lagrangian solution shown in Fig. (21) right, the time step was taken to be $\delta t = 10$ and hence $CFL \; = \; 10$. Despite this comparatively large CFL, the end time solution isn't bad. There is some fairly pronounced smearing of the sharp edges of the tracer pulse caused by the repeated (10,000 times) linear interpolation. This smearing can be significantly reduced by use of a spline interpolation, (see Problem 2) below).

The practical difference between this semi-Lagrangian scheme compared with an explicit Eulerian scheme (Lax-Wendroff) is a significantly increased permissible time step. This has considerable value in applications where computational efficiency is a premium, say in weather forecasting or climate forecasting over long times.[27] On first sight it may seem as if the semi-Lagrangian method has given us a greatly reduced computational burden for nothing more than a modest complication of the model code.

[27] Staniforth, A. and J. Cote, 1991. Semi-Lagrangian integration methods for atmospheric numerical models - A review. Mon. Wea. Rev., 119, 2206 - 2224. A recent and very comprehensive discussion is by Fletcher, S., 2019, Semi-Lagrangian Advection Methods and Their Applications in Geoscience, Elsevier, ISBN: 9780128172223

But with a little reflection, it seems that this gain in efficiency comes from appeciating and exploiting the (fundamental) Lagrangian perspective that advection alone is an adiabatic process.

5.2 Layered models of the stratified ocean interior

An important example of a numerical model that is Lagrangian in one specific way while being Eulerian otherwise is the use of a layered representation of the vertical stratification of the ocean. The ocean interior has weak but important stratification that can be presumed to be stable (denser fluid always lying below less dense fluid, except in special circumstances that can be accounted explicitly when necessary). Important terms of the Eulerian density balance include the local rate of change of density and vertical advection,

$$\frac{\partial \rho}{\partial t} = -w\frac{\partial \rho}{\partial z} + ... \tag{63}$$

which is enough to discuss the issue. Numerical implementation of the vertical advection term does not present any exceptional difficulty but the result will generally include some spurious vertical diffusion that will eventually smear out the ocean's thermocline after the density profile has been advected up and down, perhaps thousands of times, by internal waves, which if modelled exactly would be adiabatic. The smearing effect may be likened to vertical mixing, and will occur to some degree even if no real (physical) vertical mixing was intended. Over the course of a long integration, such spurious (numerical) vertical mixing may lead to unrealistic density stratification.[28]

One antidote to this kind of spurious vertical mixing is to implement a Lagrangian representation of the vertical structure and advection process (63). In place of a vertical grid, the density profile is represented by discrete layers of thickness h within which the density and horizontal velocity are presumed to be uniform in the vertical.[29] Density changes from one layer to the next by a specified jump, $\delta\rho$, that is generally presumed to be constant in time (though that can be realxed, if required). The layers are thus defined by the upper and lower depths of material surfaces, coincident with the density jumps, $\delta\rho$, that move with the fluid according to the continuity relation,

$$\frac{\partial h}{\partial t} = -\nabla\cdot(h\mathbf{V}),$$

with $\mathbf{V}$ the uniform horizontal velocity within the layer. The vertical coordinates, the surfaces that define the h, are thus Lagrangian insofar as they are embedded within the fluid. The horizontal velocity is evaluated and stepped forward using an Eulerian system, and the vertical density profile and pressure readily calculated from the known layer thicknesses and density jumps. The density profile can change with time as the layer thicknesses change, but by holding the density jumps constant, the resulting vertical advection is assured of being adiabatic, i.e., without mixing. Layers defined by density tend to remain well behaved in that they are not likely to overturn and become entangled the way that horizontal

[28] Griffies, S. M., Pacanowski, R. C., and R. W. Hallberg. (2000) Spurious diapycnal mixing associated with advection in a z-coordinate model. Mon. Wea. Rev., 28, 538-564.

[29] Bleck, R. (2002) An oceanic general circulation model framed in hybrid isopycnic-Cartesian coordinates. Ocean Model., 4, 55-88.

surfaces would be in a vortex, for example. Such layered models are widely used in ocean modelling.

No scheme is without problems, and e.g., sustained divergence (as may occur in the ocean surface layer due wind stress) can cause the layer to become very thin and even vanish. Vanishing, or even very thin layers are troublesome for momentum balance (an example occurs in the wind-driven flow of the Indian Ocean noted in 'a Coriolis tutorial', Part 5). At the other extreme, e.g., in regions where there is significant heat loss to the atmosphere, the density may become homogeneous and so without vertical structure, or at least none that can be represented by such a layered model.

The same sort of spurious mixing is associated also with horizontal advection, but likely to be smaller than the genuine or intended horizontal mixing and so less onerous. However, if the goal of a model study is to investigate long range or long time tracer transport in the horizontal, then the same basic idea, that tracer transport may be modeled by the movement of discrete material surfaces, can be extended to three dimensions.[30] The fluid is represented by discrete, three-dimensional volumes of fluid that are bounded by material surfaces. These are, in effect, macroscale parcels, sometimes called 'sacks' since their bounding surfaces move with the fluid. The tracer concentration within a given sack is presumed constant in time unless an external source or some horizontal or vertical mixing process is explicitly implemented. The main task then becomes to solve for the three-dimensional motion of the bounding surfaces, where the necessary three-dimensional velocity is evaluated from what may be a highly deformed assemblage of three-dimensional sacks, e.g., imagine following macroscale parcels in the tea cup vortices of Fig. 2.

5.3 Particle in Cell models utilize hybrid dynamics

The considerable appeal of the Lagrangian system derives from the straightforward representation of the equation(s) of motion, written here as coupled first order PDEs,

$$\frac{\partial \tilde{\mathbf{X}}_\mathbf{i}}{\partial t} = \tilde{\mathbf{V}}_\mathbf{i}, \quad \text{and} \quad \frac{\partial \tilde{\mathbf{V}}_\mathbf{i}}{\partial t} = \frac{\tilde{\mathbf{F}}_\mathbf{i}}{M_i} \tag{64}$$

and from the tracking of identifiable particles (or parcels), the $\tilde{\mathbf{X}}_\mathbf{i}$. The awkwardness of the Lagrangian system arises when evaluating the $\tilde{\mathbf{F}}_\mathbf{i}$, often a pressure gradient (Sec. 2.4) and in a more general model, diffusion terms as well, in part because of the uncontrolled spatial distribution of Lagrangian particles. A variety of numerical modelling strategies have evolved from the goal of making use of (64) while mitigating the problems associated with evaluating the $\tilde{\mathbf{F}}$.

One major branch of this hybrid model family is called Particle in Cell (PIC) models. These combine the equations of motion (64) and particle tracking while representing the force $\tilde{\mathbf{F}}$ by way of a field formulation, i.e., on a fixed (Eulerian) grid. The particles of a PIC model thus move about within a regular grid or cells. PIC models are very widely used to simulate the dynamics of fluids that may be idealized as a dilute gas: on the small scale, the flow of laboratory-scale plasmas, in which case the particles are charged, elementary particles or ions, and on the large scale, the evolution of galaxies and even the entire universe, in which case the particles are stars or star clusters.

[30] Haertel, P. (2019) A Lagrangian ocean model for climate studies. Climate, 7, 41. DOI: 10.3390/cli7030041

To introduce the essential motive behind and the structure of a PIC model we will consider a maximally simplified model from numerical cosmology in which the fluid is a dilute ensemble of point-like masses, i.e., stars, that interact solely by gravitational mass attraction. A central goal of numerical cosmology is to understand how the markedly inhomogeneous mass distribution observed in the present universe could have evolved from what must have been very small mass/energy anomalies in the newly-born universe.[31] The starting point is the hypothesis that the motion of the stars (and mass generally) is governed by the initial condition, the big bang, and therafter modified mainly by gravitational interaction between each star pair. The Newtonian gravitational force on a star i due to another star, j, is just

$$\tilde{\mathbf{F}}_{i,j} \;=\; G\frac{M_i\,M_j}{|\tilde{\mathbf{X}}_j-\tilde{\mathbf{X}}_i|^3}(\tilde{\mathbf{X}}_j-\tilde{\mathbf{X}}_\mathbf{i}), \tag{65}$$

where G is the gravitational constant, $6.6743\times10^{-11}\ \ \mathrm{m}^3\ \ \mathrm{kg}^{-1}\ \ \mathrm{s}^{-2}$, M_i is the mass of star i, and $\tilde{\mathbf{X}}_i-\tilde{\mathbf{X}}_j$ is the vector displacment between pairs of stars. The gravitational force on star i is an attaction toward star j and vice versa. Our interest is in cases where there are many stars interacting gravitationally, and the net gravitational attraction on star i is then the linear sum of the gravitational attraction to all of the other stars in the ensemble. For an ensemble of N stars, the net force on star i is then

$$\sum_{i\neq j,j=1}^{N}\mathbf{F}_{i,j} \;=\; G\sum_{i\neq j,j=1}^{N}\frac{M_i\,M_j}{|\tilde{\mathbf{X}}_j-\tilde{\mathbf{X}}_i|^3}(\tilde{\mathbf{X}}_j-\tilde{\mathbf{X}}_i). \tag{66}$$

Particle-Particle models. If the ensemble is a small star cluster, then N is O(10^4) and the force on each member may be computed by the straighforward evaluation of the mutual interactions (66). Such systems are termed Particle - Particle (P-P) models, and are purely Lagrangian.[32]

The number of calculations required to evaluate the mutual gravitational force within a P-P ensemble increases as N^2, N stars each affected by N ensemble members. This N^2 computational burden may become intractable if the simulated particles are intended to represent physical stars one to one. For example, the number of stars in a typical galaxy like our Milky Way is O(10^{11}) (100 billion), which can not be calculated via (66). The same holds for the charged particles of even a very small plasma. A

[31] This subsection follows an excellent introduction to the PIC methods of numerical cosmology by Knebe, A., How to simulate the universe in a computer. https://astronomy.swin.edu.au/sao/guest/knebe/ . For a discussion of recent research see https://www.quantamagazine.org/coder-physicists-are-simulating-the-universe-to-unlock-its-secrets-20180612/ and for greater technical detail, Bertschinger, E. 1998, Simulations of structure formation in the universe. Annu. Rev. Astron. Astrophys., 36:599-654. An interesting discussion of the differences in a fluid continuum simulation vs. particle simulation is https://www.quantamagazine.org/the-tiny-physics-behind-immense-cosmic-eruptions-20230515/

[32] Notice that gravitational attraction goes as 1/separation^2, which becomes singular when point-like stars are nearing a collision. As the separation becomes very small the acceleration becomes very large and the consequent change in velocity is not likely to be resolved adequately by a time step that would be appropriate for the generally slow motions of the vast majority of well-separated stars. The numerical solution would then likely show the nearly colliding stars shooting away from one another at very high speed in a (spurious) phenomenon called two-particle collision. This may be mitigated by adding an ad hoc 'softening' factor to the distance between star pairs, i.e., in place of the actual distance, use instead distance + ε, with ε a relatively small positive constant. This is in most respects a detail compared with other important phenomenon that have been neglected here: 1) the all-important initial condition of mass distribution includes small anomalies inferred from the infrared background, 2) that the universe is expanding, 3) most of gravity is associated with dark matter (apparently) and not just visible stars as implied here, and 4) radiation pressure is a significant counter to gravitational mass attraction.

curative for this N^2 problem comes in stages which first give up some spatial resolution, and then the give up the simplicity of Eq. (66) in favor of a field perspective on the mass distibution.

Spatial averaging and Tree models. First, consider the gravitational attraction due to a comparatively small cluster of stars that is very far away from the point of interest (cluster radius $\ll$ distance to the cluster). The net gravitational attraction due to the cluster will then be approximated well by representing the cluster by a single massive particle that is located at the center of mass of the cluster. In that way, a great many individual stars may be replaced by one massive particle that gives very similar gravitational attraction at distant points. This kind of approximation is most appropriate when the region of particular interest is a small subset of the entire domain, in which case the outlying regions may be represented economically by this sptial averaging with no appreciable loss of fidelity. Models that make use of this approximation are sometimes termed 'Tree' models, since the scale of the spatial averaging increases with distance away from the region of interest. Like the P-P models, these are purely Lagrangian.

Particle in Cell models are semi-Eulerian. A second modelling approximation, and the one of particular interest here, is to retain the Lagrangian equations of motion and long-term particle tracking, while taking an Eulerian perspective when estimating the gravitational interactions. Thus, in place of evaluating the N^2 discrete particle-particle interactions of (66) directly, evaluate instead the gravitational potential *field* associated with a spatially smoothed mass distribution. The mass density at the fixed spatial coordinate $\mathbf{X}$, i.e., a grid point (and a field varible and so no tilde) is estimated as the local, spatially-averaged mass density

$$\rho(\mathbf{X}) \;=\; \sum_j M_j W(\mathbf{X}-\mathbf{h},\tilde{\mathbf{X}}_\mathbf{i}), \tag{67}$$

with W a window function (e.g., uniform or triangular) and h a length scale that sets the effective width of W, usually a small fraction of the domain width. The grid interval of the $\mathbf{X}$ array determines the spatial resolution of the gravitational potential field estimated from solution of the Poisson equation,

$$\nabla^2\Phi \;=\; 4\pi G\,\rho(\mathbf{X}), \tag{68}$$

where $\rho(\mathbf{X})$ is the spatially-averaged mass field evaulated from (67). The solution for Φ requires solving the elliptic equation (68) with suitable boundary conditions; if the domain is the entire universe, reentrant; if the domain encompasses only a single galaxy, then vanishing at infinity. Given the solution for $\Phi(x,y,z)$, the gravitational force on a given star is then readily evaluated as

$$\mathbf{F}_\mathbf{i} \;=\; -M_i\,\nabla\Phi(\tilde{\mathbf{X}}_\mathbf{i}). \tag{69}$$

The position of a given star $\tilde{\mathbf{X}}_i$ will generally not coincide with a gridpoint of the $\nabla\Phi$ field, and hence the evaluation of (69) will require an interpolation of the $\nabla\Phi$ field to each $\tilde{\mathbf{X}}_\mathbf{i}$. This interpolation plus the spatial smoothing of (68) and (67) obscures the fine spatial-scale variation of gravitational attraction associated with the actual spatial distribution of discrete particles in favor of the smoothed (spatially) field contributed by the neighboring particles and more distant clusters. This sets the smallest resolvable feature in the evolving mass density field to be not less than several grid intervals of the Φ field, but in return the computational load is greatly reduced compared with attempting the corresponding Particle-Particle model, from N^2 down to $Nlog(N) \ll N^2$, which is characteristic of sorting algorithms.

PIC models executed on cloud-based resources can simulate truly enormous ensembles, recently 10^9 particles, and over an elapsed time that is a significant fraction of the lifetime of the universe. The solutions of the most sophisticated PIC model simulations can be mass distributions that look, qualitatively and quantitatively, much like the observed distribution of galaxies and mass in our universe.[33]

5.4 Key ideas

1) Models that are meant to represent real fluid phenomenon generally have to be solved using numerical methods. Numerical models have the opportunity to treat different physical processes (and thus different terms) in a tracer balance by methods that are appropriate to the process, e.g., advection by a Lagrangian particle-tracking method, and evaluation of the mutual forces between particles by mapping to an Eulerian grid.

2) A semi-Lagrangian integration scheme treats advection as an adiabatic transport of discrete parcels that are followed for only a short time, and so do not develop complex, entangled trajectories. A semi-Lagrangian scheme may yield good accuracy and stability, and with a time step considerably greater than is permitted by the CFL criterion appropriate to a comparable, explicit, Eulerian advection scheme.

3) Some fluid systems are inherently anisotropic, e.g., because they have a marked aspect ratio, e.g., very large width to depth, as obtains for the basin scale oceans and global scale atmosphere. In that case, vertical advection may be viewed as the rise and fall of impermeable material surfaces across which the density diffrences remain constant (adiabatic).

4) An inherent difficulty with a pure Lagrangian scheme is that spatial gradients of the pressure or of gravitational mass attraction between particles are very likely to become ill-sampled as trajectories become entangled. A cure for this is to compute the quantities that require spatial gradients by mapping the mass distribution onto an (Eulerian) grid which allows straighforward estimation of pressure or gravitational mass attraction. Lagrangian parcels can then move through the grid, subject to the local pressure field or mass attraction of the surrounding parcels. This kind of Particle in Cell model architecture is widely used in studies of cosmology and plasma physics. PIC models could be dubbed semi-Eulerian, since their core is Lagrangian, but with a very important (Eulerian) mapping step required to evaluate the mutual forces between particles.

5.5 Problems

1) Use the Method of Characteristics to solve the tracer balance of Eqs. (54) and (55). You can do this informally, with no need to introduce parameterized trajectory equations.

[33] See the recent, remarkable application of PIC modelling to the evolution of the universe reported by https://academic.oup.com/mnras/article/512/4/5823/6524208

2) A Matlab project following on Sec. 5.1; experiments that you can carry out using the script LandEadvection linked in footnote 24.

(i) The pure Lagrangian scheme gives nearly exact solution for the nominal time step, $\delta t = 1.0$. What sensitivity (what change in accuracy) is there to larger or smaller δt?

(ii) It was noted in Sec. 5.1.3 that the FTCS scheme is unstable for the nominal CFL, 0.5. Can you discern a small enough time step that the FTCS is reasonably accurate?

(iii) You will notice that trouble for the FTCS starts on the sharp edges of the tracer square pulse. Suppose the IC is made to be Gaussian and smooth instead of a square pluse. Does that relieve the instability or merely delay it?

(iv) How does the accuracy of the semi-Lagrangian scheme depend upon the time step? Compare this to i) above.

6 Lagrangian analysis of an oceanic flow.

This final section will return to an analysis of the ocean currents observed by SOFAR floats and shown in the cover image of Part 1, and in Fig. (22).[34] These data show a coherent oscillation from northeast to southwest over a distance of several hundred kilometers, and on a time scale (period) of about two months. The change in direction of the motion appears to propagate across the float cluster from southeast to northwest, more or less perpendicular to the motion itself, suggestive of a plane wave. There are striking changes in the relative vorticity, e.g., anti-cyclonic when the floats are furthest poleward, that leads to the present analysis.

The phenomenon revealed by these data is interesting in itself, and, the analysis of these data makes good use of one of the fundamental properties of Lagrangian method, *viz.*, that a Lagrangian tracer balance comes in two pieces, the tracer value on moving parcels, and the trajectory of those parcels. The trajectory is observed directly, and so the issue is reduced to the tracer alone, one of the notional joys of Lagrangian observation discussed in Sec. 2.4.2 of Part 1. The tracers in this case are the vorticity and potential vorticity.

Many fluid phenomenon are illuminated by analysis of their vorticity balance, and perhaps nowhere is this more true than in the analysis of low frequency geophysical fluids (low frequency compared to gravity waves). Indeed, most understanding of low frequency geophysical flows comes by understanding

[34] To see these data in motion, visit https://www2.whoi.edu/staff/jprice/wp-content/uploads/sites/199/2022/06/LDE1300.mp4 This analysis and several of the figures in this section were abstracted from from Price, J. F., and H. T. Rossby, 1982, Observations of a barotropic planetary wave in the western North Atlantic. *J. Mar. Res.*, Vol 40 Supp., 543 - 558. https://www2.whoi.edu/staff/jprice/wp-content/uploads/sites/199/2023/11/PriceRossby-82.pdf

the distribution and the balance of q,

$$\text{the potential vorticity of a layer} \qquad \boxed{q \;=\; \frac{\chi \;+\; f}{h}} \tag{70}$$

The terms of the potential vorticity are:

the relative vorticity, $\chi \;=\; \nabla \times \mathbf{V}$,

the planetary vorticity, $\boxed{f \;=\; \Omega \cdot \mathbf{n} \;=\; 2\,\Omega\,\sin(latitude)}$

the layer thickness, h, taken to be the entire water column thickness, about which more below.

6.1 Estimating the potential vorticity

There were 18 floats in total, but this analysis will be carried out on only 12 of these that formed a coherent cluster on a horizontal scale of several hundred kilometers and for a period of several months. This excludes several floats that were farthest to the northwest, and seemed to meander randomly with low speeds, and three floats that were farthest to the southeast and that were caught up in a smaller, sub-mesoscale anti-cyclonic eddy that was advected by the larger, mesoscale motion emphasized here. This decision to analyze 12 of the 18 available floats amounts to a scale separation (Sec. 4.1) that is based on the observed phenomenon, mainly, but also on horizontal scale.[35]

Vorticity. The analysis begins with an estimation of the velocity gradient tensor (Sec. 3). The east and north gradients of the east and north velocity components were estimated by fitting a 2-dimensional plane to each velocity component, at daily intervals. The floats provide measurements of say the east or u-component of velocity at $n = 12$ float locations, (x_i, y_i), where i denotes a specific float. Let the cluster average of u, x, and y be $\bar{u} = \frac{1}{n}\Sigma u_i$ and similarly for $\bar{x}$ and $\bar{y}$. Now make a fit of a linear function of x and y to the measured $u(x_i, y_i)$ by minimizing the mean square difference,
$\Sigma_n \left(u(x_i, y_i) - (u_0 + a(x_i - \bar{x}) + b(y_i - \bar{y})\right)^2$ to find the best fit values of the coefficients that are interpreted as first partial derivatives, i.e., $a \;=\; \partial u/\partial x$ and $b \;=\; \partial u/\partial y$. The same is done for the v component of the velocity. The goodness of the fit may be diagnosed by the fraction of the velocity variance accounted for (labeled FIT in Fig 26).

Given an estimate of the velocity gradient tensor on each day, the vorticity and the divergence may then be readily formed by sums and differences of the horizontal shears, as in the Cauchy-Stokes Theorem of Sec. 3.5. These estimates are Lagrangian in that they were made on a material volume that was tagged by float cluster and followed for an extended period of time. (The Lagrangian variables in this section omit the tilde ($\tilde{}$), which should be understood.)

[35] The unresolved (unanalyzed) motion is more characteristic (more typical) of the open, mid-ocean than is the rather energetic, polarized motion emphasized here.

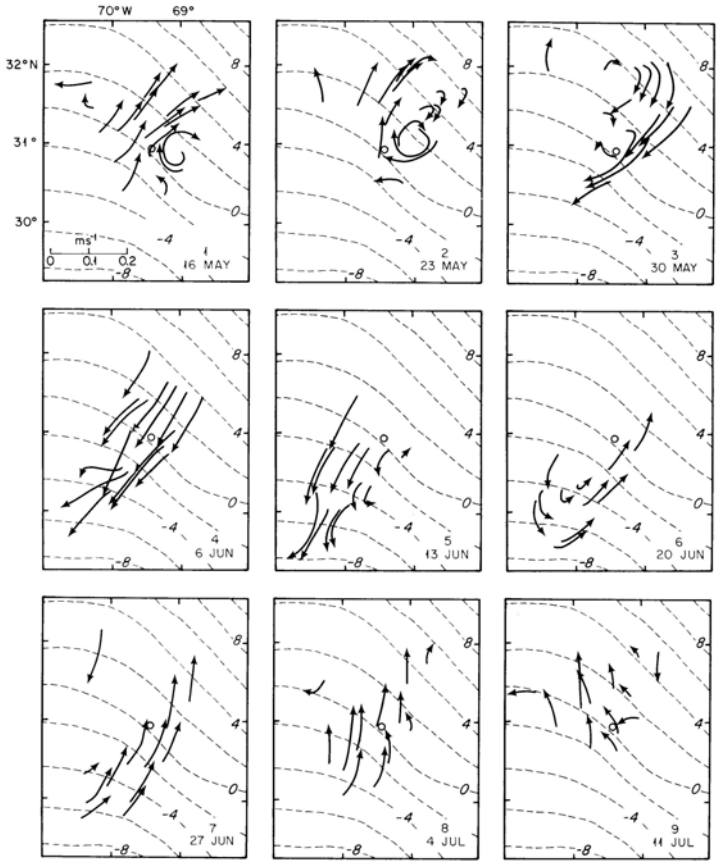

Figure 22: Maps of SOFAR float trajectories at weekly intervals. The region is the central Sargasso Sea, about 700 km west-southwest of Bermuda, and these floats were at a depth of 1300 m. A speed scale is in the upper left panel. The dashed contour lines in the background are lines of constant f/h in units of percent of f. The center of this figure just happened to be the location where the relative vorticity of the motion was approximately zero, and the zero of f/H is assigned there as well. There are two obvious kinds of motion evident here, the dominant motion is a northeast to southwest oscillation, the potential vorticity aspects of which are described in the main text. There was also a comparatively small, anticyclonic eddy centered on 31 N 69 W (on 16 May) that is not dealt with here. For an animation of these data, see the link in footnote 34.

Planetary vorticity. In the context of potential vorticity balance, the important variable f is often called the 'planetary vorticity' (while in the context of the momentum balance it is usually called the 'Coriolis parameter'). This name is apt because even when a fluid column is at rest with respect to Earth-bound observers, i.e., there is no horizontal wind or ocean current and so the relative vorticity $\chi = 0$, the column will nevertheless be rotating with respect to an inertial observer by virtue of riding along on the surface of a rotating, spherical Earth. The magnitude of this Earth's rotation-induced vorticity is given by the projection of Earth's (physical) rotation vector, Ω, onto the unit normal of the horizontal face of the column, $\mathbf{n}$, as $f = \Omega \cdot \mathbf{n} = 2\,\Omega\,\sin(latitude)$, where $\Omega = 2.729 \times 10^{-5}$ rad s^{-1} is Earth's (physical) rotation rate (one revolution per 23 hours, 56 minutes, 4 seconds). Earth's rotation vector (the spin axis) is closely aligned toward the north star, or pole star, Polaris, Fig. (23)[36], which is a very important direction that is defined with respect to the distant stars. The planetary vorticity thus has a direct dependence upon latitude, which is trivial to evaluate given the central latitude of the float cluster. A fluid column sitting directly over the north pole has a planetary vorticity that is two times the Earth's physical rotation rate, $f = 2\Omega$; if the column is at 30 N, the planetary vorticity is $f = \Omega$ and for a column on the equator, $f = 0$ and the planetary vorticity vanishes (Fig. 24). A column sitting over the south pole would

[36]The starscape image of Fig. (23) is thanks to Gavin Heffernan and the SkyGlow Project, https://vimeo.com/693011167, and modified slightly by the author.

Figure 23: Earth can claim no special place in the universe, but

Pole star, Polaris,
marks Earth's special direction
in isotropic space.

have a planetary vorticity $f = -2\Omega$.

If f is dubbed the planetary vorticity, then it is appropriate to call $\chi = \nabla \times \mathbf{V}$ the 'relative vorticity', since $\mathbf{V}$ is the fluid velocity relative to the rotating Earth and is the wind or current that we can observe directly. An inertial observer will see that the vorticity of a column is the sum of the planetary and relative vorticity, called the

$$\text{absolute vorticity,} \qquad \boxed{\xi \;=\; f \,+\, \chi}$$

An Earth-bound observer will observe directly only the relative vorticity.

Thickness. The thickness of a column is defined by material surfaces, i.e., density surfaces in the interior of the ocean (baroclinic motions) or by the sea floor and sea surface (barotropic motions). The thickness will be evaluated from the latter, provisionally, a choice that can be tested with the data.

6.2 Potential vorticity as a tracer

The balance of potential vorticity for a layer (70) may be derived from the adiabatic momentum and mass conservation equations for a rotating fluid layer in just a few steps: the curl of the momentum balance forms the vorticity, and eliminates the pressure gradient; the resulting horizontal divergence is eliminated in favor of the layer thickness (as in the Lagrangian treatment of vertical advection discussed in Sec. 5.2). For somewhat greater detail see e.g., a Coriolis tutorial, Part 2, Sec. 2. Aside from what are usually small effects of diabatic processes — bottom drag, wind stress curl, or diffusion — the q of a given fluid column in the open ocean is expected to be conserved approximately,

$$\frac{Dq}{Dt} \;=\; \frac{\partial q}{\partial t} \;=\; \frac{\partial (\frac{\chi + f}{h})}{\partial t} \;=\; 0, \tag{71}$$

at least for short times, a few months. Our interest is in the balance of the changes in relative vorticity and planetary or stretching vorticity (described below) and so it is useful to consider the linear, difference form of (71),

$$\delta\chi \;+\; \delta f \;-\; (\chi \,+\, f)\frac{\delta h}{h} \;=\; 0, \tag{72}$$

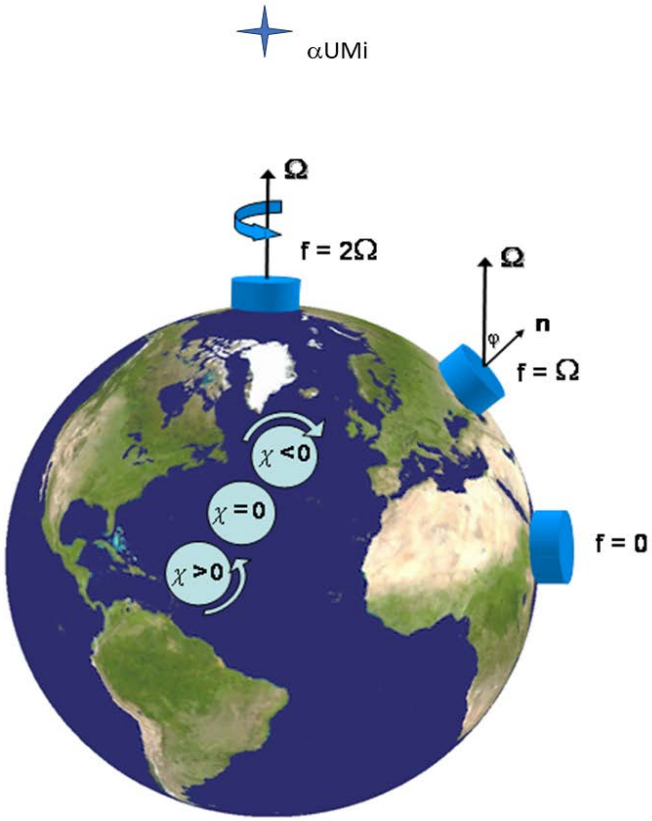

Figure 24: The spin axis Ω of our rotating Earth maintains a nearly steady direction toward a distant star, Polaris, α UMi, which is thus Earth's pole star (Fig. (23). The darker blue columns at right show that the horizontal rotation of a column due to Earth's rotation is $f = 2\Omega$ sin(latitude); the angle ϕ between the unit normal and Earth's rotation vector Ω is the co-latitude. The three lighter blue columns show the sense of relative vorticity acquired by a column that is displaced to the north or south while maintaining constant thickness. It is natural to show a column spinning about its center when it acquries relative vorticity, as here. However, the float cluster of Fig. (22) indicates that the relative vorticity was due mainly to horizontal shear rather than curvature, as implied by these spinning, vortical columns.

or when evaluated from observations,

$$R \quad + \quad P \quad + \quad T \qquad = \quad \varepsilon \tag{73}$$

where

$$\delta(\,) \;=\; \int_{t_0}^{t} \frac{d}{dt}(\,)\, dt$$

is the change in time following a given float cluster and presumably a material volume. Note that no one part of the expanded potential vorticity is conserved, but only the sum of the three terms.

The potential vorticity q is an intensive, scalar property of a (rotating) fluid, and has three properties that make it useful for the analysis of low frequency, geophysical flows: (1) The potential vorticity is transported with the fluid as a tracer, rather than with gravity wave phase speeds, as applies for momentum. Thus, q serves to tag the fluid, much like a passive tracer. (2) However, q is obviously closely related to the vorticity and the horizonal velocity, and in many cases knowledge of the distribution of q is sufficient to recover the horizontal velocity (though not when gravity waves are important). (3) The curl operation needed to form the vorticity equation from the momentum equation eliminates the pressure gradient (or any force derivable from a potential) which in low frequency flows is closely balanced with the Coriolis force. These two large nearly balancing terms make it difficult to analyze an observed momentum balance for the comparatively small terms/processes that allow the velocity to change. The

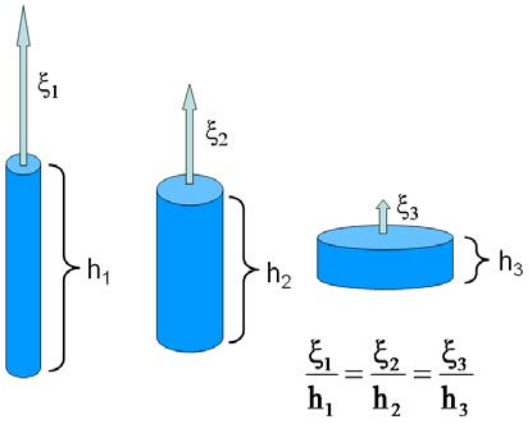

Figure 25: A schematic showing a spinning, deformable fluid cylinder that conserves its volume as thickness changes. Absent diabatic processes, it should also conserve angular momentum, ξ/h, as it undergoes changes in thickness, i.e., more positive ξ as the column lengthens (or stretched). If the vorticity is relative vorticity only, then this is directly analogous to the increased spin rate of an ice skater who pulls in her arms.

potential vorticity balance brings these processes (at least the adiabatic processes) to the fore.

6.2.1 Potential vorticity and changing latitude

Assuming for the moment that the thickness is constant, then the absolute vorticity of a column will be conserved, $d\xi/dt = 0$, or $\xi = \chi + f = constant$, including when a column changes latitude. For example, suppose that a fluid column is at rest at a mid-latitude so that it has a planetary vorticity f_0 and zero relative vorticity. Thus its absolute vorticity is just $\chi = f_0$. If this column is displaced toward the pole, as happened to the float cluster starting on ca. 16 May (Figure 22), then the planetary vorticity of the column will certainly increase. If the column maintains a constant absolute vorticity, $\xi = \chi + f = f_0$, it will acquire negative or anticyclonic relative vorticity,[37] $\delta\chi = f_0 - \delta f$, the amount given by the change in the planetary vorticity. After a couple of weeks of northeastward motion, the entire cluster reversed direction and moved back toward the southwest. As the float cluster moved equatorward, it acquired positive or cyclonic relative vorticity, which in this case served to erase the negative relative vorticity acquired during the poleward displacement. An observer who witnessed this motion from an inertial reference frame (outside the rotating Earth) would note that the absolute vorticity of the cluster remained constant (aside from thickness changes, discussed next). An Earth-bound observer, i.e., what we can see in Fig. (22), will see that the cluster lost and gained relative vorticity as it oscillated north to south.

6.2.2 Potential vorticity and changing layer thickness

Another and often very important aspect of vorticity balance is that changes in column thickness will have an effect upon the relative vorticity much like the effect of changing planetary vorticity. For a given

[37] Relative vorticity or rotation that is in the same direction as Earth's rotation is said to *cyclonic*, which comes from the Greek *kyklon* for circular motion. Cyclonic rotation is thus counterclockwise in the northern hemisphere and clockwise in the southern hemisphere. *Anticyclonic* is the reverse.

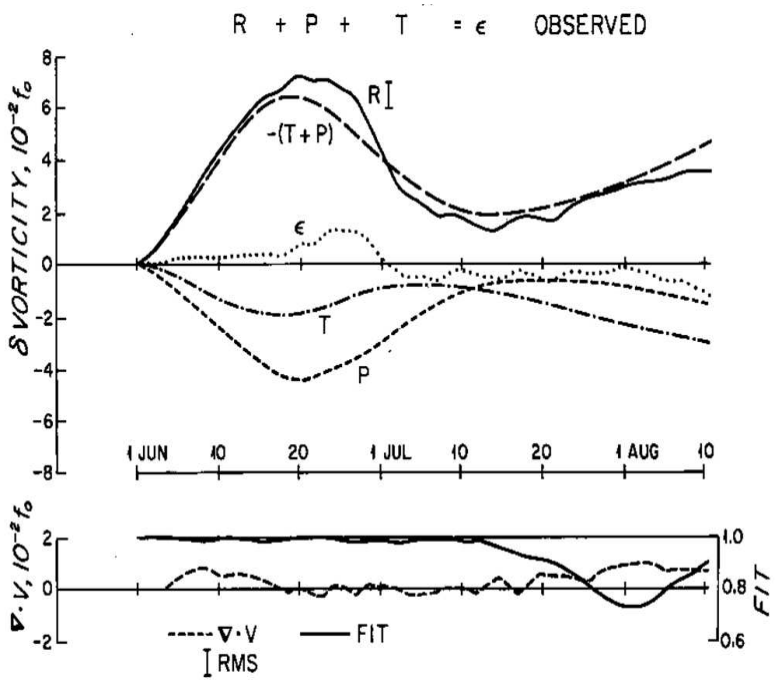

Figure 26: The balance of potential vorticity estimated from the float data of Fig. (22). The estimates begin on 1 June, as the float cluster moved southwestward through the center of the oscillation. The lower panel shows the divergence of the horizontal velocity along with FIT, the fraction of the velocity variance accounted for by the fitted plane; so long as FIT exceeds about 0.9, the velocity field is described well by a mean and the cluster-averaged horizontal shears in x and y. The sum $-(T+P)$, the topographic and planetary vorticity terms of Eq. (72), is consistent with the relative vorticity term, R, and thus with the conservation of potential vorticity by this motion.

column, the moment of inertia is $\propto 1/h$, and the absolute angular momentum is thus $\propto \xi/h$, which is just the potential vorticity noted above. If the thickness changes, then so too does the moment of inertia and the absolute vorticity, exactly as would be expected from angular momentum conservation. Thus when a fluid column is squashed, the result will be a slowed rotation rate (aside from changes in latitude and thus a change in planetary vorticity), and the reverse will happen if a column is stretched. In the example of the float cluster described here, the water depth shoaled gently toward the east and thus when the column moved northeast, it was apparently squashed by about 100 m out of a nominal thickness of 5000 m, or by roughly 2 percent, while at the same time f increased by about 3 percent. The changes in thickness and planetary vorticity were roughly comparable and in phase for this particular motion, and, are consistent with the change in relative vorticity that we can see directly in the float data (Fig. 26). Thus, the potential vorticity of this motion appears to be conserved approximately when the column thickness is identified with the water column thickness (i.e., the water depth). This implies that the motion was barotropic, with no appreciable effect of tilted density surfaces.[38]

It is noteworthy that a change in f/h of only about 5 percent is sufficient to account for the rather impressive change in the relative vorticity, about 5 percent of f_0, and by extension, of the current, which had an amplitude of roughly 0.15 m s^{-1}. Thus what would seem to be comparatively small changes in latitude or column thickness result in significant changes in the relative vorticity and the current itself. The reason, hinted at above, is that the planetary vorticity f is generally much larger then the relative vorticity of most ocean currents (and most winds) and hence the planetary vorticity represents a large 'potential' of the relative vorticity, which can be realized by changing either the latitude, and thus the

[38] Barotropic motions are quite common in the ocean, i.e., astronomical tides. However, low frequency, mesoscale eddy motions are likely to be significantly baroclinic. In that case, the column thickness would be defined better by density surfaces, and the phase of the motion quite different at different depths in the water column.

Coriolis parameter, f, or the column thickness.

6.3 Wave properties of the observed motion

You likely noticed that the floats oscillated in a specific direction, roughly northeast to southwest, and if you look closely you can see that the change in direction appears to propagate from southeast to northwest across the float array. In other words, the motion appears to be that of a polarized, or plane wave. The period and the wavelength may be readily estimated from an autocorrelation lagged in space and time, and were about 60 days and 340 km. The wave vector was toward 300 deg True, and the phase speed was about 0.06 m $\sec^{-1}$. These time and space scales are consistent with a short, barotropic Rossby wave, for which the planetary beta effect and the topographic effect discussed above are comparable, i.e., a planetary/topographic wave. Group speed inferred from the relevant dispersion relation was eastward and about 0.05 m $\sec^{-1}$, i.e., very slow.

6.4 Key ideas

1. Vorticity is proportional to the fluid rotation rate, and is an analogous to the angular momentum of a rotating solid. Important differences are that vorticity is defind locally (at every point) and does not refer to a moment arm.

2. Vorticity follows a conservation law that is more like that of a passive tracer than of momentum, since it is not propagated with gravity waves. The balance of vorticity can thus be the basis of an insightful analysis of many (not all) fluid flows.

3. The vorticity of large scale geophysical flows includes a very important contribution from the planetary rotation. The planetary voricity, f, is considerably larger than the relative vorticity of most large scale winds and ocean currents.

4. Planetary rotation is not apparent to Earth-bound observers, but becomes evident as relative vorticity when fluid columns change latitude; if toward larger f, then the induced relative vorticity is negative.

5. Similarly, planetary rotation is converted to relative vorticity when a fluid column is squashed or stretched in the direction parallel to Earth's rotation vector, analogous to a change in the moment of inertia.

6.5 Problems

1) An intertial-frame observer making observations of the velocity of a fluid column on Earth's surface will be able to observe (calculate) the absolute vorticity. We Earth-bound observers will be able to observe directly only the relative vorticity, χ, from observations of wind or ocean currents. Can you think of a way to infer the planetary vorticity, f from observations of the stars that are overhead? Refer to Fig.

(23), which is not looking directly 'up', and consider the special cases of a polar observation site and then an equatorial site.

2) How does the absolute vorticity change during the motion analyzed here?

3) This analysis was carried out in a Lagrangian coordinate or reference frame, in that the floats followed a material volume of fluid. The Eulerian statement of potential vorticity conservation (that we would be much more likely to use for a complete, predictive model) is just $\frac{D\tilde{q}}{Dt} = \frac{\partial \tilde{q}}{\partial t} + \mathbf{V} \cdot \nabla \tilde{q} = 0$. How would the northeast to southwest oscillation appear if it was observed at a fixed site, i.e., from an Eulerian reference frame? Consider three cases: (1) the idealized case that only variations of planetary vorticity are present, and assume that f can be expanded in a Taylor series, $f = f_0 + by$. (2) that only variations of water depth are important, and finally, (3) consider the actual, observed current field of Fig (22) and whether 'frozen field' advection of relative vorticity would have been observed (Sec. 6.1).

Index

Resource: Topics in Fluid Dynamics

James F. Price